Excitation of Toroidal Resonances in Metasurfaces and their Applications at Terahertz Frequencies

by

Angana Bhattacharya

A thesis submitted
in Partial Fulfillment of the Requirements
for the Degree of
DOCTOR OF PHILOSOPHY.

Department of Physics
Indian Institute of Technology Guwahati
Guwahati 781039, India.

July 2023


भारतीय प्रौद्योगिकी संस्थान गुवाहाटी
Indian Institute of Technology Guwahati

Excitation of Toroidal Resonances in Metasurfaces and their Applications at Terahertz Frequencies

by

Angana Bhattacharya
Roll No. 186121004

A thesis submitted
in Partial Fulfillment of the Requirements
for the Degree of
DOCTOR OF PHILOSOPHY.

Supervisor
Dr. Gagan Kumar

Department of Physics
Indian Institute of Technology Guwahati
Guwahati 781039, India.
July 2023


भारतीय प्रौद्योगिकी संस्थान गुवाहाटी
Indian Institute of Technology Guwahati

DECLARATION

This is to declare that I have carried out the work in this thesis entitled "*Excitation of Toroidal Resonances in Metasurfaces and their Applications at Terahertz Frequencies*" under the supervision of Dr. Gagan Kumar, Department of Physics, Indian Institute of Technology Guwahati. No part of this thesis has been submitted elsewhere for the award of any degree or qualification. The research works have been carried out in the period from January 2019 to March 2023.

In keeping with the general practice of reporting scientific observations, due acknowledgments have been made wherever the work described is based on the findings of other investigations.

Angana Bhattacharya

Angana Bhattacharya,
Roll no. 186121004,
Department of Physics, IIT Guwahati,
Guwahati-781039, Assam, India.
DATE: ....

CERTIFICATE

It is certified that the work contained in the thesis entitled "*Excitation of Toroidal Resonances in Metasurfaces and their Applications at Terahertz Frequencies*", submitted by Angana Bhattacharya, a student of the Department of Physics, Indian Institute of Technology Guwahati, for the award of the degree of Doctor of Philosophy, is a record of original research and was carried out under my supervision. The results in this thesis has not been submitted elsewhere for the award of any degree.

Dr. Gagan Kumar,
Department of Physics, IIT Guwahati,
Guwahati-781039, Assam, India.
DATE: ....

To Maa, Deta, and Dada

ACKNOWLEDGEMENTS

I would like to express my sincere gratitude towards my Ph.D. advisor, Dr. Gagan Kumar for his consistent support, guidance, patience and motivation during my Ph.D. years. His deep understanding of the field helped me understand my work better and his faith on me always inspired me to work hard and to do better.

I would like to express my sincere gratitude towards my doctoral committee members Prof. Dr. Uday Maiti, Prof. Bosanta Ranjan Boruah, and Prof. Sishir Nayak for their encouragement and insightful comments which helped me to improve my presentation skills and also my understanding of my work. I would also like to thank my collaborator Prof S.S.Prabhu, Ajinkya Punjal, and Prof Amir Ahmed for their help in certain projects. I also express my gratitude to Dr Ranjan Singh and Dr Manoj Gupta for their help and guidance in my research work.

My sincere gratitude goes to the current and former Heads of the Department of Physics, Prof. Perumal Alagarsamy and Prof. Subhradip Ghosh for providing me with all the facilities for my research and also to all the faculty members of the department and the non-teaching staff. I would also like to extend my gratitude towards the Centre for Nanotechnology, IIT Guwahati for providing me with clean-room facilities for nanofabrication of metasurfaces.

I would like to thank my PhD group-mates Bhairov, Bhagwat, Rohith, Chandan, and Anshul for all their support and the fruitful discussions, and for mainting an environment of friendliness in the lab. I express my gratitude to all my lab seniors, especially Dr Jagan for guiding me and encouraging me in my intial span of PhD. Gratitude towards Dr Dhriti, Dr Monika, Dr Rakesh, and Dr Maidul for their impact in my work. I would like to thank Dr Rajan, and Prerona for patiently teaching me the fabrication process in the cleanroom.

I would like to thank my PhD batchmates, especially Debu, Mandira, Sudeshna, Sashi, and Suchit for being a part of the ups and downs of my PhD journey. My gratitude

to Puja, Sarmistha, and Kakoli for making me laugh all the time. Special thanks to Sukhjeet for always being there and helping me not just survive, but thrive. Thanks to Ravi, and all the people I played badminton with - the evening sessions acted as sponges to any slightest low I ever felt. My gratitude towards my friends from college Madhur, Akanksha, and Mahima for being just a phone call away, and Harsh and Agarwal for all the academic advice. Also, a special mention to Himanku Da for his help in all the right matters.

Last but not the least, my heartfelt gratitude to my parents and my brother for their extreme belief in me. It astounds me at the amount of faith my brother has in me. Thanks Pompom, I would be absolutely nothing without you. To maa and deta, thank you for giving the world to me and standing by me, sometimes even beyond your means. And thanks for being my biggest cheerleaders. My sincere gratitude to Emi, Jethi, Jetha, Moha, Pakhi, Tora for being an oasis in dark times. All my heart and thanks to the rest of my cousins and my family for all the support and love.

ABSTRACT

The terahertz (THz) range of frequencies has become an important field of research in recent times, with the advent of electromagnetic metasurface technologies. This thesis focuses on the study of the excotic toroidal excitations in metasurfaces and their applications in terahertz frequencies. The toroidal dipole excitations, dominated over by electric and magnetic dipole excitations in natural materials, can be examined and utilzed in carefully designed metasurfaces. There has been a rapid growth in the study of toroidal metasurfaces because of the increasing demand for high-speed, low-loss photonic devices. This thesis examines, both numerically and experimentally, the excitation of toroidal resonances in metasurfaces, their modulation and electromagnetically induced transparency effects in a toroidal metasurfaces. Further, the thesis discusses the applications of toroidal metasurfaces for broadband terahertz polarization conversion and in exciting polarization independent resonances via a lattice-coupled toroidal mode.

In this thesis, the toroidal excitation has been discussed in carefully designed metamaterials with special toroidal symmetries in the terahertz range. The bilayer near-field coupling between two toroidal resonators was analysed and the passive modulation of the dual toroidal resonance has been discussed. In an effort to explore the possibility of active modulation in terahertz metasurfaces, the active tuning of toroidal resonances in a graphene based metasurface has been studied in this thesis. Further, several concepts and applications for the study of toroidal resonances in metasurfaces were examined. A study has been made on the excitation of single and dual-band electromagnetically induced transparency (EIT) via near-field coupled toroidal metasurfaces in this thesis.The bright-bright mode coupling between the resonators explains the dual-band windows in the proposed metasurface. Such toroidal dual-band EIT could be impactful in the study of slow light systems.

The thesis also examines the possibility of terahertz polarization conversion using toroidal excitations in a metasurface. Recently, there has been increased interest in

the study of terahertz broadband polarization convertors. In this context, a terahertz broadband polarization converter has been developed by carefully designing a toroidal meta-atom. Through the rotation of the meta-atom, nearly 40% cross-polarization conversion was achieved for a 45^0 rotation angle of the meta-atom. The thesis has also examined the possibility of further enchancement of the quality factor of a toroidal resonance by exploring the effect of coupling the toroidal excitation to the first-order lattice mode of the metasurface. The coupling between a toroidal mode and a first-order lattice mode resulted in the enhancement of quality factor in a simple metasurface geomtery. The designed metasurface ensures polarization independence, such that the sharp toroidal mode is excited for both the orthogonal polarizations of incident THz radiation.

The toroidal excitation and its applications, as discussed in this thesis, can have immense significance in high speed terahertz components for low-loss communication devices. Such toroidal terahertz metadevices have the potential to contribute towards the design and fabrication of modulators, slow-light system, polarization converters, and low loss terahertz photonic devices.

LIST OF PUBLICATIONS AND CONFERENCES ATTENDED

Journal Publications

1. **Bhattacharya, Angana**, K. M. Devi, T. Nguyen, and G. Kumar, "Actively tunable toroidal excitations in graphene based terahertz metamaterials," Opt. Commun., vol. 459, p. 124919, 2020.

2. **Bhattacharya, Angana**, R. Sarkar, and G. Kumar, Excitation of near field coupled dual toroidal resonances in a bilayer terahertz metamaterial configuration. Journal of Physics D: Applied Physics, 2021. 54(28): p. 285102.

3. **Bhattacharya, Angana**, Sarkar, R., Sharma, N.K., A. Ahmad, G. Kumar Multi-band transparency effect induced by toroidal excitation in a strongly coupled planar terahertz metamaterial. Sci Rep 11, 19186 (2021).

4. **Bhattacharya, Angana**, Rakesh Sarkar, and Gagan Kumar. "Toroidal electromagnetically induced transparency based meta-surfaces and its applications." Iscience 25.1 (2022).

5. Broadband terahertz polarization conversion using a planar toroidal metamaterial, Rakesh Sarkar, **Angana Bhattacharya**, Ajinkya Punjal, S.S. Prabhu, Gagan Kumar, Accepted in Journal of Applied Physics.

6. Dhriti, K. M., Maidul Islam, **Angana Bhattacharya**, Amir Ahmad, and Gagan Kumar. "Plasmon-induced transparency in an air–dielectric grooved parallel-plate terahertz waveguide." JOSA B 38, no. 4 (2021): 1290-1296.

7. **Bhattacharya, Angana**, B.C Chouhan, B. Bhowmik. and G. Kumar, "Polarization Independent Lattice-Coupled Toroidal Excitations in a Terahertz Metasurface", **Communicated**.

Conference Publications

1. A. Bhattacharya and G. Kumar, "Slow Light Effect in a High Quality Factor Toroidal Mode in a Terahertz Metasurface," in Frontiers in Optics + Laser Science 2022 (FIO, LS), Technical Digest Series (Optica Publishing Group, 2022), paper JTu5A.92.

2. A. Bhattacharya, R. Sarkar, A. Punjal, S. S. Prabhu, and G. Kumar, "Planar Terahertz Toroidal Meta-Device for Efficient Polarization Conversion," in Conference on Lasers and Electro-Optics, Technical Digest Series (Optica Publishing Group, 2022), paper FF3D.4.

3. A. Bhattacharya, K.M. Devi, and G. Kumar. Toroidal Resonances in Graphene Metamaterials. in 2019 Workshop on Recent Advances in Photonics (WRAP). 2019. IEEE.

4. A. Bhattacharya, R. Sarkar, A. Bharadwaj, and G. Kumar. "Sensing in a toroidal coupled dual-band EIT terahertz metadevice." 2022 Workshop on Recent Advances in Photonics (WRAP). IEEE, 2022.

5. B. S. Chouhan, K. Dhriti Maurya, B. Kumar Bhowmik, A. Bhattacharya and G. Kumar, "Graphene-Dielectric based Tunable Terahertz Polarisation Insensitive Modulator," 2022 IEEE Photonics Conference (IPC), Vancouver, BC, Canada, 2022, pp. 1-2, doi: 10.1109/IPC53466.2022.9975603.

6. Bhargav, R.A., KM Dhriti, A Bhattacharya, G Kumar. Refractive Index sensing using plasmonic mode in a periodically corrugated waveguide at terahertz frequencies. in 2019 Workshop on Recent Advances in Photonics (WRAP). 2019. IEEE.

Conferences/Schools attended

1. Winter College on Optics: Terahertz Optics and Photonics 2023, Oral presentation on "Logic Gate Operations in Toroidal Terahertz Metasurfaces", February 2023 ICTP, Trieste, Italy (**1st Place in Oral Presentation**)

2. Conference on Lasers and Electro-Optics (CLEO) 2022, Oral presentation on "Planar Terahertz Toroidal Meta-Device for Efficient Polarization Conversion", May 2022, SanJose, California, USA, (**Oral Presentation**).
3. Frontiers in Optics + Laser Science 2022 (FIO LS), Poster presentation on " Slow Light Effect in a High Quality Factor Toroidal Mode in a Terahertz Metasurface", October 2022, Rochester, New York, USA (**Poster Presentation**).
4. Optica Student Leadership Experience 2022, Rochester, New York, 2022 (**participation**).
5. Frontiers in Terahertz Technologies, Invited talk on "EIT on Toroidal Terahertz Metasurfaces", December 2021, NPL, New Delhi (**Oral Presentation**).
6. Research Conclave, Three-Minute Thesis Presentation, 2023, IIT Guwahati, Assam, India (**1st Place**).
7. Research Conclave, Oral presentation on "Toroidal Excitations in Terahertz Metasurfaces", January 2022, IIT Guwahati, Assam, India (**1st Place in Oral Presentation**).
8. Indian Nano Users Program (INUP)-2022, Poster presentation on "Multiband EIT in Toroidal Metasurfaces", IIT Guwahati, Assam, India (**1st Place in Poster Presentation**).
9. Workshop on Recent Advances in Photonics 2019, Poster presentation on "Graphene based Toroidal Terahertz Metamaterial", December 2019, IIT Guwahati, Assam, India (**Poster Presentation**).
10. Workshop on Recent Advances in Photonics 2022, March 2022, IIT Bombay (**Online Poster Presentation**).
11. IEEE Photonics Conference 2022, November 2022, Vancouver, Canada (**Oral Presentation**).
12. National Science Day celebration 2023, Invited talk on "Toroidal Excitations in Terahertz Metasurfaces and Applications Dept. of Physics, IIT Guwahati (**Oral Presentation**).

LIST OF FIGURES

radius 'r_1'. When polyimide layer covers the first layer of resonators it is termed as 'single SRR'and when the second layer of resonators are added, the overall design is called as 'double SRR'. (c) Side view of the bilayer MM design. (d) The transmission spectra for 'single SRR'configuration showing single toroidal resonance dip at 1.34 THz and the transmission spectra for the 'double SRR'configuration showing dual toroidal resonances at 1.21 THz and 1.58 THz respectively.The green arrow indicates the direction of polarization of the incident THz beam.

- **Figure 3.2:** (a) Surface current profile of the single SRR layered with polyimide at 1.34 THz. The surface current on the right arm is along anticlockwise direction while on the left arm is along clockwise direction, leading to end to end formation of magnetic moment and a clear formation of toroidal dipole moment is observed. (b) End to end formation of magnetic moment indicating toroidal excitation.

- **Figure 3.3:** (a), (b) Surface current profile for bottom SRR and top SRR respectively for bilayer MM design at 1.21 THz. (d), (e) surface current profile for bottom and top SRR respectively for bilayer MM at 1.58 THz. The clockwise and anticlockwise current flow clearly depict toroidal dipolar excitation in the MM design. (c), (f) Magnetic field profile showing end to end magnetic moment formation leading to toroidal dipole excitation at frequencies 1.21 THz and 1.58 THz respectively.

- **Figure 3.4:** Multipolar analysis of the bilayer metamaterial depicting power radiated by the multipolar moments over the simulated frequency range. It is seen that at 1.58 THz power radiated by toroidal dipolar resonance dominates over that of electric and magnetic dipolar resonances. At 1.21 THz where toroidal dipolar resonances are aligned along opposite direction, power radiated by electric dipolar resonance dominates.

- **Figure 3.5:** (a) Transmission spectra for 'single SRR' when top SRR is rotated by 45 degrees and 90 degrees with respect to the bottom SRR. The excitation diminishes at a fixed resonance frequency as rotation angle increases to 90 degrees. (b) The dual toroidal resonance seen for bilayer design ('double SRR') at the initial position of 0 degree. The high frequency resonance diminishes and vanishes at 90-degree rotation, leaving a single toroidal resonance corresponding to the bottom layer. (c) The contour plot shows the shift of resonances as the top SRR is rotated from 0 to

90 degrees and the final vanishing of higher frequency resonance for 90 degrees' rotation of top resonator.

- **Figure 3.6:** (a) Surface current for bottom resonator, showing toroidal behaviour when top SRR is rotated by 90 degrees at 1.145 THz. (b) Surface current profile for top SRR when it is rotated by 90 degree with respect to bottom SRR. Current profile shows no clockwise anticlockwise nature and toroidal dipolar moment is not observed. (c)Top view of magnetic field profile showing toroidal dipole excitation in bottom SRR and no toroidal excitation in top SRR.

- **Figure 4.1:** (a) Schematic of the proposed terahertz metamaterial structure resulting in toroidal excitation. Silicon substrate is shown in blue color, whereas graphene split rings are shown with gray color. The inset shows a larger view of the metamaterial unit. The unit cell consists of two split ring resonators, each having two gaps, which have been joined together to form a single resonator. p_x and p_y represent periodicities of the unit cell in the x and y directions, respectively. l and b stands for length and breadth the unit cell. Width and split gap of the resonator is represented by w and g. The configuration allows us to excite toroidal resonance in the y-direction, shown by T. (b) Transmittance versus frequency plot of the MM structure resulting in toroidal excitation for E_F=1 eV of graphene.

- **Figure 4.2:** (a) Surface current profile in the graphene metamolecule structure having $E_F = 1$ eV. The current flows in clockwise direction in the right half of the resonator, whereas it flows in the anti-clockwise direction in the left half as indicated by black arrows. The current directions result in the formation of end to end magnetic dipoles, thus leading to a toroidal response (b) Magnetic field profile at $f = 1$ THz in the xz plane of the metamaterial unit cell structure indicating toroidal behaviour due to oppositely circulating currents.

- **Figure 4.3:** (a) Transmittance versus frequency for increasing values of Fermi energy from 0.2 eV (in black) to 1 eV (in green). There is an evident blue shift in the toroidal resonance on increasing Fermi energy. (b) Colour and contour plot for Fermi energy versus frequency indicating a shift in the toroidal resonance. (c) Variation of toroidal frequency versus Fermi energy of graphene layer for $\tau = 2\ ps$. The frequency increases with Ferimi energy as $\omega \propto {E_F}^{\frac{1}{2}}$.


भारतीय प्रौद्योगिकी संस्थान गुवाहाटी
Indian Institute of Technology Guwahati

LIST OF ABBREVIATIONS

- **Terahertz:** THz
- **Metamaterial:** MM.
- **Split Ring Resonator:** SRR.
- **C-shaped split ring resonator:** CSRR
- **Toroidal split ring resonator:** TSRR.
- **Computer Simulation Technology Microwave Studio Simulation Software:** CST Software.
- **Scanning electron microscopy:** SEM.
- **Terahertz Time-Domain Spectroscopy:** THz-TDS.
- **Electron Beam Lithography:** EBL
- **Electromagnetically Induced Transparency:** EIT.
- **First Order Lattice Mode:** FOLM.
- **Quality Factor:** Q.

TABLE OF CONTENTS

CHAPTER 1

INTRODUCTION

The toroidal excitation is a new type of electromagnetic excitation that is excited when magnetic dipole moments are arranged in a head-to-tail configuration. The toroidal dipole moment has sharp resonant features but are masked in natural materials by the domineering electric and magnetic moments. Artificially designed material surfaces, termed as meta-surfaces, can result in the domineering effect of toroidal resonances over other tyoe of electromagnetic resonances and hence, utilize the excitation to its full potential. The terahertz (THz) range of frequencies, lying between the microwave and infra-red frequencies provides a new arena of research. The study of toroidal excitations in metamaterials has wide potential to demonstrate responses that can find wide applications in futuristic terahertz photonic devices.

1.1 Terahertz Radiation

Terahertz (THz) is the region between microwave and infrared radiation in the electromagnetic spectrum (EM). It is generally considered to be between 300 GHz to 10 THz. Electromagnetic oscillations in picoseconds range results in the THz spectra. 1 THz has a wavelength of 300 μm, photon energy of 4.1 meV and temperature of 47.6 K. Numerous terahertz sources surround us including blackbody radiation from room temperature bodies. There exists a gap in the availability of technology in utilising the THz band of frequencies, specifically due to the problems faced in its generation and

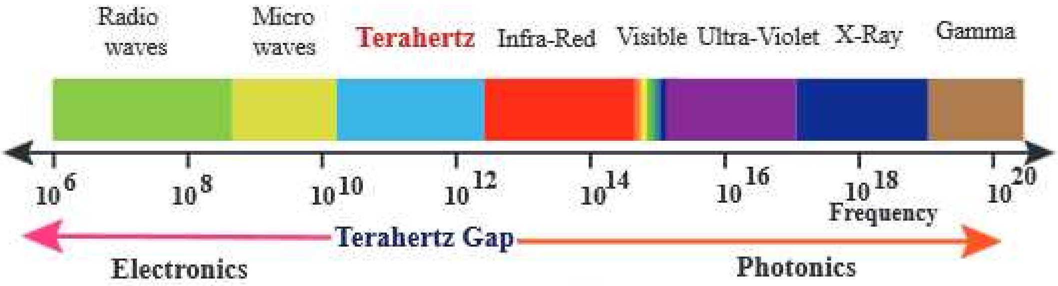

Figure 1.1: The terahertz 'gap' region in the electromagnetic spectrum.

detection. There are two ways to generate radiation: the classical way and the photonic approach. For radio waves and microwaves in the shorter frequency band, the classical approach is followed where oscillating charges radiate at the frequency of oscillation. The quantum approach, which is seen for higher frequencies in the optical band, depends on the band gap wherein electrons are forced to jump from a lower energy level to a higher energy level, thereby releasing photons of a given frequency [1]. However, it is difficult to oscillate electrons at such high frequencies that would enable the classical approach for radiation of THz . At the same time, the energy of THz is very small (4 meV) and there aren't naturally occurring solids with such a small bandgap. Thus the quantum approach of generation too meets with difficulties. For the reason that it is difficult to influence the THz radiation with conventional components, there is a gap in the generation, detection and harnessing of the terahertz band of frequencies. Figure 1.1 shows the THz band in the electromagnetic spectrum. Terahertz has a number of advantages because of its unique properties [2]. Due to its low energies, it does not cause damage to biological tissues. It passes through most dielectrics and provides profile and composition information. The spectrum of several explosives, including RDX and TNT, can be detected using THz as they have signatures in this frequency range. NASA has been using THz spectroscopy to detect defects in their space crafts at around 0.5 THz. The high water absorption of THz radiation also has potential in astronomy for the detection of water in space. In recent times, the gap in the generation, detection, and applications of terahertz radiation is being bridged through innovative technologies. Photoconductive antennas (PCA) are used for terahertz emission as well as detection. During the 1980s Fattinger and Grischkowsky first demonstrated the use of PCA for terahertz generation [3], which was further studied and designs demonstrated the capacity t generate THz of up to 40 μW and bandwidths of 10 THz. The PCA is a DC biased metal dipole antenna made on a photoconductive substrate. It consists of a gap between the metal contacts. The metal contacts are biased and the gap is the region for THz generation. For terahertz generation an optical pulse from a femtosecond laser is made incident on the antenna gap. This pulse generates photoelectrons which are accelerated due to the the DC bias field, producing a transient photocurrent, and thus produces a THz frequency pulse. A short carrier life time is preferred for the photoconductive material as longer carrier lifetimes lead to broadening of output pulse and a reduction in THz bandwidth. As a result, photoconductors with picosecond carrier lifetimes are chosen as substrate material. The performance of THz PCA-based systems depend on Signal to noise ratio (SNR), strength of the THz signal, bandwidth of the THz signal, and optical-to-THz conversion efficiency. SNR is often defined as the ratio of the peak signal in the frequency-domain spectra with the amplitude of the system noise (i.e., the measured RMS signal amplitude at the detector when the THz beam is blocked) [4]. The substrate material in addition to a low carrier lifetime, must maintain relatively high carrier mobility, appropriate bandgap, high breakdown voltage and suppression of zero bias photocurrent. Low temperature GaAs is one of the most preferred materials. GaAs has a room temperature bandgap of 1.424 eV (871nm) which makes it compatible with femto second pulsed laser sources used to excite PCAs. The LT-GaAs was grown are grown at temperatures between 200^0C and 250^0C. This has two benefits: high level of crystallinity, which in turn leads to higher carrier mobility and increased point defects which lead to reduced carrier lifetimes. For generation of high bandwidth THz, ultrashort pulse lasers need to be used to excite the antenna gap and hence, femtosecond lasers are used. Generation and detection of ultra-broadband THz radiation exceeding 10 THz are possible by using electro-optic crystals as the emitter and detector. Lying in the intersection of optics and electromagnetics, terahertz waves for long couldnot fit into the approximations of either frequency range. In such a scenario, the role of artificial materials, or metamaterials became significant. By constructing the dimensions of the meta-atoms lesser than that of wavelength of THz radiation, it has been possible to make artificial structures or materials which show excitations at the THz frequency range. Thus MMs have found application in sensing, switching, imaging, filters, scanning, and much more by harnessing terahertz frequencies. The next section provides an in-detailed decription of metamaterials and two-dimensional metamaterials, termed as metasurfaces.

1.2 Metamaterials

Metamaterials can be defined as an array of subwavelength artificial structures that are designed to achieve electromagnetic excitations dependent on their geometry. Each constituent block of a metamaterial is called a meta-atom. It attains its properties from the unit structure rather than the constituent materials. When a collection of objects have sizes much smaller than the wavelength of incident light, the atomic details lose importance and the inhomogeneous atomic scale can be averaged over to be replaced by a homogeneous electric permittivity (ε) and magnetic permeability (μ). From the electromagnetic point of view, the wavelength decides whether a collection of atoms or other objects can be considered a material. From a general definition of material such an inhomogeneous collection of structures with unit size much larger than atomic or molecular level of conventional substances may not be defined as a material. However, an EM wave passing through this subwavelength structure cannot tell the difference and hence, an EM artificial material or a metamaterial is created [5]. It is usually seen that at optical frequencies there is no magnetic response. At frequencies higher than microwaves it is challenging to achieve any magnetic response. In 1999 Pendry et al [6] first demonstrated microstructures build from nonmagnetic conducting sheets that showed an effective magnetic permeability which could be tuned to values not found in naturally occurring materials. They studied arrangements of array of cylinders, Swiss roll like arrangements and the popular split ring resonators to demonstrate the magnetic effect. They showed that artificial magnetism is possible in materials when the magnetic field component of the incident light interacts effectively with the meta atoms.

The split ring resonator (SRR) is one of the very popular structures used in metamaterial study. The split ring resonator consists of a circular or rectangular strip with gaps in between. The strip has an inductance 'L' while the gap has a capacitance 'C' leading to an LC circuit with a resonant frequency. Since the L and C of the resonator depend on its dimensions, therefore the resonant frequency of the SRR can be tweaked by changing the dimensions of the structure. The first split ring resonator proposed by Pendry et al in the microwave range is shown in figure 1.2 (a). Soon after, Smith et al proposed their split ring structure in the GHz range. In a split ring resonator, either the oscillating magnetic field couples weakly with the structure resulting in the flow of induced current in the boundaries. This leads to the development of a magnetic flux in the opposite direction and hence, a magnetic moment forms. The other method for

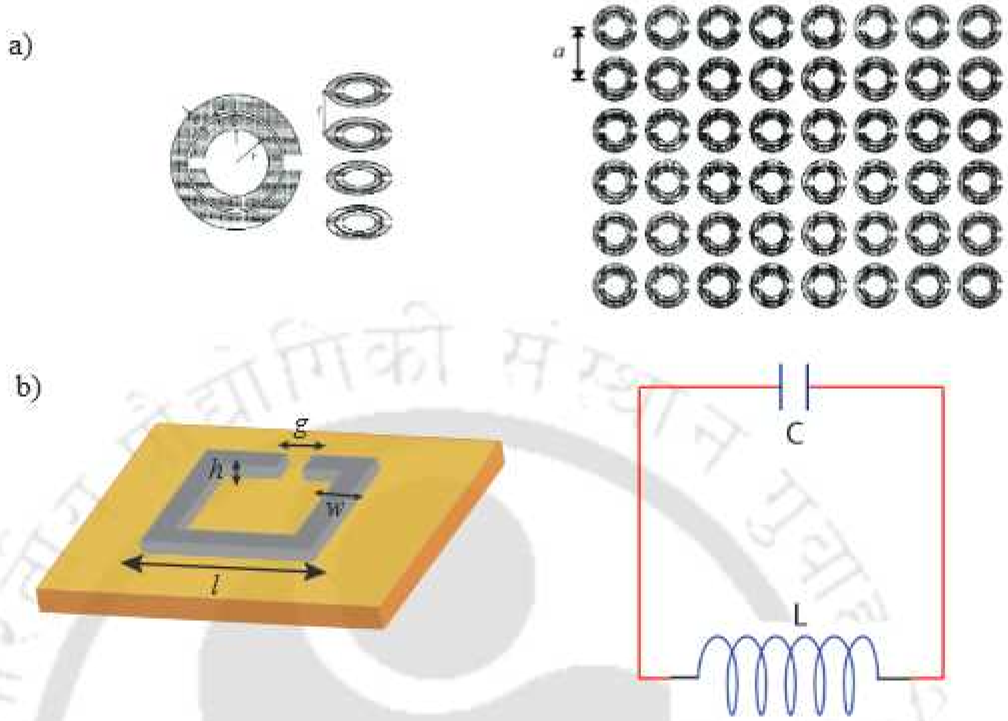

Figure 1.2: (a) Split Ring resonators initially proposed by Pendry et al of dimensions in the range of millimetres. The array of such split ring resonatos with lattice spacing 'a' © IEEE [November 1999][6]. (b) The C shaped SRR and (c) corresponding LC circuit model.

developing magnetic resonance is by exciting an electric field parallel to the gap bearing arm. A current starts flowing in the SRR and a magnetic moment is obtained. When polarization of the field is changed by 90 degress, this magnetic moment disappears. The array of such circular split ring resonators in the MM is depicted on the right side. Figure 1.2 (b) depicts a planar split ring resonator. Its inductance is $L = \frac{\mu_0 l^2}{h}$, its capacitance is $C = \frac{\epsilon_0 w h}{g}$, and its resonant frequency is $\omega = \frac{1}{\sqrt{LC}}$ [7]. The equivalent LC circuit model is depicted on the right hand side. Thus a change of L and C can be brought about by tweaking the length, thickness, or other dimensions and a corresponding change in the resonant frequency can be obtained. The constituents of MMs are different for varying frequency ranges. In the microwave range copper is preferred as it is commonly used in PCB fabrications. In the infrared band, gold and silver are preferred. Gold has better stability against environmental degradation and is also better performing in nano-fabrication techniques. However, for MM in visible frequencies silver is preferred due to lower loss as compared to gold. Besides artificial magnetism, MMs have shown various exotic phenomena including negative refractive index, electromagnetically in-

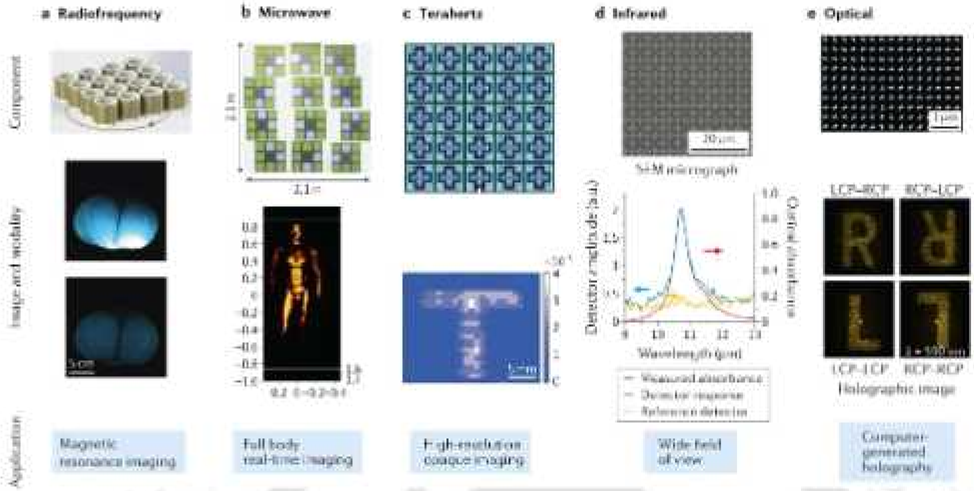

Figure 1.3: Metasurfaces for imaging applications at (a) radiofrequency, (b) Microwave region, (c) Terahertz region, (d) Infrared region, and (e) Optical region. [11]

duced transparency, super lensing etc. [8,9,10]. Figure 1.3 shows imaging using MMs in the radiofrequency, microwave, terahertz, infrared, and optical regimes. While initially 3-dimensional metamaterials were widely reported, in recent times 2-dimensional planar metamaterials, or metasurfaces, have gained prominence due to ease of fabrication and analysis. The simplicity of the geometry also makes metasurfaces attractive for research as compared to bulky metamaterials. However, the terms MMs and metasurfaces are often used interchangeably.

The frequency ranges between 1 and 3 THz, represent a region that is a breakpoint between magnetic and electric response in conventional materials. At lower frequencies, inherently magnetic response can be found while at higher frequencies, nearly all materials show an electric response. MMs have been useful in harnessing this THz frequency range. By scaling down the structures to micrometres and using optical lithography, and electron lithography techniques, SRR having resonances in the terahertz frequency range has been widely examined.

1.2.1 Terahertz metamaterials

With the advent of THz technologies, MM research to explore this exotic regime has seen a considerable rise. MMs, consisting of meta-atoms and meta-molecules specifically designed to demonstrate resonances in the THz frequencies, have exhibited a wide range of applications including sensing, switching, modulators, electromagnetically induced transparency, polarization conversion, bound state in continuum, and communication amongst others. There has been applications of THz MMs for bio-medical applications as well. Recently, THz MM sensors for early detection of cancer through basal cell, breast cell, etc., has been reported via the use of a gold nanoparticle based MM [12] . Further, a THz MM consisting of four metallic split ring resonators (SRR) could determine the concentration of carcinoembryonic antigen (CEA) [13]. The different types of resonance phenomena in THz MMs have been elaborately reported in literature [14] . The modulation of the fundamental resonance has been explored via simple MM structures [15] . THz MM waveguides based on air-dielectric groves have been explored with a flexible control on the MM response by tuning the refractive index of dielectric [16]. THz technologies have now found wide relevance in 6G communication applications via use of metasurfaces [17]. The field of terahertz topological photonics using MMs for advances in on-chip communications has also seen wide relevance [18]–[20]. Polarization conversion and wavefront modulation of THz radiation using planar metasurfaces is another important aspect of MM research. MMs have been used to study cross-polarization conversion of THz radiation that could find wide application as THz electromagnetic components. Further, graphene based THz absorbers and polarization converters have also been reported which provides the flexibility of active tuning of MM responses [21]–[23]. Sharp, low-linewidth resonances is an important aspect in the study of sensors, switches etc..The interest in sharp resonances for THz applications has led to several studies on asymmetric Fano resonances, bound states in continuum (BIC), lattice coupled resonances, etc. . The coupling between the inherent first-order lattice mode of a MM and to the hybridized resonance of asymmetric SRR has led to quality factor enhancement of the mode[24]. Quality factor (Q) is defined as a dimensionless parameter equivalent to the ratio of energy stored to the energy lost in a resonator. High Q THz resonance has also been demonstrated by symmetry breaking in metasurfaces leading to the excitation of Fano-type resonance [25]. The sharp fano resonance often forms because of the interference between a broad and a narrow resonance. Using silicon as a photoactive material, the active switching of Fano resonance in THz MM has also been reported [26]. Another type of high-Q resonance is the BIC resonance. BIC modes are stated to be modes with zero radiative losses. However, such ideal BICs are not visible in electromagnetic applications. The property of reduced loss is utilised in quasi-BIC configurations where metasurfaces manipulate radiation to demonstrate very high Q

BIC. Symmetry breakage in dielectric metasurface has also resulted in a leaky sharp BIC mode [27]–[29]. The importance of sharp modes for biochemical and biosensing applications leads to a demand for high Q resonance-based THz MMs. Radiative losses prove a major setback to THz device applications. Toroidal resonance is one such type of low-loss excitation. The property of toroidal resonances demonstrating low radiative losses and high Q makes toroidal MMs an alluring subject of study. Toroidal MMs have in recent times proved to be extremely beneficial in the design of low-loss THz switches, sensors, EIT devices for a variety of applications.

1.3 Introduction to toroidal moments

The theory of electromagnetism has dealt with electric and magnetic moments for a long time. The electric dipole moment is a measure of the charge separation of positive and negative charges in an electromagnetic system. The magnetic dipole moment indicates the strength of the magnet or the magnetic field produced in a region. A magnetic dipole moment is excited when current flows in a loop. The electric and magnetic moments had been widely studied and their implications in material properties had been reported. The 'toroidal moment' is a type of electromagnetic excitation that has recently aroused interest in the research community. The toroidal moments are said to be excited when surface currents flow in the form of coils in a toroid shaped geometry. Considering a torus-like geometry, if there are current loops flowing on the arms of the torus (termed as poloidal current loops) such that the direction of current leads to the formation of magnetic moments that are aligned in a head-to-tail fashion, it will lead to the excitation of a toroidal dipole moment along the symmetry axis of the torus. The toroidal dipole moment is the lowest order toroidal moment. The formation of the electric, magnetic, and toroidal dipole moment via the distribution of charge and current is shown in figure 1. 4 [30]. Figure 1.4(a) shows the formation of an electric dipole moment when the positive and the negative charges are displaced by a finite distance. The electric dipole moment (p) is oriented from the negative charge towards the positive charge by convention. Figure 1.4(b) shows the excitation of a magnetic moment on the flow of a current(j) along a loop. The magnetic dipole moment (m) forms according to the right hand thumb rule perpendicular to the loop. Figure 1.4(c) depicts several current loops (j) forming on the arms of a torus. Such loops of currents are termed as poloidal currents. The direction of current flow is such that the resulting magnetic dipole moments are oriented in a head-to-tail

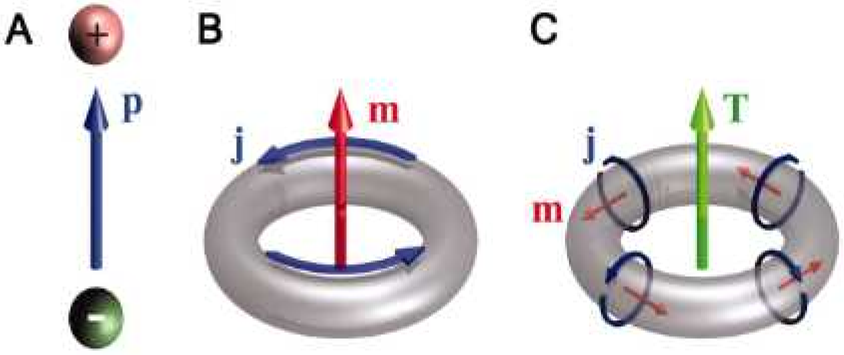

Figure 1.4: The formation of electric, magnetic, and toroidal dipole excitation due to charge and current configurations. (a) Electric dipole formation by positive-negative charge separation. (b) Magnetic dipole moment formation by current flow in a loop. (c) Toroidal dipole moment formation as a result of poloidal current loops in the arms of a torus. From [30]. Reprinted with permission from The American Association for the Advancement of Science.

manner. The alignment of the magnetic moments in this fashion results in the excitation of the toroidal dipole moment (T) along the symmetry axis of the torus. Thus, the toroidal moments provide a complete picture of the electromagnetic excitations in a system and represent an exciting new concept in the field of electrodynamics. The toroidal dipole moment was initially introduced by Zel'Dovich to explain parity violation in nuclear physics [31]. Dubovik in 1967 introduced the concept of toroidal moments, separate from electric moments in solid state physics. The multipole expansion of charge, potential, and current densities in electrodynamics has proven its significance in understanding the physical properties of matter. A Taylor expansion of the transverse part of the vector potential $\vec{A}$ helped in deducing the toroidal dipole moment as, $T_i=\frac{1}{10c}\int[r_i\vec{r}.\vec{J}(r,t)-2r^2J_i(r,t)d^3r]$, where T_i is the toroidal dipole moment, i being the direction (x, y, z) and $(\vec{r},\vec{J})$ indicates the position and current density vectors respectively. Another approach to calculating the toroidal dipole as well as higher order toroidal terms involves solving Maxwell's equations. By solving the inhomogeneous Maxwell's wave equations for electric field and magnetic field by using the Green's function, and further expansion of the Green's function in terms of spherical harmonics provide a solution to the electric and magnetic multipole coefficients. Splitting of the electric multipole coefficient leads to the toroidal terms. The toroidal multipole family is depicted by,

$$T_{l,m}=\frac{k}{l(l+1)}\int j_l(kr^{'})Y^*_{l,m}(\theta^{'},\phi^{'})[r^{'}.J(r^{'})]d^3r, \tag{1.1}$$

where $T_{l,m}$ as mentioned in equation 1.1 indicates the expansion of the toroidal mo-

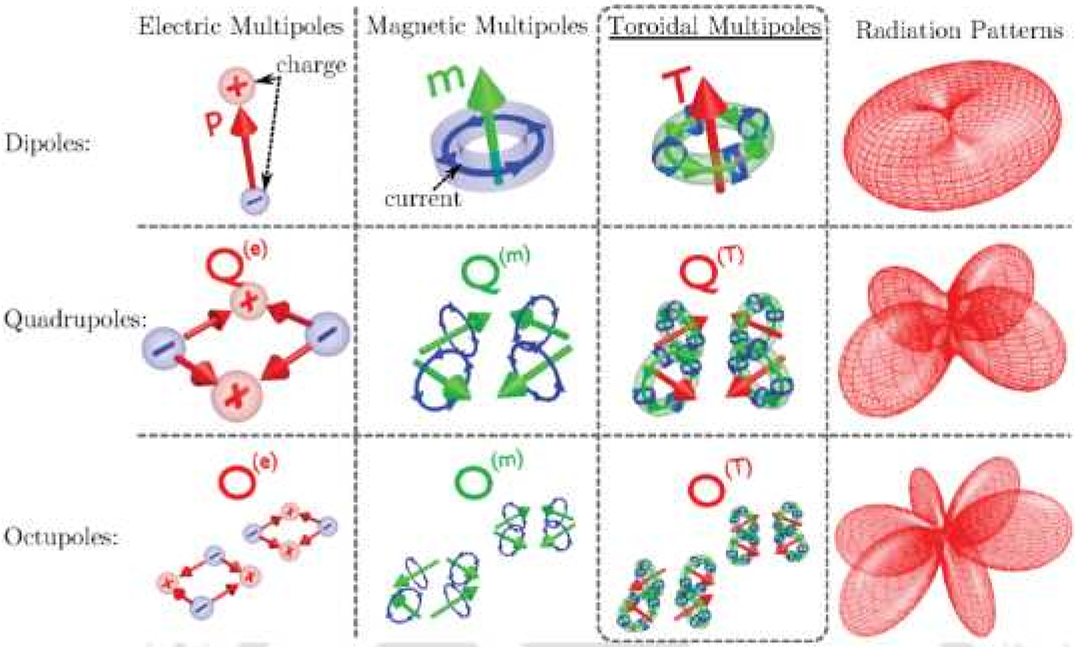

Figure 1.5: A visual description of the electric, magnetic, and toroidal multipoles, i.e., the dipoles,quadrupoles, and octopoles, and their respective radiation patterns. Reprinted figure with permission from [35]. Copyright (2023) by the American Physical Society.

ments, j_l are the spherical Bessel's functions, $Y_{l,m}$ is the spherical vector harmonics, and J(r) represents the surface current density with respect to position, r. The toroidal family is often ignored as there is an extra dependence on the propagation constant, k[32,33]. This indicated that for long wavelengths the toroidal term could often be ignored. The size of structures determined the contribution of toroidal moments in comparison to electric and magnetic moments. The scattering of radiation by electric dipole approximates to $(\frac{R}{\lambda})$, that by magnetic dipole approximates to $(\frac{R}{\lambda^2})$, while electromagnetic scattering by toroidal dipole moment approximates to $(\frac{R}{\lambda^3})$, with R being the length of the dipoles and λ being the free space wavelength. Hence, for smaller structures the radiation scattered by toroidal moment is minimal in comparison to that by electric and magnetic dipole moments. Molecules and systems with toroidal symmetry and relatively large dimensions demonstrate high toroidal contribution [34-36]. The radiation patterns of dipoles, quadrupoles, and octopoles and their formation for electric, magnetic, and toroidal mulitpoles is depicted in figure 1.5.

The initial interest in the study of toroidal moments was due to the wide presence of toroidal symmetries in nature. Besides the existence of toroid-like current configurations in nuclear particles, a number of biological and solid state materials demonstrated

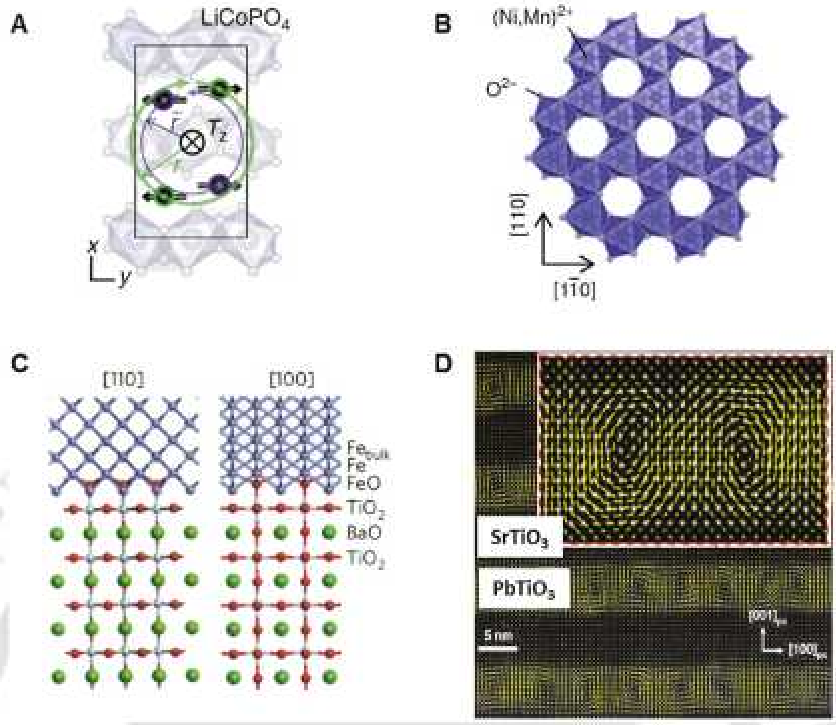

Figure 1.6: The formation of toroidal moment in organic compounds (a) $LiCoPo_4$, (b) Toroidal moment formation in low temperature $Ni_xMn_{1-x}TiO_3(x \approx 0.42)$, (c) Bonding in molecules of Fe and $BaTiO_3$ leading to toroidization at room temperature. (d) Electric toroidal moment observed in oxide supperlattices. [33]

toroidal symmetries. Hence, a curiosity was aroused on the effect of the 'toroidization' due to the clusters of toroidal dipole moment formation at a macroscopic level. Toroidization is equivalent to electric polarization and magnetic dipole density in condensed matter. The density of toroidal dipoles represents toroidization. Macroscopic toroidization in materials is termed as ferrotoroids, similar to ferroelectrics and ferromagnets [5]. Toroidal fullerenes in Chemistry were observed to show toroidal moments [37]. Biological samples involved in DNA binding have been reported to exhibit toroidal nature [38]. Ferrotoroidal signatures were observed in compounds such as $LiCoPO_4$ and spin-glass $Ni_xMn_{1-x}TiO_3(x \approx 0.42)$ [39]. Toroidization at room temperature was also observed in interfaces of Fe and $BaTiO_3$ and in oxide superlattices of $SrTiO_3$ and $PbTiO_3$ [40]. These observations are shown in figure 1.6. Figure 1.6(a) and 1.6(b) shows the toroidal nature in compounds $LiCoPo_4$ and spin-glass $Ni_xMn_{1-x}TiO_3(x \approx 0.42)$ at low temperatures. Toroidization at room temperature using structural modification effects is demonstrated in figures 1.6(c,d) in interfaces of compounds and in oxide supperlattices.

Besides natural molecules and compounds demonstrating toroidal behaviour, the toroidal excitation was observed to be always accompanied by electric dipole excitation. The contribution from toroidal dipole moment was domineered over by the contribution of electric and magnetic moments in natural materials. Therefore, to study the novel properties of toroidal dipole moment, metamaterials and metasurfaces, were designed with toroidal symmetries such that the attributes of the toroidal dipole moment could be scrutinized in detail.

1.4 Toroidal Metamaterial

The toroidal resonances have several advantages including their low radiative-loss property which is crucial in the study of MMs. However, in natural materials, the electric and magnetic dipole moments gain prominence, which overpowers the effect of the toroidal dipole moment. In MMs, the geometry of the meta-atoms can be specifically designed keeping in mind toroidal symmetries. This results in the meta-atoms mimicking toroidal geometries and hence, amplifies the toroidal resonance. The incident radiation that falls on the MM ensures current flow such that the head-to-tail magnetic moment formation takes place, which is a signature of toroidal dipole excitation. The study of toroidal MMs has gained prominence in recent times. The initial studies of toroidal excitations in MMs were based on 3D geometries. The next section discusses the design and study of 3D toroidal MMs in various frequency regimes.

1.4.1 3D toroidal metamaterials

The first experimental study on toroidal resonances in MMs was performed in 2010 by the group of Kaelberer and a sharp toroidal response was observed in the GHz frequency range. They designed a MM structure that deviated from the traditional solenoidal designs and constructed four metallic SRRs embedded orthogonally on a dielectric slab. Flow of circular currents in the metallic loops led to the excitation of the toroidal dipole moment with a Q=240 [30]. The MM design and response is shown in fig 1.7(a). Further studies were performed by various groups in an effort to understand the characteristics of the toroidal dipole resonance. A similar study was performed in the optical domain where using 3D ion-beam folding method, vertical silver split ring resonators were fabricated on a silicon nitride film. The confinement of the magnetic moments leads to toroidal

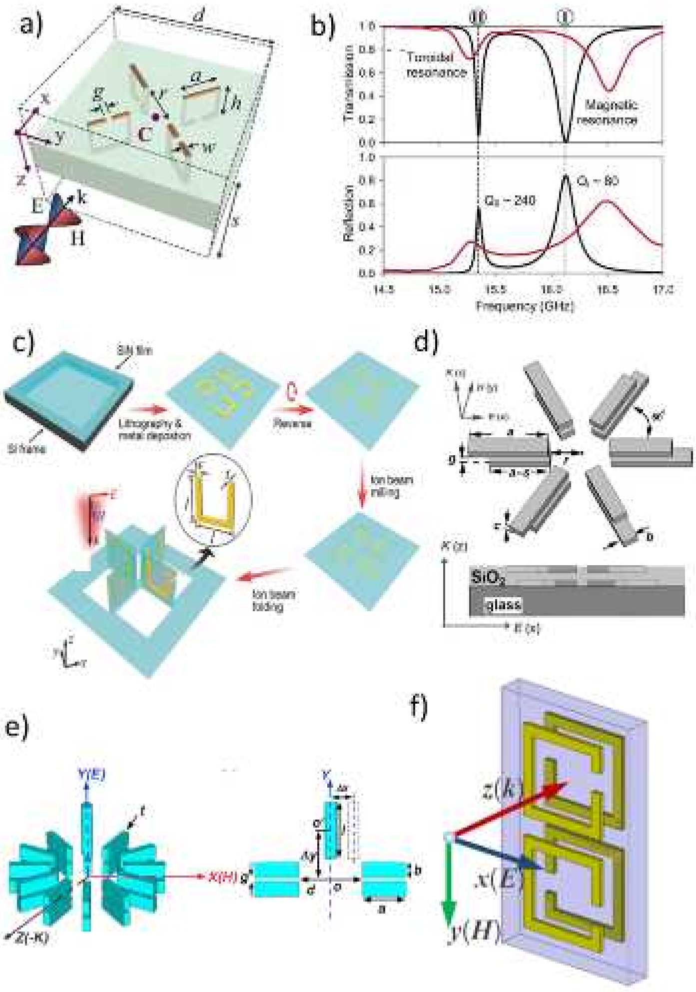

Figure 1.7: Three dimensional metamaterials demonstrating toroidal dipole excitation. (a) The first experiemntally designed toroidal MM [30], and (b) corresponding excitation of sharp toroidal dipole moment[30]. (c) Design of a toroidal MM using vertical SRRs [42]. (d) Demonstration of toroidal dipole excitation in the optical regime usime a double bar MM geometry Reprinted from [45], with the permission of AIP Publishing. (e) 12-fold metal bar geomtery exciting dual toroidal dipole excitation and EIT [43]. f) Stacked MM geometry for enhancing quality factor of toroidal dipole excitation. Reprinted figure with permission from [44] Copyright (2023) by the American Physical Society.

resonance. The highlight of the study was the fabrication technique of the 3D metal-dielectric composite. The toroidal MM structure is depicted in figure 1.7(c)[42]. While vertical SRR based toroidal MMs required lateral incidence of radiation for coupling, normally coupled toroidal MM using asymmetric double bar geometry was presented in the optical range, as shown in figure 1.7(d). Tight confinement of electric and magnetic field confirms the toroidal excitation in the optical range both experimentally and numerically [45]. A 12-fold double metal bar geometry was also reported that demonstrates dual toroidal moments in the optical domain along with an electric dipole moment. The destructive interference between the two modes also results in an analog of EIT [43]. The MM design is shown in fig 1.7(e). Enhancement of Q factor in the GHz range has been reported through stacked SRRs in a four-SRR metamolecule configuration [44]. Fig 1.7(f) demonstrates the stacking of the resonators leading to an enhanced Q factor.

3D toroidal MMs demonstrated a number of applications across the optical and microwave regimes. However, for high frequency domains, smaller micro and nano-sized meta-atoms need to be fabricated. The fabrication of 3D MMs is often complicated. Stacked MMs require a high degree of accuracy in the fabrication process. Hence, studies on planar toroidal metasurface have become relevant in recent times. The next section discusses the study of planar toroidal MMs.

1.4.2 Planar toroidal metasurfaces

The importance of ease of fabrication and scalability in MM, as well as simple simulation designs were prime concerns for the shift from 3D toroidal MMs to planar MMs or metasurfaces. Several studies have been performed across different frequency regimes on the excitation of toroidal resonance in planar MMs. The excitation of a very high Q 'anapole' resonance was reported in the GHz range [46]. The anapole excitation is a non-radiative type of excitation that takes place due to the interference between a toroidal dipole moment and an electric dipole moment. The sharp toroidal resonance is believed to be a result of the perfect cancellation of the electric dipole moment by the toroidal dipole excitation. Toroidal excitation has also been demonstrated in the near-infra red domain in an all dielectric metasurface [47]. The planar metasurface consists of molecules made of four silicon discs of millimetre dimension. Introduction of an asymmetry in the metasurface leads to a strong toroidal dipole moment. An all-dielectric disc oglimer type planar metasurface has also shown efficient toroidal moment in infrared wavelengths. Several configurations of the dielectric discs are suggested which ensures the diversity of MM designs for optical applications [48]. In the field of biological applications, a toroidal resonance in the GHz range has been utilized in the sensing of Zika virus envelope protein in room temperature [49]. The next section discusses the toroidal excitations examined in planar metasurfaces.

1.4.3 Planar toroidal terahertz metasurfaces

The terahertz range of frequencies are being explored widely for a variety of light-matter applications. In an effort to combine the unique properties of toroidal resonances to the characteristics of THz radiation, toroidal metasurfaces are being specifically designed to demonstrate resonances in the THz regime. Toroidal metasurfaces have demonstrated applications including high-Q metasurfaces, switches, bio-sensors etc. This section summarises some of the recent studies undertaken in the field of toroidal terahertz metasurfaces.

The shift from 3D MMs to 2D metasurfaces was a major turning point in the study of toroidal terahertz photonics. Though 3D geometries provide better magnetic field confinement, the 2D metasurfaces can be designed very carefully to ensure suppressed electric, and magnetic moment with domineering toroidal effect. In this respect, a study was reported on a planar toroidal geometry where two joint metallic loops with capacitive gaps in each loop where brought together in the form of a meta-molecule with resonances in the THz regime [50]. The metasurface geometry is demonstrated in figure 1.8. By varying the position of the capacitive gaps domineering toroidal behaviour was established in the MM. The distance of the SRR arms was varied from the central resonator arm and it was observed that at an optimal distance 'd'of 7μm the toroidal excitation was highest. This was followed by the study of the surface current profile and magnetic field profile in the metasurface for varying d. The surface current and magnetic field profiles confirmed the excitation of toroidal dipole moment for an optimum value of the distance of the capacitive gaps from the central arm .

Further, applications of toroidal excitation in sensing, switching and singleband EIT has also been examined [41-70, 118-124]. The single band EIT has been demonstrated in an asymmetric metasurface consisting of two J shaped metallic SRRs [53]. The surface current profile is elaborated to explain the toroidal effect. By tuning the length of the resonators, a single band EIT window is reported. The underlying asymmetry in the

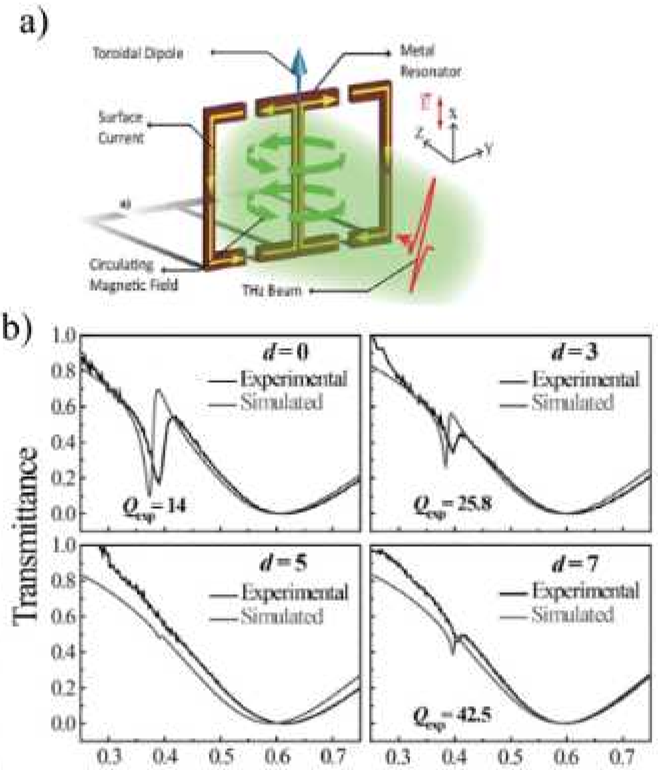

Figure 1.8: (a) The metasurface geometry that demonstrates sharp toroidal resonance in the terahertz region. (b) Transmission for varying distance 'd' between the resonator arms. [50]

design of metasurface leads to excitation of EIT. Chapters 3 to 7 of this thesis highlights several works on toroidal excitations in metasurfaces. However, despite these reports there lies significant gaps in the study and interaction of toroidal excitations in THz metasurfaces and its applications. This thesis attempts to address certain such gaps in the field of toroidal metasurfaces in the terahertz domain.

1.5 Identification of toroidal excitation in metasurfaces

The identification of a toroidal excitation in a metasurface is done using three major techniques, i.e., the study of the surface current profile, study of magnetic field profile, and multipole analysis. This section elaborates the procedures for identification of toroidal dipole resonances in metasurfaces.

1.5.1 Surface current profile

The surface current profile is one major way of identifying the toroidal dipole nature of an electromagnetic excitation. The excitation of a toroidal dipole resonance required the magnetic moments to be arranged in a head-to-tail fashion. When electric current flows in a loop a magnetic moment excites according to the right-hand thumb rule. When metasurfaces are excited by an incident electromagnetic radiation, it is ensured the electric field polarization of the incident beam is such that circular loops of current are formed in the metasurface for toroidal dipole excitation to take place. The metasurface is often designed in such a manner that two current loops form. When the two current loops are oriented in opposite directions, i.e., if in one loop of current flows clockwise while the other current loop flows anticlockwise, magnetic moments also form with opposite orientation. Such an opposite orientation of magnetic moments becomes the planar analogue for head-to-tail moment formation. The direction of toroidal dipole excitation can be determined again by the right hand thumb rule, where the extended fingers indicate the direction of magnetic moment coming out of the plane and the thumb indicates the direction of the toroidal dipole excitation. Fig 1.9 (a) demonstrates the circular flow of surface current and excitation of toroidal dipole moment in a planar metasurface.

1.5.2 Magnetic field profile

The magnetic field profile of a metasurface is another way of confirming the toroidal excitation in a metasurface. Once the surface current flow indicates the toroidal dipole resonance, the magnetic profile is analysed by studying the lateral view of the metasurface. The circular head-to-tail configuration of the magnetic moments are considered proof of toroidal dipole excitation. This is indicated in figure 1.9(b).

1.5.3 Multipole Analysis

The multipole analysis is an excellent tool to identify the different kinds of electromagnetic excitations in a metasurface. It involves breaking down the power scattered by the metasurface into the component contribution by the electric, magnetic, toroidal, and quadrupole moments. The power scattered by the different electromagnetic moments are derived from the current density information that is generated in a metasurface when

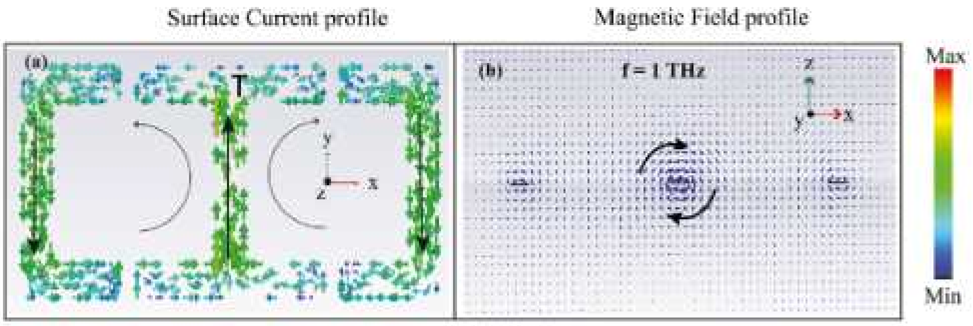

Figure 1.9: (a) The flow of surface current in the a metasurface for excitation of toroidal dipole moment. The surface current flows clockwise on the right arm of the resonator and anticlock wise on the left arm. (b) The head to tail alignment of magnetic moments for toroidal dipole excitation.[54]

radiation is incident on it [55,60]. The power radiated by each individual moment i.e., 'WP','WT' and 'WM',WQ$_m$, and WQ$_e$ respectively, for electric, toroidal, magnetic dipole moment, and magnetic and electric quadrupole moment is given by,

$$WP = \frac{2\omega^4}{3c^3}|P|^2, \tag{1.2}$$

$$WT = \frac{2\omega^6}{3c^5}|T|^2, \tag{1.3}$$

$$WM = \frac{2\omega^4}{3c^3}|M|^2, \tag{1.4}$$

$$WQ_m = \frac{\omega^6}{40c^5}\Sigma|MQ_{\alpha\beta}|^2, \tag{1.5}$$

$$WQ_e = \frac{\omega^6}{5c^5}|EQ_{\alpha}\beta|^2, \tag{1.6}$$

where the angular frequency of incident radiation is represented by ω, speed of light in vacuum is given by c, P, T,M and Q represents the electric, toroida, magnetic dipolar moments, and the quadrupole moment calculated using the surface current data. By plotting the power scattered by the different electro-magnetic moments over the desired frequency range, a quick and easy evaluation of the toroidal contribution can be performed for the metasurface. The multipolar analysis is often used as a tool for confirmation of the toroidal excitation after studying the surface current profile and magnetic field profile.

1.6 Important concepts relating to the thesis

This section provides a very brief overview of certain topics that have been discussed in the thesis.

1.6.1 Electromagnetically induced transparency

The electromagnetically induced transparency (EIT) is a quantum phenomenon involving three level systems where an absorbing medium becomes transparent to the incident light. Inducing transparency in an otherwise absorptive spectrum has garnered a considerable interest of the scientific community in the last decade because of its significance in constructing photonic components such as slow light systems, buffers and tunable filters [84,85, 56]. However, to experimentally realise EIT requires very specific environments. Specific experimental conditions including constraints on temperature and high intensity pumping has led to the exploration of classical alternatives to the EIT phenomenon [85]. In comparision, the classical analogue of EIT, termed as plasmon induced transparency, is often explored using metasurfaces. The study of EIT in metasurfaces usually involves the coupling between a dark resonator and a bright resonator. A dark resonator is one which doesn't directly couple to the incident electromagnetic radiation. In contrast, the bright modes are the resonators that directly couple to the incident radiation. Within the transparency window, the medium becomes highly dispersive. On the other hand, another method of introducing a transparency region in a metasurface is by coupling bright-bright resonators. The bright-bright mode coupling of resonators also results in the excitation of tranparency windows. The transparency region can be excited in a single window or on multiple windows depedening on the metasurface geometry and near-field coupling of the resonators. The excitation of one transparency window is termed as a "Single band EIT". A single band EIT is excited when a bright mode at a fixed frequency couples to a dark mode at the exact same frequency. To introduce two transparency windows, or a "dual-band EIT" another resonator at a nearby resonant frequency is coupled to the metasurface geometry leading to the excitation of two transparency windows. Further, the near-field coupling to higher number of resonators in a similar fashion leads to the excitation of "multiband-EIT" windows. A larger number of EIT windows provides the added flexibilty of high regions to study the light-matter interactions and broader regions to explore the effects of slow-light, high dispersion etc. Chapter 5 of this thesis discusses the excitation of EIT in toroidal metasurfaces in details.

1.6.2 Polarization conversion of incident radiation

The direction of polarization of the incident radiation forms an important part of the studies highlighted in this thesis. In the context of this thesis, the term "polarization" of radiation indicates the direction of the electric field of the incident THz radiation falling on the metasurface. The terms "co-polarized" and "cross-polarized" radiation is frequently used in the studies. Co-polarized radiation indicates the incident radiation that is polarized parallel to the split gaps of the resonatos. The cross-polarized radiation signifies the radiation that is orthogonal to the co-polarized radiation, i.e., it is perpendicular to the split gaps of the resonators. The thesis also deals with the term "polarization-indepedent". The term polarization independence indicates that the metasurface property is observed independent of the polarization direction of the incident radiation, i.e, the properties of the metasurface does not depend on whether the electric field of the incident radiation is co-polarized or cross-polarized. The polarization of radiation hence, is a very important parameter when studying the applications of a metasurface. Chapter 6 of the thesis discusses a terahertz metadevice that converts radiation from the co-polarized component to the cross-polarized component.

1.6.3 Tunable response in metasurfaces

Tunability of a metasurface indicates the ability to modify or adjust the properties of a metasurface. The thesis involves studying the modulation of the properties of the designed metasurfaces by various techniques. One method of varying the metasurface properties is by changing the physical structure of the meta-atoms. Changing the physical structure of a resonators, including the length, capacitive gaps etc., is termed is the passive tuning of a metasurface. Despite obtaining desired modulation of the MM properties, passive tuning increases fabrication efforts as it requires multiple devices of varying parameters. The active tuning of a metasurface is the modulation in the properties of the MM without actually making any change in the dimensional parameters of the resonators. Active tuning of the metasurface properties, in this thesis, is performed by introducing graphene in the MM. By varying the fermi-energy, and relaxation time of graphene, the response of the metasurface is modulated. The fermi-energy can be varied by externally appplied volatage in the metasurface. This is explained in detail in chapter 4. Similar active modulation of a metasurface properties can also be achieved by photo-excitation of silicon-dioxide layer. Thus, the tunability of a metasurface forms an important part in the study of MM properties and responses.

1.6.4 Lattice Coupled Resonance

The lattice mode is a resonance mode inherent to the MM. It is often a dark mode that arises due to diffraction along the interface of the periodically arranged meta-atoms of a metasurface. The energy transmitted in the metasurface is strongly confined to the surface, which acts similar to a trap, and reduces the far-field radiation [112]. The periodicity of the MM controls the resonant frequency of the lattice mode. The first order lattice mode is given by, $f_L = \frac{c}{nP}$, where f_L is the lattice frequency, 'c' is the speed of light in vacuum, 'P' is the periodicity of the metasurface, and 'n' is the refractive index of the substrate. Thus, the resonance of the MM can easily be coupled to the lattice mode by varying the periodicity of the MM. The coupling between the MM resonance and the lattice mode has led to extremely high narrowing of resonance linewidths leading to very high-quality factor (Q) resonances and lowered radiative losses [112-118]. In the seventh chapter of the thesis, the lattice mode is discussed in detail and the coupling between a lattice mode and a toroidal mode is analyzed.

1.7 Outline of the thesis

In this thesis, the excitation of the toroidal dipole resonance has been discussed in the THz frequency range and its applications have been elaborated. The thesis delves into several geometries of metasurfaces for the excitation and interaction of toroidal resonance. The passive tuning and active modulation of the toroidal resonance is explained. Further, the excitation of EIT in a toroidal MM is discussed. The application of toroidal THz metasurfaces as a broadband polarization convertor, and for inducing sharp lattice coupled mode, independent of the polarization of incident radiation, has also been addressed. The work has been organized into eight chapters in this thesis. A chapter-by-chapter description of the thesis is provided below:

Chapter 1 provides an overview of the thesis as a whole. It discusses in detail about terahertz radiation, its uses, and advantages. Metasurfaces and their applications have been explained in this chapter. The toroidal dipole resonance in 3D MMs and 2D metasurfaces has been discussed and their identification in MMs has been reported. The terms that find repeated mention in the thesis has been discussed in this chapter.

Chapter 2 provides the methodology for the thesis. It discusses the design of planar metasurfaces using CST simulation software and their fabrication using photolithography. Further, the terahertz characterization of such metasurfaces using THz-TDS is explained in this chapter.

Chapter 3 discusses the excitation of a toroidal dipole resonance in a THz MM. The interaction between dual toroidal resonances in the bilayer MM geometry is explored. The modulation and switching of the dual resonances into a single toroidal resonance is reported. A Lagrangian approach is used to suggest the coupling between the toroidal resonances.

In **Chapter 4**, the toroidal dipole response in a graphene based 2D THz metasurface is explored, and the active tuning of the toroidal resonances are discussed. The MM configuration is made of graphene based joint split ring resonators (SRRs). The actively tunable response of the toroidal excitations is examined with respect to a change in the Fermi energy of graphene material. The relaxation time is further modulated and the MMs response to the Q factor is studied. Such dynamically controllable toroidal excitations could be significant in designing efficient tunable modulators, filters and sensors.

Chapter 5 discusses the excitation of EIT in a toroidal THz metasurface. Initially, the excitation of a single band EIT is explored, which is then extended to the excitation of multiband EIT windows. The metasurface geometry consists of a toroidal split ring resonator (TSRR) flanked by two asymmetric C resonators. The strong near field coupling of the toroidal excitation with the dipolar C-resonators of the meta molecule results in dual-band transparency windows in the THz region. The frequency modulation of transparency windows is examined by changing the separation between TSRR and the C resonators. The numerically simulated findings were interpreted and validated using an equivalent theoretical model based upon three coupled oscillators system. Such multiband EIT systems can impact the development of terahertz toroidal devices for next generation photonic systems.

Chapter 6 explores the experimental application of toroidal dipole excitation in the broadband polarization conversion of THz radiation. The linearly polarized state is converted to an orthogonally polarized state via the toroidal metasurface. The meta-atoms comprised of a simple single SRR based geomtery. The X and Y components of transmission for numerous in-plane rotations of the proposed geometry was studied. Polarization conversion of nearly 40% was observed over a THz band of 1.19 to 2.5 THz. Such a broadband cross-polarization converter is significant for the development of terahertz toroidal metamaterial devices.

Chapter 7 discusses the coupling of a toroidal resonance to the inherent lattice mode of a metasurface, both numerically and experimentally. The design of the metasurface is such that the lattice-coupled toroidal excitation is independent of the polarization direction of the incident THz polarization. The Q factor is enhanced for both the X and Y polarized components. Such a polarization independent lattice-coupled toroidal metadevice could be significant in the development of low loss THz photonics components.

Chapter 8 summarises the findings of the research work elaborated in the thesis and further discusses the future scope of toroidal THz metasurface in the context of the findings that have been reported.

CHAPTER 2

METHODOLOGY

This chapter discusses the techniques and methods used in our studies. A project involves three main steps: design and simulation of the metasurface, fabrication of the metasurface, and finally characterization of the fabricated samples. A match between the simulated and experimentally obtained results is necessary for the study to be considered correct. Section 2.1 explains the simulation tool and technique used in our studies. Section 2.2 discusses the fabrication methodology, while section 2.3 discusses the characterization of the fabricated metasurfaces.

2.1 Design of the metasurface

The metasurfaces in the thesis has been designed using the commercially available simulation tool CST (Computer Simulation Technology) Microwave Studio simulation software. CST is a powerful software that allows the design, optimization and the electromagnetic analysis of electromagnetic components. The software solves the Maxwell's equations for a given structure with defined boundary conditions and evaluates the transmission, reflection, and absorption coefficients for the structure in an uncomplicated procedure. CST uses the "finite integral technique" to perform the numerical simulations. The finite integral technique involves solving the integral form of the Maxwell's equations for a suitable volume or domain. CST provides various solvers including transient solver, frequency domain solver, and Eigen-frequency solver. The frequency domain solver is

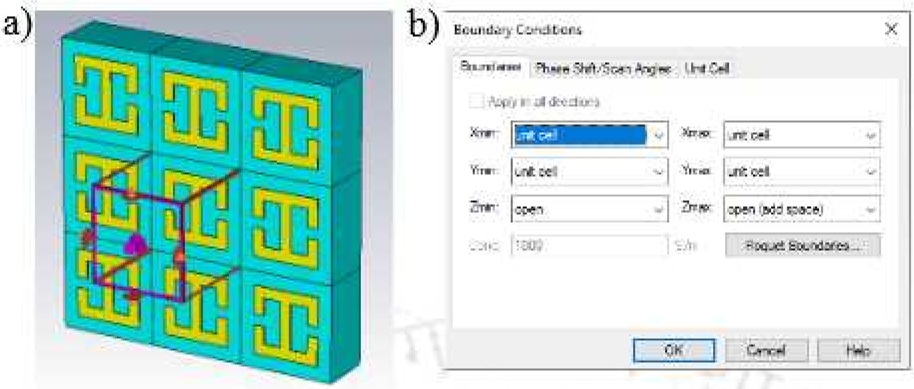

Xmin: unit cell
Xmax: unit cell
Ymin: unit cell
Ymax: unit cell
Zmin: open
Zmax: open (add space)
Cond.: 1000 S/m

Figure 2.1: (a) View of a metasurface array designed using CST Microwave Studio simulation software.Boundary condition is set for each unit cell. (b) Snapshot of the boundary conditions set for the MM along the X, Y, and Z axes.

useful for simulation of subwavelength geometries of small dimensions and for periodic arrays. Hence, for modelling the metasurfaces of our studies, the frequency domain solver is an adequate technique. The frequency domain solver performs calculation for each frequency over a broadband domain. The metasurface array is divided into unit cells and an automatic meshing is done by the software. Each unit cell is divided into small tetrahedral grids of size $\lambda/10$, λ being the wavelength of the incident radiation. This "tetrahedral meshing" is set automatically in the frequency domain, but can also be modified at will. The better the meshing of the metasurface, the more accurate results are obtained. For the design of the metasurface array, a new project template is created in the microwave and RF/optical domain with selection of periodic structures as the type of design. Metamaterial full structure is chosen as the workflow and the frequency domain solver is used. After selecting the frequency domain solver as the requisite solver, the frequency range for simulation is defined. Next, CST provides an interface to define the unit cell of the metasurface array and the dimensional parameters can be easily defined. Once the length, breadth, periodicity, and other dimensions are defined, and the geometries are built, materials can be added to the structures. CST has an extensive material library for most materials including metals (gold, silver, aluminium) and a varying range of dielectrics that are based on Drude or Lorentz models and replicates the properties of the materials. To numerically mimic the metasurface array, boundary conditions are set that best defines the MM in question. Figure 2.1 (a) shows the designed MM array in the CST window, while figure 2.1(b) demonstrates the setting of "unit cell" boundary conditions in a MM. "Unit cell" conditions are defined in the

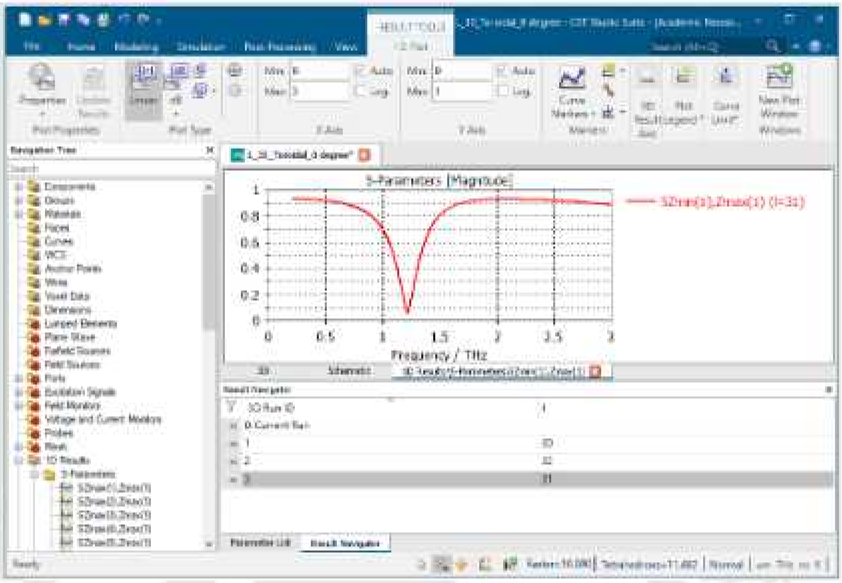

Figure 2.2: The CST interface for metasurface smulation depicting the transmission plot for a frequency range of 0.2 THz to 3 THz.

XY plane and further, the probe and source is defined by setting Z(max) as open (add space) and Z(min) as open. Once the boundary conditions are defined, CST solves the Maxwell's equations for the unit cells after a proper meshing. The frequency domain solver transforms the equations solved for each frequency into its Fourier transform and the computed transmission and reflection coefficients are stored in the S-matrix. The S_{11} term of the matrix, given by (SZ_{Max}(1),Z_{Max}(1)) defines the reflection coefficient at port 1, where the coefficients 1 and 2 represent the ports 1 and 2. The S_{21} term of the matrix, given by (SZ_{Min}(1),Z_{Max}(1)) defines the transmission coefficient. The simulation of the metasurfaces for linearly polarized light is performed in all our studies. The substrate for our studies have been chosen as silicon or quartz with dielectric permittivity $\varepsilon_r = 11.9$ and $\varepsilon_r = 3.75$ according to experimental availability. Figure 2.2 shows the interface of CST when obtaining the transmission for a metasurface array.

2.2 Fabrication of metasurfaces

The metasurfaces fabricated for this thesis involved both electron-beam lithography and photolithography in a standard cleanroom environment, while photolithography was preferably used. The dimensions of the structures fabricated are in the micrometre scale such that resonances at 0.1 to 2 THz are observed. Here, the processes involved in the metasurface fabrication using photolithography is mentioned below:

1 Substrate sterilization: The first step of fabrication involves thorough cleaning of the substrate to remove any external particles present on it. The presence of dust or any other particles results in inefficient adhesion of deposited chemicals on the substrate. The substrate is cleaned with acetone and then washed with isopropanol to remove all traces of the acetone. It is then dried using dry nitrogen gas to remove all moisture. Further, it is heated at 175^0C for 10 minutes.

2 Metallization: The substrate is deposited with the required metal (gold or aluminium) using a thermal evaporator. The substrate is baked for 10 minutes at 30^0C.

3 Resist deposition: The substrate is coated with HMDS (hexamethyldisilazane) solvent using a spincoater at an 4000 rotation per minute (RPM) to ensure adhesiveness of the photoresist and then, the substrate is heated at 175^0C for 15 minutes . Next, positive photoresist S1813 is spincoated on the substrate at 3500 RPM and is heated for 5 minutes at 130^0C after the coating is done to harden the coated resist.

4 Patterning: The subtrate is patterned with the desired designs using a suitably designed hard mask. The exposure is done via illumination of the substrate with UV light through the hard mask in a mask aligner or UV box. The aligner is set such that a hard contact between the substrate and the mask is maintained.

5 Development: The patterned substrate is developed in a developer solution (SU8) by dipping the sample in the solution rinsing it with deionized (DI) water. The area exposed to UV light is dissolved away while the rest of the photoresist remains intact, such that the desired pattern is printed on the substrate. It is ensured that no trace of the photoresist remains on the exposed area.

6 Etching: The desired MM array is achieved by etching the developed sample with an etchant for corresponding to the metal deposited. Once the extra metal and resist are etched away, the required metalized array is printed on the substrate and the metasurface is obtained.

The steps involved in the fabrication of a metasurface is illustrated in figure 2.3.

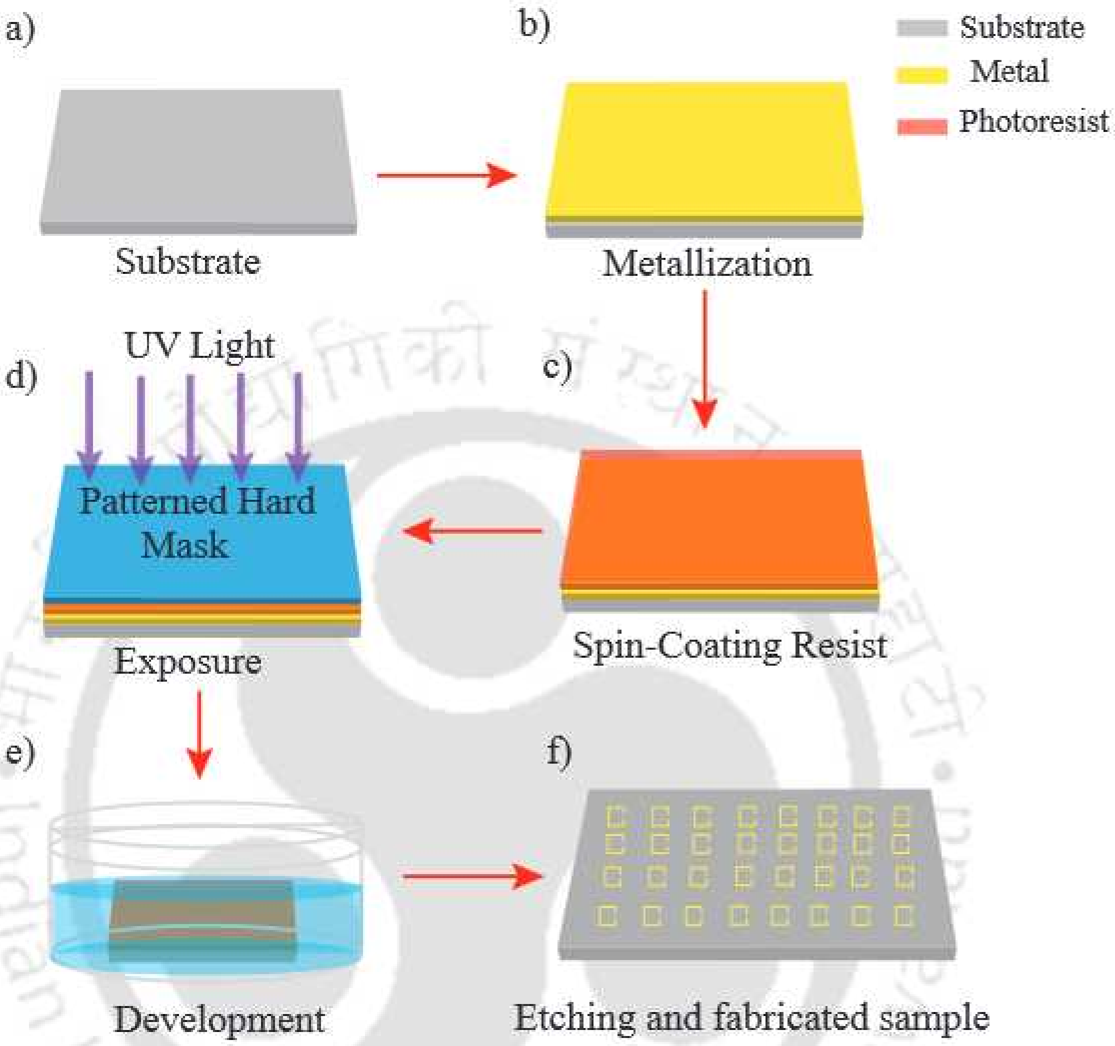

Figure 2.3: Steps involved in the fabrication of a THz metasurface using photolithography technique.

2.3 Characterization of metasurfaces

The metasurfaces fabricated for our studies have been characterized using a terahertz time-domain spectroscopy setup. There can be several ways of generating and detecting THz radiation inlcuding photoconductive antenna (PCA), electro-optic sampling etc.. The setup we have used is based on PCAs for both generation and detection of THz radiation.

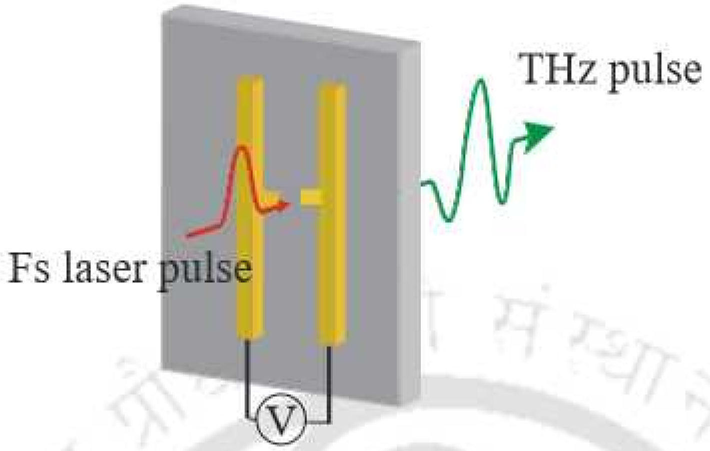

Figure 2.4: Schematic depiction of a biased photoconductive antenna emitting THz radiation.

2.3.1 Terahertz Time-Domain spectroscopy (THz-TDS)

The terahertz time-domain spectroscopy (THz-TDS) is a powerful technique to analyze and characterize samples. THz-TDS provides direct measurement of the electric field in the THz frequency. The measurement of the electric field of the THz pulse leads to information about the amplitude and phase of the waveform. Several methods can be used in a THz-TDS system for the generation and detection of THz waves. For characterization of our samples, a photo-conductive antenna (PCA) based setup is used. PCAs are widely used for THz generation and detection because of their functionality at low power of lasers and low cost. The generation of THz pulses in a PCA takes place by photo excitation of photo carriers, induced by an ultrafast laser. The PCAs are designed on a semi-conductor substrate of semi-insulating low-temperature Gallium Arsenide. Gallium Arsenide is a suitable material due to its low charge carrier life time, high damage threshold and, and high mobility of electrons. The PCAs designs consists of parallel metal electrode strips on the Ga-As substrate with a small gap in between the two strips. The gap area stores the electric energy generated from the antenna. Fig 2.4 shows a schematic of a PCA used for generation and detection of THz waves. Figure 2.5 demonstrates a THz time domain signal and the corresponding frequency domain signal. An ultrafast laser having pulse energy higher than the bandgap of the substrate material strikes the gap of the PCA generating photocarriers. The PCA is biased by an external voltage E_b, as a result of which the photocarriers move and generate a current. The current density can be described as J(t)= N(t)$e\mu E_b$, N being the density of the carriers, e is the electric charge,

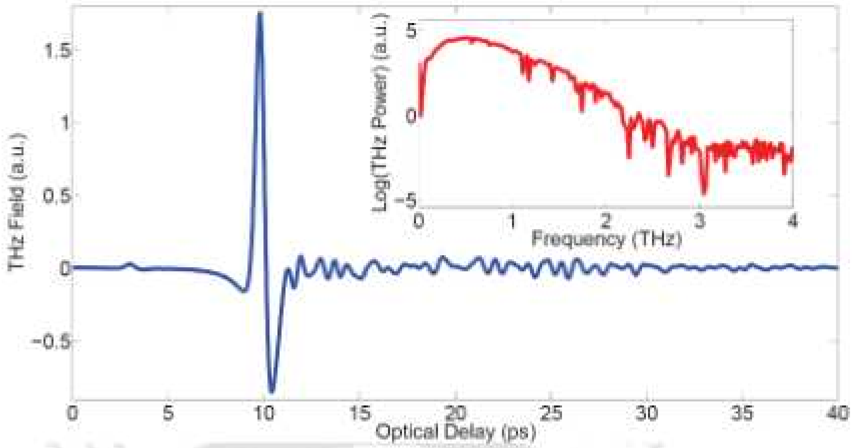

Figure 2.5: The terahertz time-domain signal over a time delay. Inset shows the corresponding frequency domain signal over a band of 4 THz [119].

μ is the mobility. The time-varying current radiates the terahertz waves, whose electric field amplitude is given by $E_{THz}= \dfrac{Ae\mu E_b}{4\pi\epsilon_0 c^2 z}\dfrac{\partial N}{\partial t}$, A being the illuminated area [21]. The setup for THz-TDS for our studies consists of a femtosecond laser of central wavelength 780 nm, 100 MHz repetition rate, and pulse width of 100 femtosecond. The setup is purged with dry nitrogen gas to eliminate moisture. A schematic of the THz-TDS setup described is depicted in figure 2.6. The laser beam is split into two parts using a beam splitter - the pump and the probe beam. The pump beam (with high power component) is used for THz generation, while the probe beam is used for THz detection. The pump beam hits the 5 μm gap of the PCA and generates THz radiation. The triggering of the optical pulse in the gap region results in the release of energy in the form of a THz pulse. The refractive index of low temperature Ga-As is 3.6 while that of air is 1, hence the large mismatch is overcome by using hyper-hemispherical silicon lens to couple the THz radiation to free space. The THz radiation is then collimated and passed through the sample. The terahertz pulse transmitted through the sample is then guided towards the detector PCA, coupled to a silicon lens, using another parabolic mirror. In the detection mechanism, the transmitted THz radiation acts as the external biasing field. The second part of the femtosecond beam, the probe beam, is used to map the detected THz field. Since the THz beam is of picosecond timescale, the femtosecond beam is passed through a delay stage to ensure correct mapping. The carriers generated by the probe beam moves under the biasing of the THz field, producing a photocurrent given by J = Neμ E(τ), τ being the temporal delay between the THz and probe beams and $E(\tau)$ being the THz field. The photocurrent that is generated is very small, of the order of nano ampere

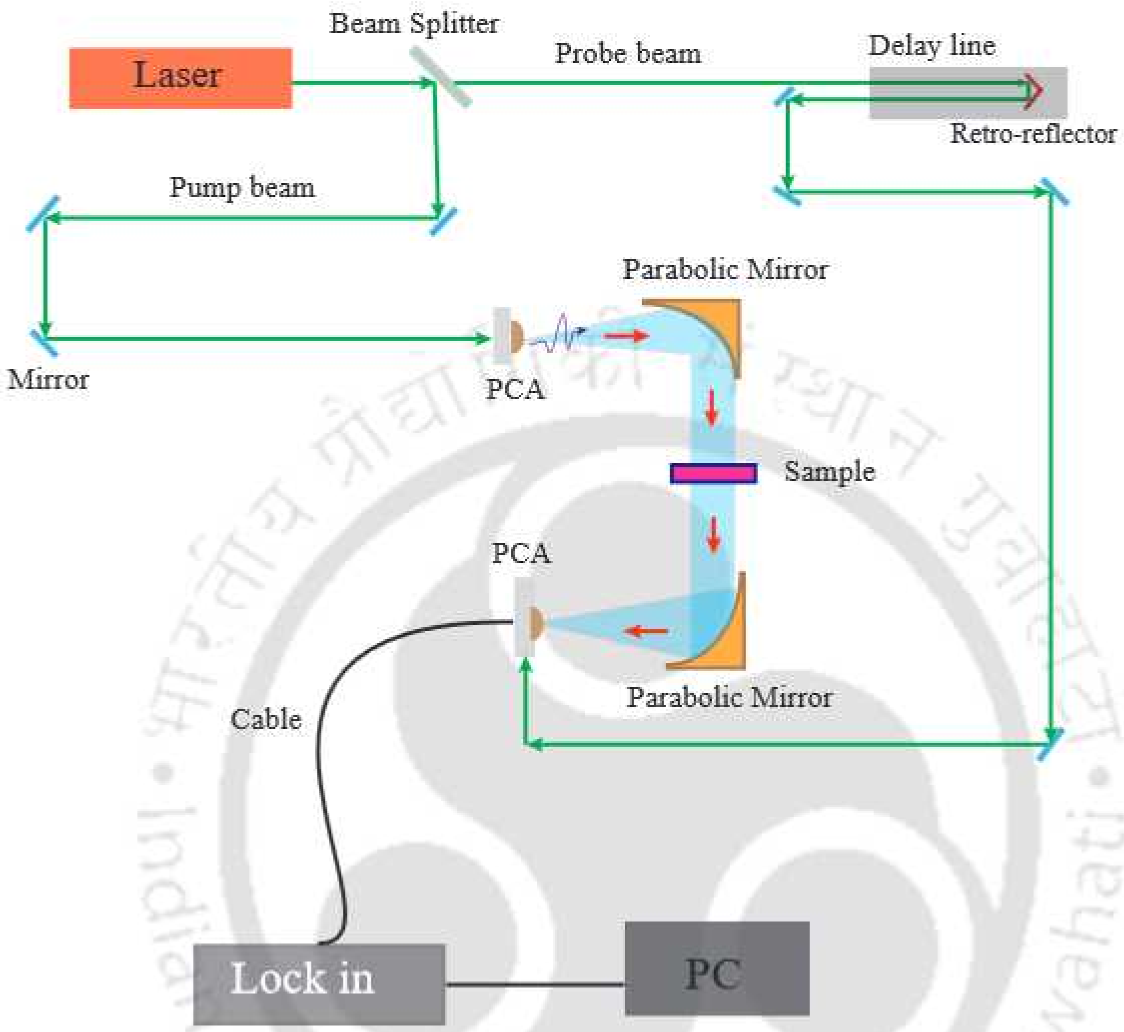

Figure 2.6: Schematic of a THz-TDS setup using a femtosecond laser and PCAs for generation and detection of THz radiation.

and hence, a current amplifier is utilized to record the data. Recorded photocurrent data gives direct mapping of E(τ) as a function of τ, through which the profile of the terahertz pulse is obtained. Instead of the intensity of the terahertz waves, the THz-TDS method provides direct measurement $E(\tau)$, i.e., the amplitude and phase information, instead of the intensity. This facilitates the evaluation of the complex refractive index of the sample. For experimental analysis, a reference scan is usually measured for the substrate of the metasurface, termed as $E_R(\omega)$. The measured field of the sample is termed as $E_S(\omega)$. The transmission amplitude, $T(\omega)$, is the ratio between the field of sample and field of reference, $T(\omega) = \dfrac{E_S(\omega)}{E_R(\omega)}$).

The first few studies of this thesis are based on numerical analysis, while experiment has been performed on the studies of terahertz polarization convertor and lattice-coupled toroidal mode discusses in chapters 6, and 7, respectively. The numerical and experiemntal strategies discussed in this chapter is utilized throughout the thesis. The following chapters discuss various studies on metasurfaces using different meta-atom designs for applications in THz photonic devices.


भारतीय प्रौद्योगिकी संस्थान गुवाहाटी
Indian Institute of Technology Guwahati

CHAPTER 3

INTERACTION OF TOROIDAL RESONANCES IN COUPLED TERAHERTZ METASURFACES

In this chapter, we aim at establishing a basic method of exciting toroidal resonances in a terahertz metasurface and discuss the interaction between two toroidal dipole resonances in a bilayer terahertz metasurface. A passive modulation in the interaction, and eventaul switching from a coupled to an uncoupled system is also analyzed. Dual toroidal excitations and near field coupling between resonances can provide an extra degree of freedom to control and manipulate resonance properties. The interaction between layers of toroidal dipolar moments in near field configuration has been limited to near and mid-infrared frequencies and focus has been on studying the interactions in the same layer. In this context, Fan et al. have investigated four asymmetric split ring resonators based structure separated by a dielectric spacer in which the near field coupling between the resonators results in toroidal excitation in the microwave frequency range [57]. Further, they reported the enhancement of Q factor by optimizing the resonators [58]. Wang et. al [59] have demonstrated the excitation of toroidal resonances via two coplanar U shaped split ring resonators and reported red-shift in resonances with increasing inductance of the spacer. In spite of significant work on toroidal excitations,

---

Part of the results of this Chapter have been published in the following paper: Angana Bhattacharya, Rakesh Sarkar, and Gagan Kumar, "Excitation of near Field Coupled Dual Toroidal Resonances in a Bilayer Terahertz Metamaterial Configuration," Journal of Physics D: Applied Physics, 2021, 54(28), 285102 bilayer coupled toroidal resonator have not been given considerable attention at terahertz frequencies. This study discusses a bilayer coupled resonator system and develops a comprehensive understanding to control toroidal dipolar moments using terahertz MMs. The MM structure consists of a circular split ring resonator with symmetric gaps on both arms. It is further combined with another identical meta atom by separating the two layers using a polyimide spacer. Each resonator shows toroidal excitations in terahertz regime where the effect of interaction between the toroidal dipolar moments of each layer is analysed. The coupling between the two toroidal excitations is investigated by rotating the top resonator. Surface current profiles and magnetic field profiles of the MM structure are studied to understand the toroidal effect better. The Q factor of the single and double layer configurations are calculated to stress on the coupling effect. Further, a mathematical model is suggested to explain the coupling between the toroidal dipolar resonances. The chapter is organised as follows –the second section discusses the metamaterial geometry in detail and elaborates on the results obtained via numerical simulations. The coupling between the toroidal excitations and their switching from a coupled to an uncoupled system is studied via surface current and magnetic field profiles. A theoretical modeling of the coupling between the toroidal resonances is discussed which is followed by the conclusions.

3.1 Design of the coupled terahertz metasurface

To achieve a dual toroidal response and to demonstrate the coupling nature of the toroidal moments, we carefully designed our MM array. Each unit cell of our proposed MM structure consists of a circular split ring resonator (SRR) with two symmetric gaps respectively on both the arms of the SRR on a quartz substrate. On top of the first layer of metamaterial array, a polyimide layer is placed which acts as a dielectric spacer. The dielectric spacer of polyimide is further topped by a layer of identical circular split ring resonator. This results in a bilayer design capable of demonstrating required toroidal coupling between the excitations in the two layers. The schematic of our MM structure is shown in figure 3.1(a). In the proposed MM structure, the SRR is made of gold of thickness 200 nm while the substrate is made of loss free quartz of 200 μm thickness (h). The periodicity 'p 'along both the x and y axis is 44 μm. The parameters of the proposed SRR are shown in figure 3.1(b) by magnifying a single meta atom. The outer radius 'r_1'of the SRR is 15 μm and the inner radius 'r_2 'is 10 μm. The capacitive gap

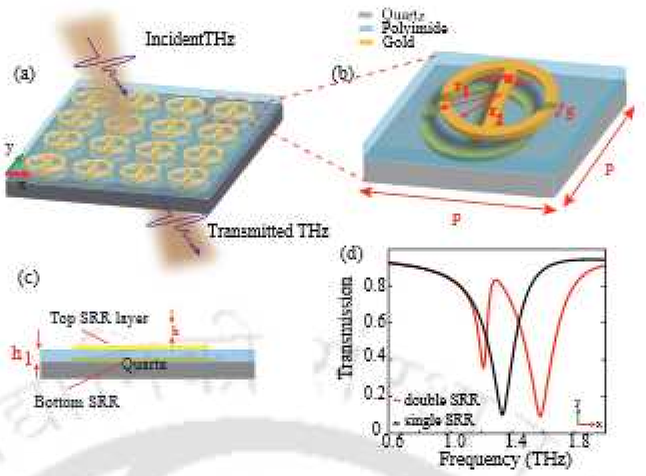

Figure 3.1: (a) Schematic of the proposed metamaterial bilayer configuration exhibiting dual toroidal dipolar resonance. The first layer consists of circular resonators made of gold on a quartz substrate. A polyimide layer covers the first layer on top of which a further identical layer of gold split ring resonators are added. Electric field of incident THz beam is polarised parallel to the split gap along y direction. (b) The unit cell consists of two layers of identical split ring resonators of periodicity 'p', width 'w', split gaps 'g', the inner radius 'r_2'and outer radius 'r_1'. When polyimide layer covers the first layer of resonators it is termed as 'single SRR'and when the second layer of resonators are added, the overall design is called as 'double SRR'. (c) Side view of the bilayer MM design. (d) The transmission spectra for 'single SRR'configuration showing single toroidal resonance dip at 1.34 THz and the transmission spectra for the 'double SRR'configuration showing dual toroidal resonances at 1.21 THz and 1.58 THz respectively.The green arrow indicates the direction of polarization of the incident THz beam.

'g'each arm of the circular resonator is 4 μm. The width of the middle arm is 5 μm. The polyimide spacer is of height (h_1) 4μm thickness. The geometry which consists of polyimide layer on top of the first layer of SRRs is termed as 'single SRR'. The final bilayer design, which comprises the second layer of SRRs on top of the polyimide spacer is termed as 'double SRR '. These layers are shown in figure 3.1(c) for clearity. Terahertz radiation with electric field polarised parallel to the split gap is incident on the MM array. Fig 3.1(d) shows the transmission spectra obtained from single SRR and double SRR configurations when THz radiation is incident on the MM array. All designs and numerical simulations are done in commercially available CST microwave studio using tetrahedral meshing in the frequency domain solver. Unit cell boundary conditions are set along x and y directions while we set open boundary conditions along the direction of light propagation for the metamaterial geometry. This geometry can be fabricated via a two-step lithography process.

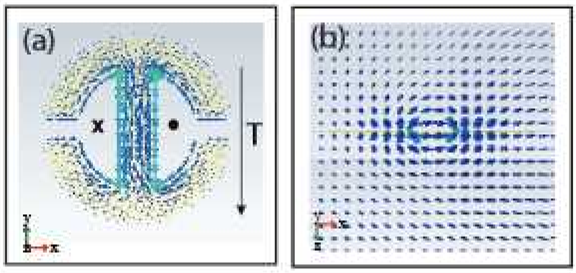

Figure 3.2: (a) Surface current profile of the single SRR layered with polyimide at 1.34 THz. The surface current on the right arm is along anticlockwise direction while on the left arm is along clockwise direction, leading to end to end formation of magnetic moment and a clear formation of toroidal dipole moment is observed. (b) End to end formation of magnetic moment indicating toroidal excitation.

3.2 Study of the metasurface response

The coupling of toroidal resonances in the bilayer MM array is investigated by studying the transmission profile of the MM geometry. The black line in figure 3.1 (d) shows the transmission obtained via numerical simulation when THz light is incident on single SRR configuration and a single resonance is observed at 1.34 THz. The red line shows the transmission spectra for double SRR configuration. On adding the second layer of meta-atoms, a low frequency resonance is observed at 1.21 THz and a second higher frequency resonance is observed at 1.58 THz respectively. It is expected that for an uncoupled system, the low frequency resonance, belonging to the bottom layer, would excite at the same resonant frequency as it's initial single layer configuration even on the addition of a second layer. However, for the bilayer configuration a red shift in the low frequency resonance is observed (shift from 1.34 THz to 1.21 THz) which indicates the strong near field coupling between the excitations in the bilayer configuration. The addition of polyimide layer results in the increase of the inductance L of the polyimide layer. Since the frequency of the resonances depend inversely on the inductance, a red shift in the low frequency resonance is observed on the introduction of the second layer in the bilayer configuration [59]. This is further validated in the modeling discussed in the next section.

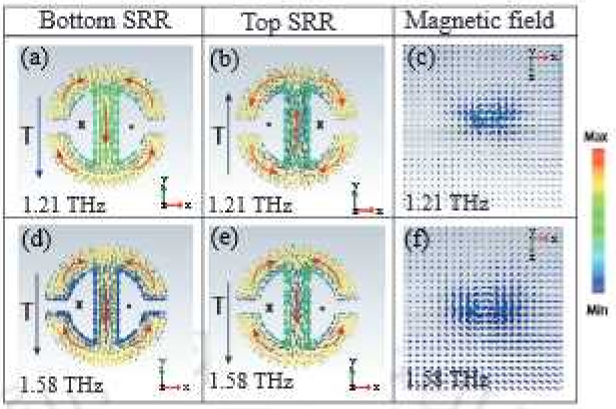

Figure 3.3: (a), (b) Surface current profile for bottom SRR and top SRR respectively for bilayer MM design at 1.21 THz. (d), (e) surface current profile for bottom and top SRR respectively for bilayer MM at 1.58 THz. The clockwise and anticlockwise current flow clearly depict toroidal dipolar excitation in the MM design. (c), (f) Magnetic field profile showing end to end magnetic moment formation leading to toroidal dipole excitation at frequencies 1.21 THz and 1.58 THz respectively.

3.3 Analysis of toroidal behaviour of the resonances

In order to confirm the toroidal behaviour of the resonances, the surface current profiles and magnetic field profiles are studied for each configuration. Figure 3.2 (a) displays the surface current profile for resonance observed at 1.34 THz of single SRR configuration. It is seen that the surface current in the right arm flows in the anticlockwise direction while that in the left arm flows in the clockwise direction. This leads to the formation of a magnetic moment coming out of the plane in the right side and magnetic moment going into the plane in the left side. This end to end formation of magnetic moments in turn leads to toroidal dipolar excitation along the negative y axis. Figure 3.2 (b) illustrates the magnetic field profile for the toroidal resonance at 1.34 THz showing end to end alignment of magnetic dipole moments and confirms the toroidal behaviour. Further, the surface current profiles and magnetic field profiles of double SRR configuration are simulated. The surface currents form a loop in the circular SRR resulting in end to end formation of magnetic dipole moments and hence an excitation of toroidal dipolar moments. From figure 3.3(a) it is seen that the surface current profiles orient the toroidal dipolar excitation along negative y axis for the bottom resonator while figure 3.3(b) shows that the toroidal excitation is along the positive y axis for the top layer of resonators corresponding to the resonance at 1.21 THz. For the resonance at 1.58 THz it is observed from figure 3.3(d) and 3.3(e) that the flow of currents along clockwise and anticlockwise

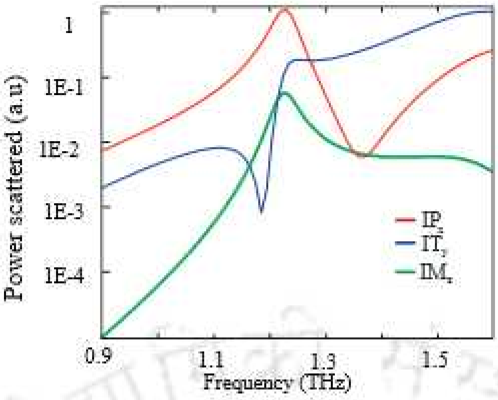

Figure 3.4: Multipolar analysis of the bilayer metamaterial depicting power radiated by the multipolar moments over the simulated frequency range. It is seen that at 1.58 THz power radiated by toroidal dipolar resonance dominates over that of electric and magnetic dipolar resonances. At 1.21 THz where toroidal dipolar resonances are aligned along opposite direction, power radiated by electric dipolar resonance dominates.

directions in the right and left resonators respectively result in the formation of toroidal dipolar excitations and these excitations are aligned along the negative y axis for both the top and bottom layer of resonators. The magnetic field profiles are also studied for both configurations, as shown in figure 3.3(c) and 3.3(f). The circulation of current results in formation of magnetic dipole moments. It is observed that the magnetic dipoles orient in a head to tail arrangement which is a signature for toroidal excitations. In an effort to numerically confirm the toroidal behaviour of the metamaterial design, we ran a multipolar analysis to study the power radiated by toroidal, magnetic and electric dipolar components using equation (1.2-1.5) as elaborated in Chapter 1, where IP_x, IT_y, and IM_z indicates the power radiated by electric, toroidal and magnetic dipoles respectively. Figure 3.4 represents the normalized power scattered over the simulated frequency range by the multipolar components. In the analysis, we have ignored higher multipoles for clarity. It is observed that at the lower frequency of 1.21 THz, the power radiated by the electric dipolar vector is higher than that of toroidal dipolar vector. This is believed to be due to the oppositely oriented toroidal dipolar resonances in the top and bottom layer at 1.21 THz, as apparent from the surface current profile shown in figure 3.3 (a ,b). Further, we observe that the radiated toroidal dipolar power dominates the electric and magnetic dipolar powers at 1.58 THz. In this case, toroidal dipolar resonances are oriented along the same direction (Fig. 3.3(d,e)) and therefore expected to dominate the other multipole moments.

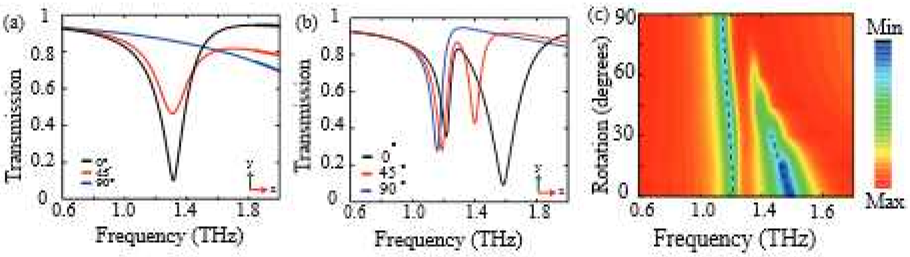

Figure 3.5: (a) Transmission spectra for 'single SRR' when top SRR is rotated by 45 degrees and 90 degrees with respect to the bottom SRR. The excitation diminishes at a fixed resonance frequency as rotation angle increases to 90 degrees. (b) The dual toroidal resonance seen for bilayer design ('double SRR') at the initial position of 0 degree. The high frequency resonance diminishes and vanishes at 90-degree rotation, leaving a single toroidal resonance corresponding to the bottom layer. (c) The contour plot shows the shift of resonances as the top SRR is rotated from 0 to 90 degrees and the final vanishing of higher frequency resonance for 90 degrees' rotation of top resonator.

3.4 Investigation of coupling and modulation of the toroidal excitations

Further, to study the coupling between the toroidal dipolar moments in the bilayer design, the quality factor (Q) is studied. The quality factor is a dimensionless parameter that is defined as the ratio of the energy stored to that of energy dissipated by the resonator, per cycle. A high Q factor indicates less damping or a low rate of loss of energy as compared to the energy stored. For our calculations, we have used the definition that Q factor is the ratio of the resonance frequency to the bandwidth at full width at half maximum (FWHM). Q factor for the 'single SRR'configuration at resonance frequency 1.34 THz was calculated and found equal to 7.17. Next, the Q factor for bilayer MM geometry was calculated and was found to be 17.7 for the resonance at 1.21 THz and 8.61 for the resonance at 1.58 THz. This increase in the Q factor at 1.21 THz indicates lower losses on adding the second layer of SRRs. We further examine the modulation of toroidal resonances in the coupled system by rotating the top SRRs from its initial position of 0 degree with respect to the SRR of the bottom layer (i.e. exactly aligned with the lower layer). It is rotated in the steps of 15 degree until it is at a 90-degree rotation with respect to the bottom SRR. Fig 3.5 shows the transmission spectra for the MM for different degrees of rotation. Figure 3.5(a) indicates that for the bottom layer corresponding to 'single SRR1', the rotation of the top resonator would result in diminishing of the resonances and finally vanishing of the resonance on rotation by 90

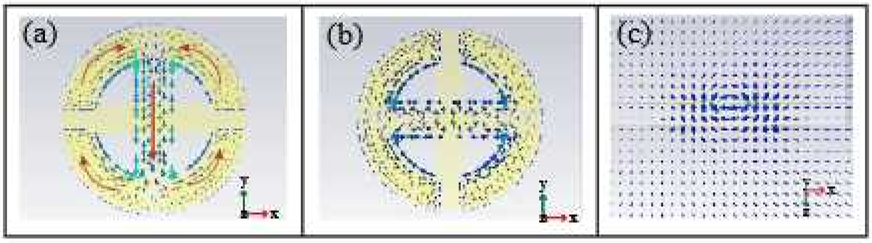

Figure 3.6: (a) Surface current for bottom resonator, showing toroidal behaviour when top SRR is rotated by 90 degrees at 1.145 THz. (b) Surface current profile for top SRR when it is rotated by 90 degree with respect to bottom SRR. Current profile shows no clockwise anticlockwise nature and toroidal dipolar moment is not observed. (c)Top view of magnetic field profile showing toroidal dipole excitation in bottom SRR and no toroidal excitation in top SRR.[117]

degree at a fixed resonant frequency. However, for bilayer configuration as demonstrated in figure 3.5(b), the resonances depict a red shift. The black line in figure 3.5(b) is the plot for when both the layers are exactly aligned. The red line shows transmission for the top layer of SRRs rotated by 45 degree with respect to the bottom layer. The blue line indicates the transmission plot when the top layer is at a 90-degree rotation with respect to the bottom layer. It is observed from figure 3.5 that the dual toroidal resonance is pronounced at zero degree because of the coupling between the bilayer configurations and reduces as it is rotated by 45 degree. The high frequency resonance tunes out and as rotation angle increases from 75 degree to 90 degree, the resonance vanishes and only the low frequency resonance is observed. Thus a single resonance is visible at 1.15 THz corresponding to the lower layer in the bilayer MM. This indicates the switching of toroidal excitations in a coupled bilayer metamaterial system via rotation. The contour plot, shown in figure 3.5(c) presents a comprehensive picture of the modulation and switching of the resonances. We also investigate the surface current profile for this configuration of 90 degree rotated top layer of SRRs. From figure 3.6(a) it is observed that the bottom circular SRR shows a toroidal behaviour because of the clockwise and anticlockwise circulating currents. However, the surface current profile of the top layer doesn't demonstrate the behaviour of toroidal dipolar excitations as observed from figure 3.6(b). The magnetic field profile in figure 3.6(c) also confirms this and indicates the end to end formation of magnetic moments only for the bottom resonator in the bilayer configuration.

3.5 Modeling of Toroidal Dipolar coupling

The single SRR exhibits a toroidal resonance at 1.56 THz in the absence of the polyamide layer, which we take as the intrinsic resonance frequency of the toroidal resonator written as $f_o = 1.56$ THZ. In the coupled structure, two distinct resonances are observed. For the interpretation of the interactions leading to the dual resonances, we have developed a theoretical modeling based on the Lagrangian approach. We have considered the coupled SRR pairs as two coupled LC circuits . One can write the Lagrangian of the coupled system as [61,62].

$$\begin{aligned}\Gamma = \frac{1}{2}L_1(\dot{Q_1}^2 + \dot{Q_2}^2) - \frac{1}{2}L_1 f_o^2(Q_1^2 + Q_2^2) + \\ \frac{1}{2}L_2(\dot{Q}_1 - \dot{Q}_2)^2 - M_H\dot{Q}_1\dot{Q}_2 - M_E f_o^2 Q_1 Q_2\end{aligned} \tag{3.1}$$

Here, L_1 represents the inductance of the resonators, L_2 is the additional inductance which contributes to the electrical coupling, and M_H and M_E are the coefficients of the magnetic and electric dipole-dipole couplings. The first two terms represent kinetic energy from inductances and potential energy from the capacitors of the coupled system. The current exchange between the two resonators contributes to the kinetic energy represented by the third term. The fourth and fifth terms signifies the potential energy arising due to magnetic and electric dipole-dipole interactions of the two coupled resonators. In order to obtain the Eigen frequencies, we have used Euler-Lagrange's equation of motion

$$\frac{d}{dt}\left(\frac{\delta\Gamma}{\delta\dot{Q}_i}\right) - \frac{\delta\Gamma}{\delta Q_i} \tag{3.2}$$

(where i= 1,2). Substituting equation (2) in Euler-Lagrange's equation (3), we obtain the Eigen frequencies of the coupled toroidal resonances as,

$$f_1 = f_o\sqrt{\frac{1-K_E}{1+2\eta+K_H}}, \tag{3.3}$$

with Q_1 = -Q_2

$$f_2 = f_o\sqrt{\frac{1+K_E}{1-K_H}} \tag{3.4}$$

with $Q_1 = Q_2$
, where ($K_E = \frac{M_E}{L_1}$), ($K_H = \frac{M_H}{L_2}$), ($\eta = \frac{L_2}{L_1}$) are normalized coupling coefficients and we have taken the trial solution as ($Q_i = A_i e^{i\omega t}$). From the numerically simulated transmission

spectrum of Figure 5, we have calculated the fitting parameters and are depicted in table 1. From table 3.1, one can note that the coefficient of inductive coupling is always positive and that of the conductive coupling is always negative. The higher value of M_H signifies that the inductive coupling plays a major role in our coupled bilayer structure. For $\theta = 0$ degree, higher values of M_H and M_E signify that both the resonators are strongly coupled and two distinct toroidal resonances are observed at 1.21 THz and 1.58 THz respectively. As the orientation of top resonator w.r.t. bottom resonator changes i.e. θ varies from 0 degree to 90 degree M_H decreases from 0.626 to 0.56 and M_E decreases from -0.62 to -0.75. This reduction of coupling coefficients leads to the redshift of both the resonances. Thus the rotation of top SRR with respect to the bottom SRR reduces the strength of both conductive and inductive coupling. One can also note that as θ increases L_1 decreases and L_2 increases. Ultimately for θ=90 degree, for the given set of parameters, the value of K_E becomes equal to -1 and the resonance condition of ω_2 can not be satisfied. As a result, higher order resonance vanishes and also the lower values of M_H and M_E signify that the two resonators are least coupled. Hence the role of different coupling terms and their manifestation with respect to variation of orientation in our coupled structure can be estimated using Lagrangian approach

Table 3.1: Parameters for theoretical modeling of the modulation of dual toroidal excitations for different angles of rotation of top SRR with respect to bottom SRR in bilayer configuration

θ (degree)	L_1 (pH)	L_2 (pH)	M_E (pH)	M_H (pH)	ω_1 (THz)	ω_2 (THz)
0	0.86	0.48	-0.62	0.626	1.21	1.58
45	0.84	0.55	-0.64	0.592	1.19	1.40
90	0.75	0.72	-0.75	0.56	1.153	0

3.6 Discussion

This chapter provides a numerical and analytical understanding on the coupling of toroidal resonances, and the switching of the coupled toroidal system to an uncoupled system. The bilayer configuration comprising of two layers of SRRs seperated by a polyimide layer demonstrated dual toroidal dipolar excitation. The surface current and magnetic field profiles, and a multipole analysis of power scattered by different electromagnetic moments confirmed the toroidal behaviour. The modulation from dual to single toroidal excitations is observed when the higher order toroidal excitation gradually diminishes and vanishes when the top resonator is rotated by 90 degree, indicating a modulation of the toroidal resonances in the bilayer system. To expand our understanding of bilayer coupling of toroidal dipolar excitations, a theoretical model is explained using the Lagrangian approach. The study of coupled dual toroidal resonances in bilayer configurations can be useful in the design of devices demonstrating enhanced coupling and high Q factors.

CHAPTER 4

TUNABLE TOROIDAL EXCITATION IN GRAPHENE TERAHERTZ METASURFACE

The study of the toroidal excitation in metasurfaces and its applications is quite a major step in the development of toroidal meta-photonic devices. The previous chapter discussed the excitation and interaction of toroidal excitations in a bilayer metamaterial and the passive modulation of the coupled toroidal system to an uncoupled system. In the terahertz regime, toroidal meta-modulators find special significance with high efficiency and tunability which has potential in communication and filtering applications [63,64]. In spite of these advantages, most of the studies on toroidal MMs have been focused only on the passive tuning of the toroidal responses. The active tuning of the toroidal response increases is possibility of use where one requires several applications that provides a control over the response of the metasurface in a desirable manner. In this context, recently, active tuning of MM structures using graphene has garnered a lot of attention [67-72] due to graphene's capability in actively tuning of resonances through application of external biased voltage. However, only a limited work has been done on the active tuning of toroidal resonance in graphene metasurfaces [70,73,74]. The active tuning of the toroidal responses using graphene-based MMs can be of immense significance in sensing and other applications. In this chapter, an attempt is made to address the problem of

---

Part of the results of this Chapter have been published in the following paper: Bhattacharya, A., Devi, K. M., Nguyen, T. and Kumar, G. Actively tunable toroidal excitations in graphene based terahertz metamaterials. Opt. Commun. 459, 124919 (2020) active tuning of toroidal excitation. The excitation of toroidal dipolar excitations in a planar 2D MM structure comprising an array of two joint resonators (SRRs) made of graphene with two split gaps in each resonator is discussed. The active tuning and modulation of the MM's toroidal response is examined by varying the Fermi energy and relaxation time of the graphene material. The surface current and magnetic field profiles of the MM structure is studied to understand the toroidal effect. The subsequent sections discuss the design of the graphene based planar metamaterial geometry, the toroidal excitation at terahertz frequency and its active tuning in detials.

4.1 Design of graphene based terahertz metamaterial

The excitation of toroidal resonances in metamaterials require an optimized design of the meta-molecule unit cell. Each unit cell of our proposed MM structure consists of two split ring resonators, each having two gaps, which have been joined together to form a single resonator. The schematic of the proposed metamaterial array along with the transmission characteristics is illustrated in figure 4.1(a) . In the proposed structure, the split ring resonators are made of graphene material while the substrate is made of intrinsic silicon having a thickness of 10 μm. The periodicity of the structure in x and y direction is taken as $p_x = 24$ μm , $p_y = 12$ μm while the length and breadth of a single resonator is taken as $l = 18$ μm , $b = 8$ μm , respectively. The width 'w' of each strip of resonator is 1 μm and the capacitive gap 'g' of each resonator is considered as 1 μm. The distance of the central position of each gap from their respective side arms is fixed at 4.5 μm. The numerical simulations are performed using the technique of finite element frequency domain solver in CST Microwave Studio. The metamaterial geometry is simulated under the unit cell boundary conditions in the x–y plane. One may fabricate proposed graphene structures on a silicon carbide (SiC) substrate by first growing graphene using chemical vapour deposition (CVD), and then printing and lithography followed by appropriate post processing techniques.

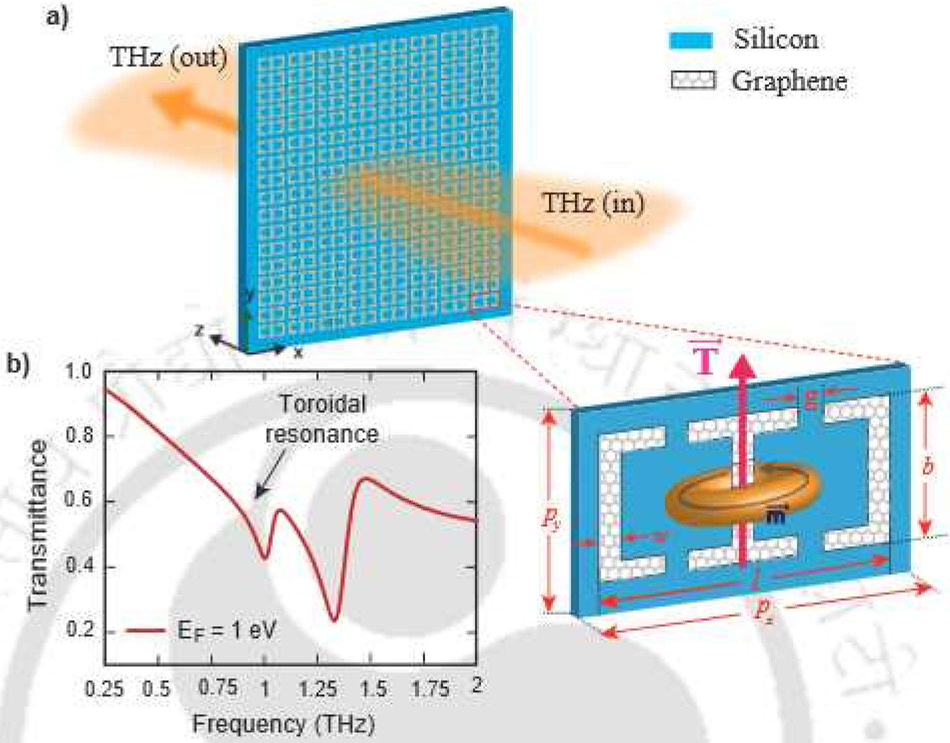

Figure 4.1: (a) Schematic of the proposed terahertz metamaterial structure resulting in toroidal excitation. Silicon substrate is shown in blue color, whereas graphene split rings are shown with gray color. The inset shows a larger view of the metamaterial unit. The unit cell consists of two split ring resonators, each having two gaps, which have been joined together to form a single resonator. p_x and p_y represent periodicities of the unit cell in the x and y directions, respectively. l and b stands for length and breadth the unit cell. Width and split gap of the resonator is represented by w and g. The configuration allows us to excite toroidal resonance in the y-direction, shown by T. (b) Transmittance versus frequency plot of the MM structure resulting in toroidal excitation for E_F=1 eV of graphene.

4.2 Analysis of the metasurface's response and toroidal behaviour

Figure 4.1(b) shows a plot of the transmittance profile of the MM structure at normal incidence versus frequency for the Fermi energy E_F= **1 eV** of the graphene layer. It is evident from the figure that two dips are observed in the transmittance profile, where the first dip occurs at frequency 0.98 THz and the second at 1.33 THz. In the transmittance profile, the first dip at frequency 0.98 THz indicates a toroidal excitation, whereas second dip correspond to dipolar resonance. This chapter focusses only on toroidal excitation.

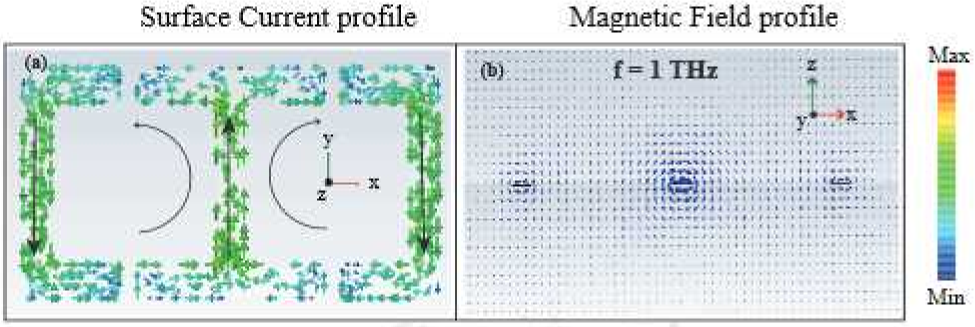

Figure 4.2: (a) Surface current profile in the graphene metamolecule structure having $E_F = 1$ eV. The current flows in clockwise direction in the right half of the resonator, whereas it flows in the anti-clockwise direction in the left half as indicated by black arrows. The current directions result in the formation of end to end magnetic dipoles, thus leading to a toroidal response (b) Magnetic field profile at $f = 1$ THz in the xz plane of the metamaterial unit cell structure indicating toroidal behaviour due to oppositely circulating currents.

In order to confirm the toroidal behavior of the resonance, we examined surface current profile and magnetic field profile of the MM structure in figure 4.2(a) and figure 4.2(b) respectively. It is apparent from 4.2(a) that the flow of current in the two resonators are in the opposite directions i.e. it flows clock-wise in the right hand side split ring resonator while it flows anti-clock wise in the left hand side resonator. This results in magnetic moment formation, going into the plane and out of the plane in the right and left resonators respectively. End to end formation of magnetic moment indicates toroidal excitation.The magnetic moments formed as a result of the ring like arrangement of our proposed meta-material structure helps in strengthening of the toroidal moments . Figure 4.2(b) shows the magnetic field profile in the xz plane of the MM structure. The circular magnetic field is more prominent in the central arm, as for this configuration, there happens to be more current flowing through the central arm than the other two arms. This leads to the development of toroidal moment in the MM structure.

4.3 Active control and modulation of toroidal resonances

Graphene has an important advantage that it's Fermi level can be manipulated by the application of a gate voltage,chemical doping or by photo induced doping. Graphene integrated MM structures could be advantageous in making active devices as it's Fermi energy can be tuned.[67,75,76]. To explore the active tuning capability of toroidal reso-

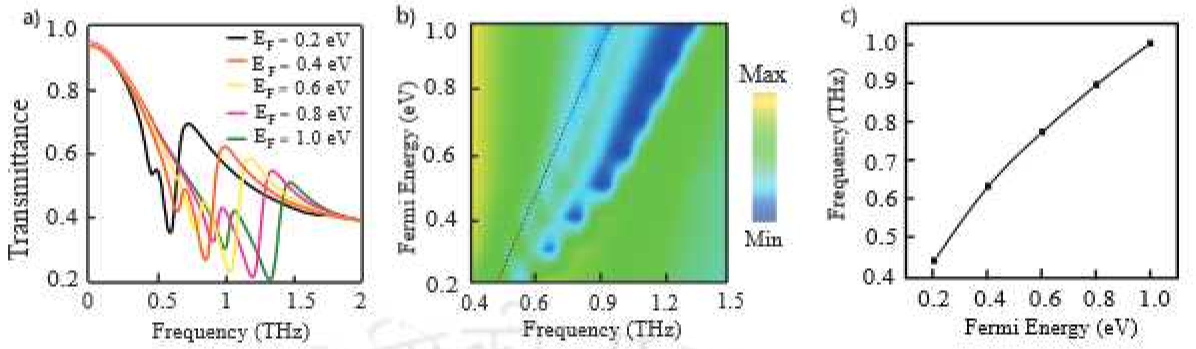

Figure 4.3: (a) Transmittance versus frequency for increasing values of Fermi energy from 0.2 eV (in black) to 1 eV (in green). There is an evident blue shift in the toroidal resonance on increasing Fermi energy. (b) Colour and contour plot for Fermi energy versus frequency indicating a shift in the toroidal resonance. (c) Variation of toroidal frequency versus Fermi energy of graphene layer for $\tau = 2\ ps$. The frequency increases with Ferimi energy as $\omega \propto {E_F}^{\frac{1}{2}}$.

nances in the proposed MM structure, we perform numerical simulations for different Fermi energy E_F. The transmittance characteristics of the proposed MM structure are examined by varying E_F from 0.2 eV to 1 eV for a fixed relaxation time. These chosen values of Fermi energies have been experimentally reported in previous works [53,54,37]. The transmittance profile along with its corresponding contour plot is depicted in Fig 4.3. Figure 4.3(a) represents the line plot of the transmission characteristics of the proposed MM structure. The first dip in the figure indicates the toroidal excitation. The black solid line depicts transmittance for Fermi energy 0.2 eV while the orange line shows transmittance for Fermi energy 0.4 eV. The transmittance for Fermi energy 0.6 eV is represented by the yellow solid line. The pink trace signify the transmittance for E_F = 0.8 eV and the green line corresponds to Fermi energy 1 eV. It is evident from the figure that there is significant shift in the toroidal resonance as the Fermi energy is increased. This can be further understood from the contour plot shown in figure 4.3(b). It is clearly observed from the contour plot, that the frequency of the toroidal resonance exhibits a blue shift with the increase of the value of Fermi energy of the graphene layer as depicted by the dotted line. The blue shift in the resonance with increasing Fermi Energy can be explained using the formula for carrier concentration,

$$n = \frac{1}{\pi}(\frac{E_F}{\hbar v_F})^2 \tag{4.1}$$

As mentioned in [75], the universal relation between ω and $|E_F|$ is described by a scaling of $\omega \propto {E_F}^{\frac{1}{2}} \propto n^{\frac{1}{4}}$ where ω is the frequency, E_F the Fermi energy and n is the carrier concentration. On taking a square root of the Fermi energy variation from 0.2 eV

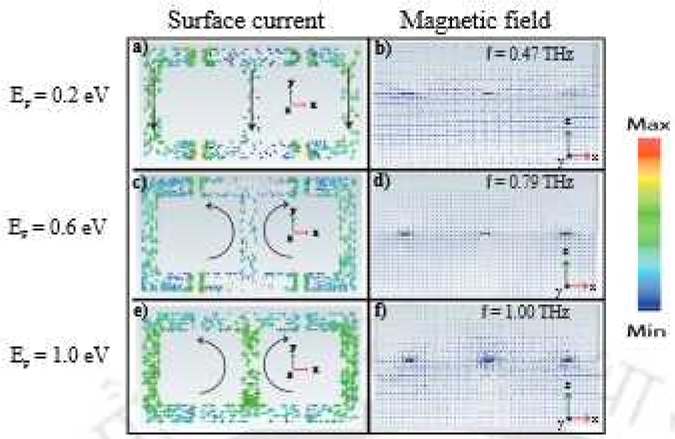

Figure 4.4: : Surface current and magnetic field profiles for symmetric metamaterial structure with increasing visibility of toroidal resonance with increase of Fermi energy. a), c) and e) represent surface current profiles corresponding to Fermi energies 0.2 eV, 0.6 eV and 1.0 eV respectively, while b), d) and f) represent respective magnetic field profiles. Oppositely flowing currents in the arms for Fermi 0.6 eV and 1.0 eV at fixed phase angle leads to toroidal response.

to 1 eV, using the above mentioned formula, it is observed that the shift in frequency of the toroidal resonance with an increase in Fermi energy is well accounted. This is depicted in figure 3 (c). The formula for equation (1) fits well for the toroidal resonance frequency with Fermi energy, as can be seen in figure 4.3(c) and therefore, it is believed that the toroidal excitations originate from graphene plasmons. To further understand the effects of the variation of Fermi energy on the toroidal response of MM structure, the surface current and the magnetic field profile is examined. Figure 4.4 represents the magnetic field profile along with the corresponding surface current profile for E_F= 0.2 eV, 0.6 eV and 1 eV for a fixed phase of 153.75 degree. Figure 4.4(a) and (b) represents the surface current and the magnetic field profile for E_F = 0.2 eV. It is evident from figures 4.4(a), and (b), that there is almost no toroidal resonance. As the Fermi energy is increased, a visible formation of toroidal excitation is observed. When the flow of current in the two resonators are in the opposite direction such that it flows clock-wise in the one resonator while it flows anti-clock wise in the other resonator, it gives rise to two magnetic monopoles joining end to end and hence a toroidal excitation is obtained. In the right resonator a magnetic dipole forms pointing out of the plane while in the left resonator, the dipole points into the plane. Figure 4.4(c) depicts oppositely flowing currents in the two resonators while a visible formation of toroidal excitation can be seen from Fig. 4.4(d). For Fermi energy 1 eV, it is observed from figures 4.4(e) and (f)

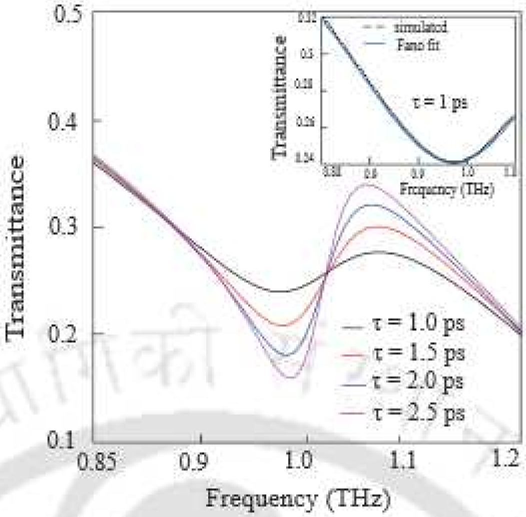

Figure 4.5: Transmittance versus terahertz frequency for toroidal resonance for different values of relaxation times (τ = 1 ps, 1.5 ps, 2 ps, 2.5 ps). The amplitude of toroidal excitation can be modulated with τ. Inset depicts the Fano fitting of the simulated data τ = 1 ps. The dotted curve corresponds to simulation, whereas blue curve represent fitting.

that a uniform distribution of oppositely flowing currents occurs in the resonators. This oppositely flowing currents, in turn, leads to the formation of strong toroidal excitation in the MM structure. Therefore, it can be concluded that an effective active tuning of the toroidal resonance can be achieved by varying the Fermi energy of the graphene layer. Thus,as can be seen from the variation of Fermi energy in figure 4.3, the resonanace dips become more prominent on increasing Fermi energy from 0.2 eV to 1 eV. These particular values have been so chosen as they are conventionally experimentally viable, as mentioned before. This tuning in toroidal resonance on increasing fermi energy is confirmed by the surface current and magnetic field profile plot in figure 4.4. We further examine the effect of change of relaxation time in graphene material on the toroidal excitations. Experimentally viable relaxation times as reported in previous works have been chosen [77,78]. Terahertz transmittance results for toroidal resonances versus frequency for different relaxation times are shown in figure 4.5. As the relaxation time (τ) is changed, we observe an amplitude modulation of the toroidal response. In figure 4.5(a), the black line depicts the transmittance for relaxation time τ = 1 ps. The red line depicts toroidal excitation for relaxation time τ = 1.5 ps, the blue line stands for τ = 2 ps while the pink line depicts transmission for τ = 2.5 ps.For the change in relaxation time from 1 ps to 2.5 ps, it is observed that the amplitude of the transmittance dip increases. As can be seen from the figure, significant change in amplitude of the transmittance

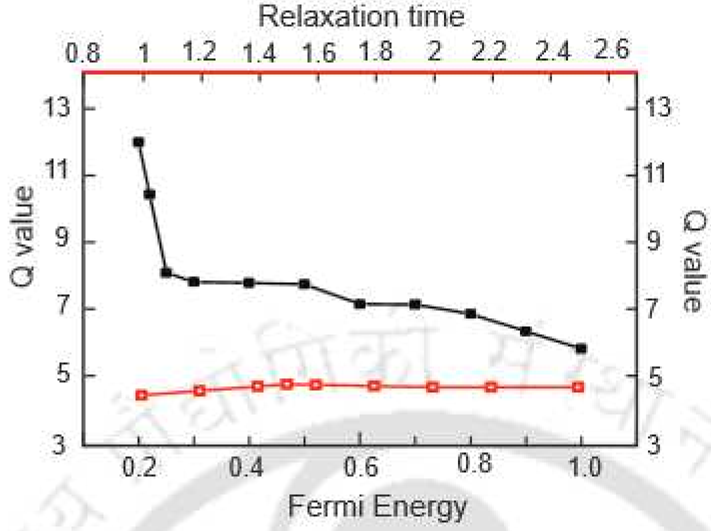

Figure 4.6: Variation of Q value with a change in relaxation time and Fermi energy. The red curve corresponds to the variation of Q-factor with relaxation time (upper x-axis), which remains nearly constant signifiying almost no change. The black curve represents the change of Q-value versus Fermi energy for $\tau = 1\ ps$. Q value decreases with an increase of Fermi Energy.

curve is observed on changing the relaxation time. The inset of the figure depicts the fitting of the toroidal resonance for 1 ps relaxation time with a Fano line shape function (given by Eqn.(3)). This is done to evaluate the Q factor of the resonance as has been described in the next section. The increase in transmittance dip can be understood by the dependence of conductivity on the relaxation time. According to Drude model, the conductivity of a material can be defined as $\sigma = ne^2 {v_F}^2 \tau / E_F$, where τ is relaxation time, E_F is Fermi Energy, and v_F is Fermi velocity. An increase in τ leads to an increase in σ. The imaginary part of the complex wave number k, is given by [79],

$$k \equiv \omega \sqrt{\frac{\epsilon\mu}{2}} \left(\left[\sqrt{1 + \left(\frac{\sigma}{\epsilon\omega}\right)^2} - 1 \right] \right)^{\frac{1}{2}} \tag{4.2}$$

This implies an increase in wavenumber with an increase in σ, which results in a reduced transmittance since it varies as $e^{-\alpha r}$, where α is an absorption coefficient $(= 2k)$. Therefore, increase in relaxation time leads to a decrease in the amplitude of transmittance dip. A similar explanation is valid for the increase in transmittance dip amplitude for increasing Fermi energy. Since $v_F \propto E_F$, this implies σ becomes proportional to Fermi Energy. As fermi energy increases, σ increases, from Eq.4.(1) and it is seen that k increases as well. This leads to a decrease in the transmittance and decreasing of amplitude of the transmittance dips for Fermi energy can be explained.

4.4 Quality factor calculation

In order to appreciate the relevance of the toroidal excitations, we further calculate Q-factor of the resonances. The Quality factor (Q) is a dimensionless parameter which is used to quantify the resonator's energy storage with respect to the energy loss. A high Q factor signifies less damping , i.e, low rate of loss of energy as compared to the energy stored. From the transmittance plots obtained for both fermi energy and relaxation time, the toroidal resonance is fitted with a fitting formula for assymetric resonances. We calculate the Q-factor of the modes using the procedure discussed below. A number of studies have reported a fitting formula to fit the fano asymmetric resonance [80,81].To further ensure that the toroidal resonance obtained shows fano characteristics, the transmittance for varying relaxation time is fitted with the lineshape fitting formula

$$T = |a_1 + ia_2 + \frac{b}{(\omega - \omega_0 + i\gamma)}|^2 \tag{4.3}$$

where a_1, a_2 and b are constants, ω_0 is the resonant frequency and γ is the overall damping rate.The Q value is defined as $\frac{\omega_0}{2\gamma}$. The Q factor of the dipole resonance for Fermi energy 1 eV is calculated and found to be 8.82. A decrease in the Q value is observed on increasing the Fermi Energy from 0.2 eV to 1 eV. This decrease in Q factor can be attributed to the change in carrier concentration with an increase in Fermi energy [82]. As expected the Q-factor decreases sharply in the beginning and then slowly for large value of E_F. However,it is observed that a change in the relaxation time results in the Q value showing very slight change and can be taken to be constant. The Q factor obtained for variation in Fermi energy as well as relaxation time is shown in figure 6. The red line plot for right hand y axis and upper x axis stands for the Q factor variation with relaxation time. The black line plot for left hand Y axis and lower X axis stands for the Q factor variation on increase of Fermi energy. An increase in Fermi energy results in a decrease in the Q factor. It is observed that a change of relaxation time does not show much effect on the quality factor. The Q factor remains constant. This fact can find use in high Q factor geometries where modulation can be achieved without changing Q values.

4.5 Discussion

In this chapter a graphene based planar metamaterial geometry capable of supporting toroidal excitations, has been discussed. In the MM structure, the actively tunable response is obtained by changing the Fermi energy of graphene layer. It is observed that an increase in Fermi energy from 0.2 eV to 1 eV results in prominent toroidal excitations. It also causes a blue shift of the toroidal resonance in the MM structure. This blue shift in the resonance scales with Fermi energy and number density n as $\omega \propto {E_F}^{\frac{1}{2}} \propto n^{\frac{1}{4}}$. The magnetic field and surface current profiles indicate the excitation of toroidal resonances. Further, we observed that change in relaxation time of graphene layer leads to amplitude modulation of the toroidal response. An increase in the relaxation time from 1 picosecond to 2.5 picosecond increases the amplitude of toroidal resonance of the MM structure. We have also analyzed the Q-factor of the toroidal resonances by fitting them with the Fano linshape formula. It is observed that an increase in Fermi energy leads to a decrease in the Q value of the toroidal resonance. Further, a change in relaxation time has almost null effect on the Q value. This fact can be used in constructing terahertz devices where signal can be modulated without affecting the quality factor. Such active tuning of MM using graphene and excitation of toroidal resonances at terahertz frequencies and their dynamic control could be significant in designing tunable terahertz devices.

CHAPTER 5

ELECTROMAGNETICALLY INDUCED TRANSPARENCY IN A TOROIDAL TERAHERTZ METASURFACE

The previous chapters discussed the excitation of toroidal resonances in terahertz metasurfaces along with the possibility in its passive and active modulation. In this chapter, we discuss an application of the toroidal dipole moment in inducing electromagnetically induced transparency (EIT) at terahertz frequencies. The EIT effect in metasurfaces has been briefly discusses in section 1.6.1 of this thesis. The potential of the toroidal excitation induced EIT in the THz spectrum can be immense. It has been observed that the coupling between toroidal and dipolar (electric and magnetic) resonances can result in narrow transparency windows with high Q factor resonances as compared to the dipole-dipole coupled system. This can find applications in the highly sensitive chemical and bio-molecular sensing [86]. Toroidal EIT also exhibit steeper dispersion within the transparency window resulting in an elevated group refractive index which can cause the group velocity of light to reduce significantly in the medium which can be useful in making optical components. Most studied on toroidal EIT has focussed on exciting a single EIT window in the microwave or GHz regime. In this context, Li et al. demonstrated EIT effect in a planar MM in the microwave frequency regime comprising

---

Part of the results of this section have been published in the following papers: Bhattacharya, A. et al. Multiband transparency effect induced by toroidal excitation in a strongly coupled planar terahertz metamaterial. Sci. Rep. 11, 1–9 (2021) and Bhattacharya, A., Sarkar, R. and Kumar, G. Toroidal electromagnetically induced transparency based meta-surfaces and its applications. iScience 25, (2022) of a toroidal asymmetric SRR acting as a dark mode resonator and cut wires acting as bright modes [87]. Similar work has been reported in literature where single EIT window is observed in the GHz range and multipolar analysis indicates prominence of toroidal excitations for the dark mode resonator [88,89]. Shen et al. observed EIT via combination of an asymmetric elliptical SRR and cut wires [88]. The combination resulted in an EIT window in the GHz range and the combined structure demonstrated toroidal behaviour [90]. Dynamic manipulation of EIT effect has also been reported in a graphene loaded all dielectric meta surfaces [91]. In another study, Shen et al. demonstrated dual band EIT effect in E-ϵ planar MM structure in microwave frequency regime. In the terahertz (THz) frequency domain, Wang et al. have explored the excitation of single EIT window where mutual coupling of two asymmetric 'J' shaped metal rings was observed [92]. Despite the growing interest, there has been a gap in examining dual band and multiband transparency effect induced by toroidal dipolar excitations in the THz region. Toroidal excitations strongly coupled with the dipolar resonances of the metamaterials can result in transparency windows that can be manipulated with coupling between the resonators. In this chapter, the single band transparency effect by coupling between a toroidal resonator and 'C' shaped resonators is examined in the THz frequency regime, which is followed by a thorough analysis of exciting dual band EIT using the toroidal THz metasurface. A theoretical modeling for toroidal resonance based EIT phenomenon is also explored and reported.

The chapter is organized as follows. The first section explores the excitation of single band EIT in the toroidal THz MM. The following sections discuss the excitation of multiband toroidal EIT. A theoretical model is elaborated in the last section to explain the EIT effect

5.1 Single band EIT in a toroidal THz metasurface

The excitation of a single band EIT is first analyzed via a carefully designed THz MM geometry. We designed a MM geometry which demonstrated coupling between bright toroidal-bright LC mode, resulting in a single band EIT window in the THz region. The MM configuration consisted of a double capacitive-gapped toroidal SRR and a C shaped dipolar resonator. This is illustrated in Figure 5.1. Figure 5.1(a) shows the designed MM array on which THz radiation is incident. The transmission profile of the MM array is shown in Figure 5.1(b). It is observed that in between the dips corresponding to 0.97

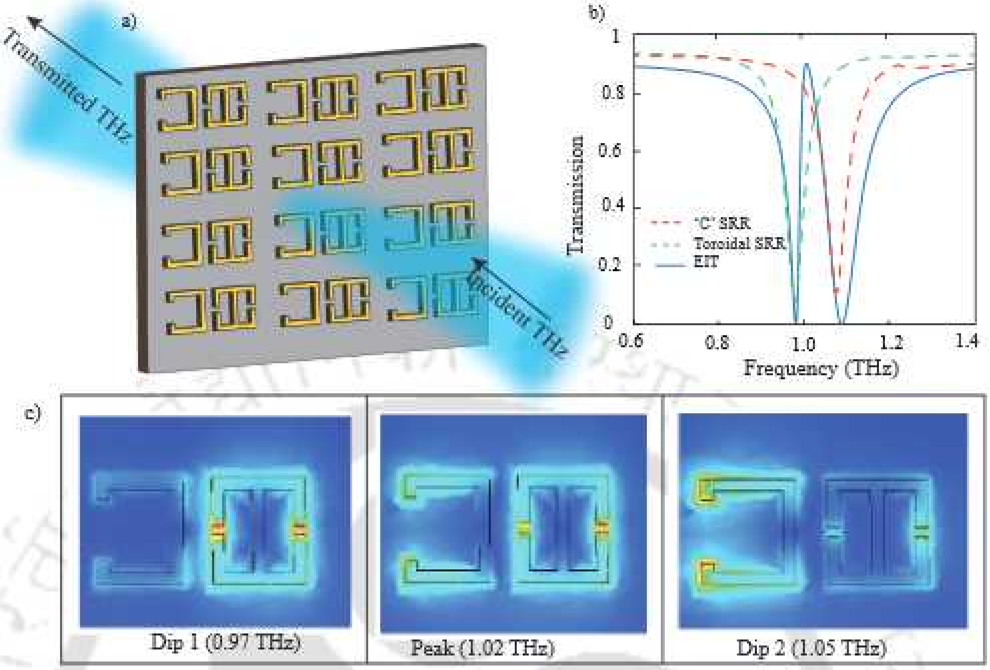

Dip 1 (0.97 THz)

Peak (1.02 THz)

Dip 2 (1.05 THz)

Figure 5.1: (a) Schematic of the proposed terahertz metamaterial structure resulting in single band toroidal EIT excitation.(b) Transmission through the individual resonators and the EIT response in the combined metasurface configuration. (c) Electric field profile of the metasurface at the excitation of EIT.

THz (dip 1), and 1.05 THz (dip 2), a transparency window is evident with a peak at 1.02 THz. The CST simulations of the transmission profile for the double gapped resonator and the C resonator showed individual resonance frequencies at 0.976 THz and 1.05 THz, respectively. These are depicted by the dotted lines in figure 5.1 (b). The green dotted line depicts the transmission for the double-gapped SRR, termed as "toroidal SRR", showing a resonance at 0.97 THz. The red dotted line depicts the tranmission through the C-shaped resonator, which demonstrates a resonance at 1.05 THz. The electric field profiles in Figure 5.1 (c) further validate this. It shows the excitation of the toroidal SRR at 0.97 THz, the excitation of the left CSRR at 1.05 THz, and at the peak frequency, both the resonators are excited. The excitation of both resonators at the transparency peak frequency in bright-bright mode coupling based EIT has been reported in literature (Yahiaoui et al., 2018). Hence, we demonstrated a single EIT window in the THz range via the bright-bright coupling of toroidal resonance to an LC resonance. Although single band EIT has found prominence in literature, recently the potential of EIT in multiband frequency regime has been paid significant attention by the research community. The advantage of multiband EIT over the single band EIT lies in the fact that one can manipulate the light-matter interaction over multiple windows in the frequency spectrum. Such investigations provide the flexibility in designing multiband sensors, modulators, and optical switch devices.

5.2 Dual-band EIT in a toroidal THz metasurface

5.2.1 Design of the terahertz metasurface and its terahertz response

To achieve dual-band transparency windows with toroidal resonance, the MM unit cell was carefully designed. The schematic of the MM configuration along with the unit cell are depicted in Figure 5.2. The geometry consists of a split ring resonator with symmetric gaps on each arm flanked by two C shaped resonators on each side. The split ring resonators are made up of aluminium. The MM resonators are designed on a quartz substrate having relative permittivity of ϵ_r = 3.75. The periodicity in the x direction is given by P_x =130 μm, that in the y direction is given by P_y = 80 μm. The parameters of the unit cell are magnified in the corresponding image of figure 5.2(b). The length 'L'of the mid resonator is 32 μm, and that of C shaped resonators, 'L_1'='L_2'= 30 μm. The breadth of each resonator 'b 'is taken as 35 μm . The capacitive gap 'g'= 'g_1'is 3 μm for the mid resonator and right 'C 'resonators while the capacitive gap of the left most C shaped resonator is 'g_2 '= 21 μm. 'd'depicts the distance of each C shaped resonator from the mid resonator. The width of the SRRs is given by 'w '= 4 μm. Figure 5.2 (c) shows the transmission plot when both the C shaped resonators are symmetrically placed from the mid resonator by d = 10 μm. Terahertz radiation is incident on the MM configuration with electric field polarised parallel to the split gaps along the y-direction. CST microwave studio software, version 2020 (`http://cst.com`), was used for the design and numerical simulations. We used tetrahedral meshing in the frequency domain solver. Periodic boundary conditions were set along x and y direction while open boundary condition is used along the direction of incident light. The geometry can be fabricated via conventional photo-lithography or electron beam lithography in a clean room environment. The transmission for the proposed MM was studied numerically for incident terahertz beam. The transmission spectrum obtained for the configuration with d=10 μm is plotted in figure 5.2(c). Three resonance dips and two transparency

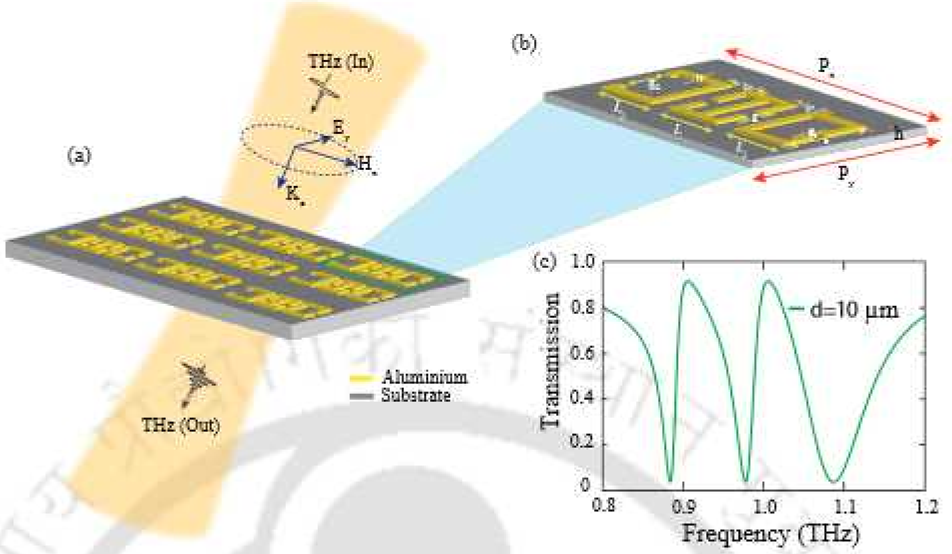

Figure 5.2: (a) Schematic depicting the terahertz transmission through the proposed MM configurations. The incident THz field is polarized parallel to the split gap i.e, along the y axis. (b) Magnified view of the unit cell of the MM comprising of a toroidal SRR and two asymmetric C shaped resonators made up of aluminium. (c) Transmission spectra showing multiband transparency effect for d= 10 μm.

windows are observed. The first resonance dip D1 is at 0.88 THz, the second dip D2 is at 0.979 THz while the third dip is observed at 1.08 THz. The two transparency peaks termed as P1 and P2 are excited at 0.907 THz and 1.007 THz respectively. To understand the multiband EIT behaviour, transmission spectra and electric field profiles of each individual resonators and also that of the combined structure are studied in figure 5.3. Figure 5.3(a) describes the transmission obtained from the right CSRR. The transmission plot shows a resonance dip at 0.86 THz. The black trace in figure 5.3(b) depicts the transmission obtained from the mid TSRR. A resonance dip at 0.97 THz is observed. Further, the transmission plot for the left CSRR in figure 5.3(c) portrays a resonance dip at 1.05 THz. On combining all the three resonators, as observed from figure 3(d) and 3(e), three resonance dips (D1, D2, D3) and two resonance peaks (P1 and P2) are obtained. It may be suggested that the first dip D1 at 0.88 THz is due to the right CSRR, the second dip D2 at 0.979 THz is due to the mid TSRR and the third dip at D3 at 1.08 THz is due to the left CSRR, as can be understood from the behaviour of individual transmission plots of the three resonators. The strong near field coupling between the three resonators result in the transparency window observed in Figure 5.3(d) and 5.3(e) with transparency peaks at P1 corresponding to frequency 0.907 THz

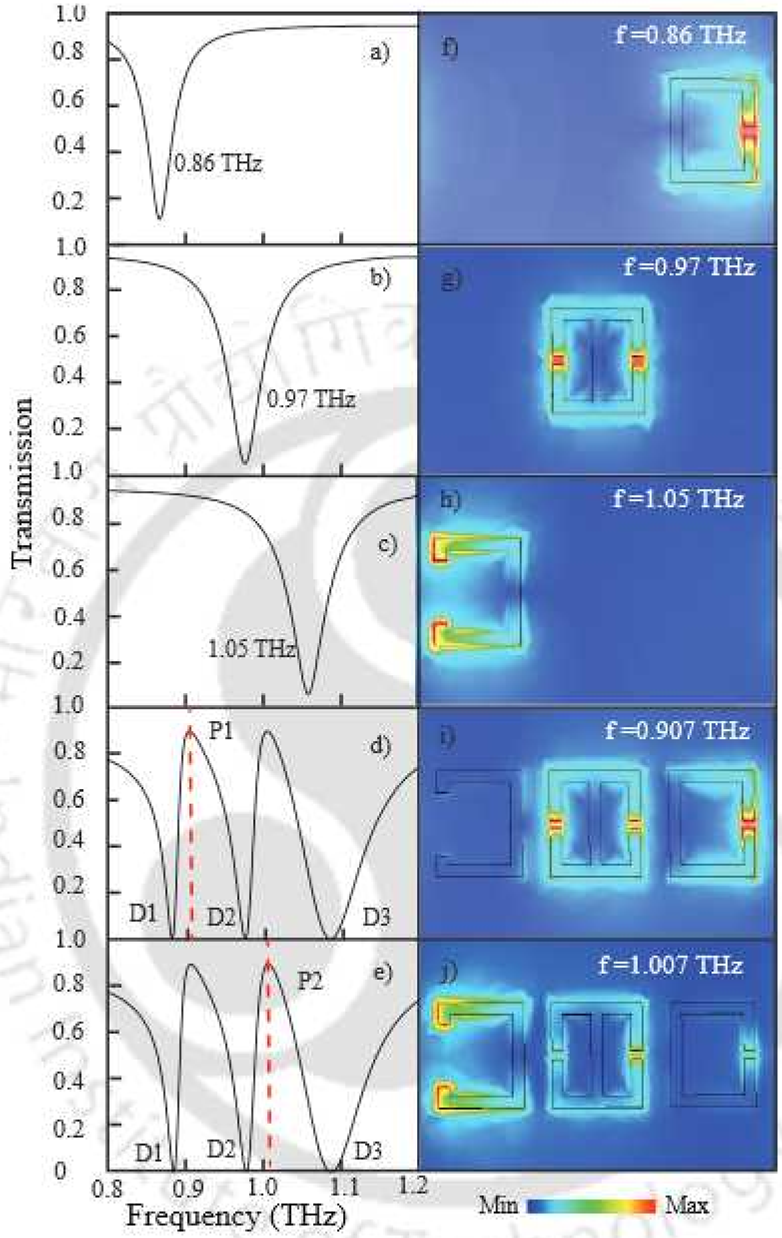

Figure 5.3: (a) The transmission for the right CSRR indictating individual resonance at 0.86 THz. (b) Transmission spectrum for mid TSRR demonstrating resonance at 0.97 THz. (c) Transmission spectrum corresponding to left CSRR showing resonance at 1.05 THz. (d) The transmission spectrum of combined MM at d = 10 μm. Multiband EIT is observed with peak frequencies indicated by red dotted lines at P1 and P2. (e) Peak P2 of the EIT window at 1.07 THz. (f) Electric field profile showing right CSRR excited at 0.86 THz. (g) Electric field profile showing TSRR excited at 0.97 THz. (h) Electric field profile showing left CSRR excited at 1.05 THz. (i) Eelectric field profile corresponding to peak P1 (0.907 THz) showing excitation of the TSRR and right SRR indicating coupling between the two. (j) Electric field profile corresponding to peak P2 (1.007 THz) showing excitation of left CSRR and TSRR.

and P2 corresponding to frequency 1.007 THz respectively.

5.3 Electric field analysis of the toroidal metasurface

To confirm multiband EIT due to coupling between the resonators, we discuss the electric field profile of the proposed MM. Figures 5.3 (f)-(h) provides a visual understanding of the electric field behaviour for the meta-atom. The electric field profile in figure 5.3(f) clearly demonstrates that the field is strongly confined at the split gap of the right most resonator at 0.86 THz. From figure 5.3(g) it is observed that the TSRR is excited at 0.97 THz. It is further seen in figure 5.3(h) that at 1.05 THz, electric field excitation is highest for the left resonator. This behaviour of electric field excitation is in line with the transmission resonance trend that was studied for each individual resonator. It can also be stated that each resonator behaves as a bright mode and is directly coupled to the incident terahertz radiation. Next the electric field excitations at the two peaks of the multiband transparency windows are studied. Figure 5.3(i) corresponds to the electric field excitation at peak P1 (0.907 THz) while figure 5.3(j) depicts the field excitation at P2 (1.007 THz). It is observed that at P1, the TSRR and right CSRR are excited strongly. Thus, it can be derived that there is a strong bright-bright mode near field coupling between the two resonators which leads to the introduction of 1st transparency window. Further, A similar observation is made at P2 where the TSRR and left CSRR are strongly excited, which signifies that the strong near field coupling between these two SRRs introduces the 2nd transparency window. The mode hybridization of the TSRR and the C shaped SRRs, and subsequent frequency detuning leads to the two transparency windows. Hence, it can be inferred that strong near field coupling between the bright -bright modes leads to the multiband EIT windows peaking at P1 and P2 respectively [93,94].

Next, the nature of the EM excitation was studied in each of the separate SRR by an individual evaluation of the surface current profiles. Figure 5.4 presents a magnified image of the resonators. Figure 5.4(a) exhibits surface current flowing along the anticlockwise direction leading to a dipolar excitation in the left 'C'resonator. Similar behaviour is observed in the right 'C'resonator , demonstrating dipolar excitation with current circulating in the clockwise direction. For the mid resonator shown in Fig 5.4 (b), it is observed that the surface current flow follows the toroidal excitation behaviour as discussed in chapter 1. Thus, the mid SRR exhibits toroidal dipolar excitation and is

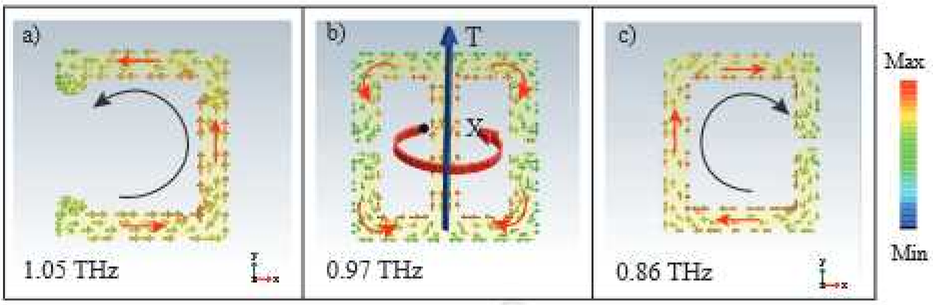

Figure 5.4: (a) Anticlockwise flow of surface current on the left CSRR (1.05 THz) exhibiting electric dipolar excitation. (b) Surface current profile in the mid TSRR (0.97 Thz) showing end to end formation of magnetic dipole moment leading to toroidal dipolar excitation T. (c) Clockwise flow of current in thr right CSRR (0.86 THz) exhibiting electric nature of exciation.

termed as 'TSRR'.

5.4 Toroidal excitations in the metasurface

To get a clear idea of the dominant nature of excitation in the combined proposed MM design, a multipolar analysis is performed for the five major electromagnetic moments i.e., electric dipole moment, magnetic dipole moment, toroidal dipole moment and electric and magnetic quadrupole moments. The power radiated by the individual moment i.e., 'WP','WT', 'WM', 'WQ_m', and 'WQ_e'respectively, for electric, toroidal, magnetic dipolar moment and magnetic and electric quadrupole moment is calculated as mentioned in the introductory chapter of the thesis. The black line in figure 5.5(a) represents the power radiated by toroidal dipolar moment, the blue line depicts the contribution to radiated power by magnetic dipolar moment. The scattered power contribution by the electric dipolar moment is shown by the red line. The green line shows power scattered by magnetic quadrupole moment while the purple line shows power scattered by electric quadrupole moment. The brown dotted lines indicate the position of peak 1 and peak 2 of the multiband windows. We observe significant contribution from toroidal scattered power and magnetic quadrupole scattered power near the peak frequencies of the EIT windows.The black curve at the peak frequencies of transparency windows, i.e., P1 and P2, and also at 0.97 THz, which is the resonance frequency of the TSRR, shows higher value of toroidal scattered power when compared to the other curves. It is evident from the figure that there is a dominant contribution to scattered power by the toroidal dipolar excitation in both the peak frequencies, P1 and P2 . The contribution by toroidal

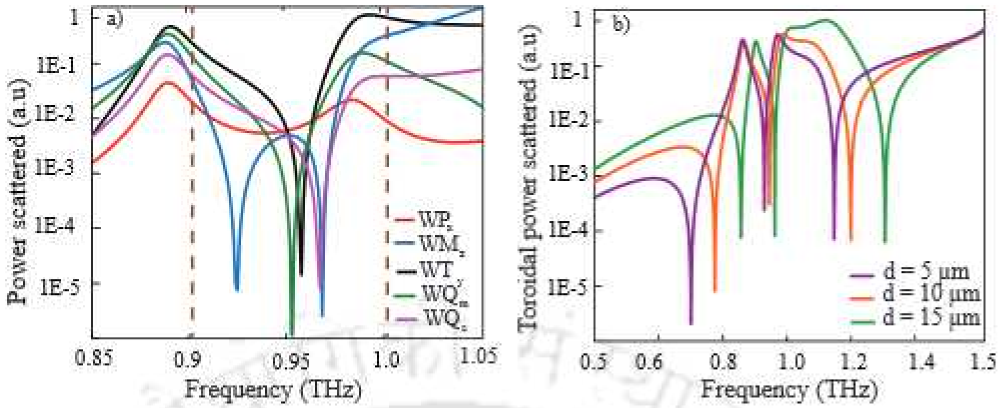

Figure 5.5: (a) Multipolar analysis for the MM configuration over the simulated frequency range indicating a dominance by toroidal dipolar excitation over electric and magnetic dipolar contributions, as well as electric and magnetic quadrupolar contributions. Dotted brown lines indicate positions of peak 1 and peak 2, respectively. (b) Blue shift in in the toroidal scattered power on increasing the distance '*d*'between the mid SRR and the C shaped resonators on both sides.

scattered power is also highest at 0.97 THz, i.e., the resonant frequency of the middle resonator. This confirms the toroidal nature of the mid resonator and also, the prominent dominance of toroidal excitation in the MM design in the EIT window. It signifies the excitation of electromagnetically induced transparency effect due to a toroidal terahertz MM configuration. We further examined the behaviour of the scattered power by toroidal dipolar moment on changing the distance '*d*'between the TSRR and CSRR symmetrically, as depicted in figure 5.5(b). The violet line indicates power scattered for '*d*'= 5 μm, the orange line for '*d*'= 10 μm and the green line signifies power scattered for '*d*'= 15 μm respectively. A blue shift in the scattered power is observed on the increase of d. We believe that the dips in the multipole expansion is due to the individual response of the resonators. The toroidal resonance is excited along the y-direction and the dip might indicate the power abosrbance by the toroidal meta-atom.

To get a better idea of sensing capacity the proposed MM, the Q factor of the '*d*'= 10 μm configuration for the first and second dips were calculated using the formula $Q = \frac{f_0}{FWHM}$, where f_0 is the resonant frequency and FWHM is the full width at half maximum of the resonance. It is found that for the first dip Q = 42, while for the second dip, Q = 34. Such high Q factor toroidal resonance could find utilisation in toroidal EIT based sensor applications.

5.5 Frequency modulation of transparency windows

The behaviour of the meta-surface on changing the distance between the TSRR and the other two CSRRs was examined. Distance '*d*'was changed symmetrically with respect to the TSRR by 5 μm , 10 μm and 15 μm respectively. Figure 5.6(a) shows the transmission plot for d = 5 μm, while figure 5.6(b) and figure 5.6(c) shows the transmission for d = 10 μm and d = 15 μm respectively. Here the solid curve illustrates the numerically simulated transmission spectra and the theoretically fitted transmission spectra are depicted by the dashed curves. The theoretical model is discussed in the next section. A blue shift in the peak frequencies P1 and P2 can be observed on increasing d. Thus, a frequency modulation of the multiband EIT window is achieved by a symmetric increase of the distance between the TSRRs and the CSRRs on each side. It is believed that the near field coupling between the TSRR and CSRRs decreases due to an increase in their separation resulting in a blue shift of the transparency windows in the proposed multiband transparency effect.

5.6 Theoretical modeling

To study the coupling mechanism between the toroidal resonator and two CSRRs and to validate the numerically obtained transmission spectra, we have used a theoretical model based on three coupled harmonic oscillator systems. Such a system can be represented by the following set of equations [93,94],

$$\begin{aligned} \ddot{x}_1 + \gamma_1 \dot{x}_1 + {\omega_1}^2 x_1 + {\Omega_1}^2 x_2 + {\Omega_2}^2 x_1 &= \frac{Q_1}{M_1} E, \\ \ddot{x}_2 + \gamma_2 \dot{x}_2 + {\omega_2}^2 x_2 + {\Omega_1}^2 x_1 &= \frac{Q_2}{M_2} E, \\ \ddot{x}_3 + \gamma_3 \dot{x}_3 + {\omega_3}^2 x_3 + {\Omega_2}^2 x_1 &= \frac{Q_3}{M_3} E, \end{aligned} \tag{5.1}$$

Here we represent the toroidal SRR as oscillator 1, the left CSRR as oscillator 2 and right CSRR as oscillator 3. Also (x_1, x_2, x_3), (γ_1,γ_2 ,γ_3), (ω_1 ,ω_2 ,ω_3) are the displacements, loss factors and resonance frequencies of oscillators 1, 2 and 3 respectively. Ω_1 and Ω_2 represent the coupling strengths between oscillators 1 and 2 and oscillators 1 and 3, respectively. However, we have neglected the coupling between oscillators 2 and 3. (Q_1, Q_2, Q_3), (M_1,M_2, M_3) are the effective charges and masses of the oscillators. The incident

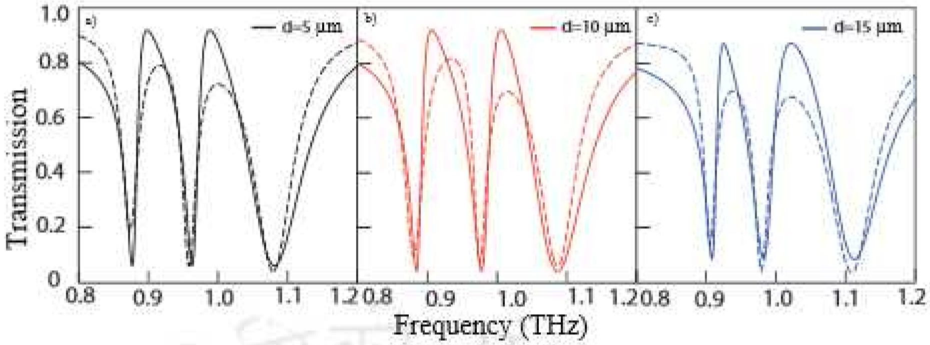

Figure 5.6: (a) Numerically simulated and theoretically fitted transmission spectra for d= 5 μm (a), 10 μm (b) and 15 μm (c). The dotted lines indicate the transmission profile obtained by theoretical modeling for the proposed multiband EIT effect.

electric field of the terahertz radiation is represented by $E = E_0 e^{i\omega t}$, where ω depicts frequency of the incident radiation.

To solve equation (4) and get displacements (x_1, x_2, x_3) we have assumed a trial solution as $x_n = N_n e^{i\omega t}$. By solving equation (4) for x_1, x_2, x_3 the susceptibility χ can be related with the polarization P of incident terahertz radiation as

$$\begin{aligned} \chi = \frac{P}{\epsilon_0 E} = \frac{Q_1 x_1 + Q_2 x_2 + Q_3 x_3}{\epsilon_0 E} \\ = \frac{Q_1^2}{M_1 \epsilon_0} (\frac{\alpha_1 \Omega_1^4 + \alpha_2 \Omega_2^4 + \alpha_3 \Omega_1^2 + \alpha_4 \Omega_2^2 + \eta + \beta \Omega_1^2 \Omega_2^2)}{D_1 D_2 D_3 - \Omega_2^4 D_2 - \Omega_1^4 D_1} \end{aligned} \tag{5.2}$$

where $D_1 = \omega_1^2 - \omega^2 + i\omega\gamma_1$, $D_2 = \omega_2^2 - \omega^2 + i\omega\gamma_2$, $D_3 = \omega_3^2 - \omega^2 + i\omega\gamma_3$ and $A_1 = \frac{Q_1}{Q_2}$, $A_2 = \frac{Q_1}{Q_3}$, $B_1 = \frac{M_1}{M_2}$ and $B_2 = \frac{M_1}{M_3}$.

Also we have taken here $\alpha_1 = -\frac{B_2}{A_2^2}$, $\alpha_2 = -\frac{B_1}{A_1^2}$, $\alpha_3 = -\frac{D_3}{A_1}(1 + B_1)$, $\alpha_4 = -\frac{D_2}{A_2}(1 + B_2)$,

$$\beta = \frac{B_1 + B_2}{A_1 A_2}, \eta = D_2 D_3 + \frac{B_1 D_2 D_3}{A_1^2} + \frac{B_2 D_1 D_2}{A_2^2}$$

Theoretically fitted transmission spectra has been obtained by using Krammer-Koning relations $T = 1 - imag(\chi)$, where we have used energy conservation principal A+T=1 (normalized to unity). Here absorption in the medium has been defined by $A = imag(\chi)$ .The dash curves in figure 5 illustrate theoretically fitted transmission spectra for d=5 μm,10 μm and 15 μm. It is evident from the figure that the analytically fitted transmission spectra are in good agreement with the corresponding numerically simulated ones. Here black traces illustrate multiband transparency spectra for d=5 μm, while that for d=10

μm and d=15 μm are depicted by red and blue traces respectively. It can be visualized from the figure that as the separation 'd'increases, both peaks of the two transparency windows get blue shifted. In the model we have taken resonance frequencies of the three resonators as ($\omega_1, \omega_2, \omega_2$=0.95 THz, 0.87 THz and 1.08 THz) and kept them constant to theoretically fit the transmission spectra with the simulated ones. The loss factors for three resonators are taken as 0.027, 0.023 and 0.05 THz respectively. Theoretically fitted transmission spectra for d=5 μm, matches well with the simulated ones for the coupling parameters Ω_1=0.25 THz and Ω_2 =0.20 THz. A change in the coupling parameters (Ω_1, Ω_2) leads to the blue shift of the transparency windows with change in 'd'. The coupling parameters are taken as (Ω_1 =0.22 THz, Ω_2 =0.18 THz) for d=10 μm and (Ω_1 =0.20 THz, Ω_2 =0.16 THz) for d=15 μm respectively. Hence, the blue shift of the transparency peaks with the change in separation 'd'is dictated by the reduction of coupling parameters Ω_1 and Ω_2.

5.7 Discussion

The single band and dual-band transparency effect via strong near field coupling between a toroidal resonator and two CSRRs has been discussed in this chapter in the THz range. The electric field profiles indicate coupling of bright-bright modes leading to multiband EIT with peaks at 0.907 THz and 1.007 THz. The dominance of toroidal dipolar excitation in the EIT windows was examined using a multipolar analysis of the scattered powers by the metasurface. Frequency modulation of the transparency windows by varying the distance 'd'between the adjacent resonators demonstrated a blue shift in the multiband transparency windows with increasing distance, which can be attributed to decreased coupling between the SRRs. For a thorough analytical understanding, the numerical results are fitted with a theoretical model based on three coupled oscillators. The theorectical modeling could impact future analysis of toroidal MM designs and studies. Such toroidal excitation based transparency effect in MMs would help the design of terahertz multiband devices including sensors, filters and modulators with lower radiation losses.

CHAPTER 6

POLARIZATION CONVERSION USING A TERAHERTZ TOROIDAL METASURFACE

In this chapter, we concentrate on the application of a toroidal metasurface in the broadband polarization conversion of terahertz radiation. The exploitation of the toroidal excitation can lead to a range of photonics-based applications. In this context, the broadband modulation of the polarization state of electromagnetic radiation can be significant. Traditional approaches for polarization conversion such as the use of birefringent crystals, the Faraday effect, total internal reflection effect have the drawback of limited conversion bandwidth and the efficiency owing to their specific wavelength dependence. In contrast, researchers have found that MMs show excellent performance in achieving broadband as well as highly efficient polarization conversion owing to their ultrathin thickness and scaling properties. Cheng et al. reported broadband reflective multilayer cross polarization converter which showed reasonably sustained bandwidth at a wide range of incident angles [95]. Xu et al. demonstrated broadband polarization conversion in transmission and reflection modes in multi-layered MM geometries [96]. Ako et al. demonstrated a three-layer transmissive polarization converter [97]. Broadband quarter wave-plates based on multilayer MM geometries have been reported in this frequency

---

Part of the results of this Chapter have been published in the following paper: Sarkar, R., Bhattacharya, A., Punjal, A., Prabhu, S. S. and Kumar, G. Broadband terahertz polarization conversion using a planar toroidal metamaterial. J. Appl. Phys. 132, 183103 (2022). Figures taken from the article are used in the chapter Reprinted from [120], with the permission of AIP Publishing.

regime [98]. Dynamic control of broadband polarization conversion has also been reported using graphene based metallic geometries [99,100,101].Linearly polarized light has been converted to its cross-component through the near field coupling existing between a pair of orthogonally twisted SRRs [102,103]. Apart from these studies, numerous other structures based on chiral and near-field coupled metamaterials have been reported for broadband polarization conversion[104-111]. Toroidal excitations with their inherent low-loss properties make a toroidal MM an ideal polarization convertor.

This chapter discusses and demonstrates broadband terahertz polarization conversion in a toroidal metamaterial. The increasing cross polarisation conversion of the incident radiation by gradual rotation of the MM from 0° to 45° in steps of 15° rotation angle is investigated. A multipolar analysis indicates toroidal excitation at 0° rotation of MM and significant scattered power of toroidal excitation on rotating the meta-atom. The chapter is organized: The second segment delves into metamaterial geometry and design. The third section provides numerically simulated results. A multipole analysis is performed to investigate the toroidal nature of the MM. The next section presents experimentally obtained results from fabricated MM structures and discusses them in detail folowed by a summary in the last section.

6.1 Design of the toroidal polarization converter

The MM was initially designed using commercially available CST microwave studio simulation software. The schematic of our proposed design is shown in figure 6.1(a). The unit cell of our proposed design consists of a double capacitive gapped split-ring resonator (SRR) made up of gold is displayed in figure 6.1(b). The resonators are patterned on a quartz substrate. The periodicity 'P' is taken as 44 μm , the length 'L' is 31 μm, and the width of each meta atom is $w = 5$ μm. The gap is $g = 5$ μm. The resonator is excited by the incident terahertz with its polarization parallell to the split gap of the meta-atom. Figure 1(c) illustrates the optical microgarph image of the fabricated sample.

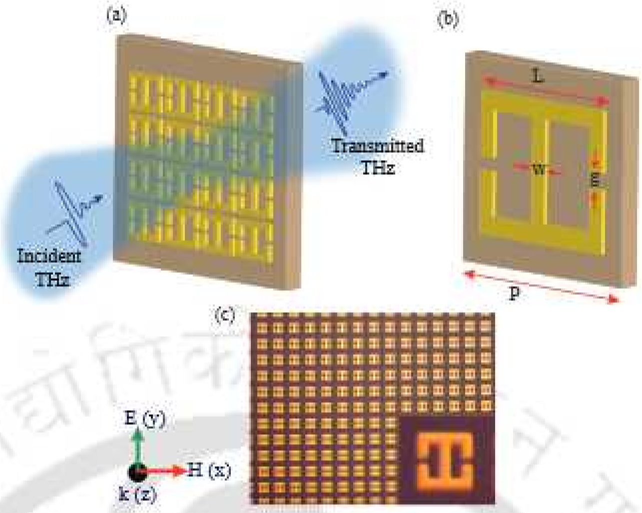

Figure 6.1: (a) The schematic comprising an array of a double capacitive gapped split-ring resonator (SRR), depicting terahertz transmission. (b) A closer look at the meta-molecule unit. The geometrical parameters are: P=44, L=31, g=w=5 μm. (c) The fabricated sample's optical microscopy image.

6.2 Terahertz cross-polarization conversion in the metasurface

The polarization conversion of the toroidal device was analyzed by initially studying the transmission profile of the MM. The y-and x-components of the transmission spectra are termed as co-and cross-polarization here. By rotating the suggested geometry with respect to the incident light at various angles, we were able to examine its co- and cross-polarization transmission spectra. θ denotes the rotation angle. Figures 6.2(a) and (b) exhibit simulated co- and cross-polarization spectra, respectively. The split gaps of the resonator are initially parallel to the polarization of incident terahertz. The SRR is further rotated by 15°, 30°, and 45° with respect to the incident THz radiation. The co-polarized transmission amplitude for θ=0° shows a sharp resonance dip at 1.21 THz. This is depicted by the black traces. In the figures 6.2(c) and 6.2(d), we have shown surface current profiles and magnetic field distributions at 1.21 THz to validate the resonance's toroidal behavior. Due to the surface current flowing counterclockwise at the left arm, it can be seen that the magnetic moment is moving in the plane's outward direction. On the other hand, the right arm's clockwise surface current flow is causing the magnetic moment to move into the plane. The end-to-end creation of magnetic moments leads to toroidal dipolar excitation along the y-axis. Figure 6.2 (e) provides an artistic

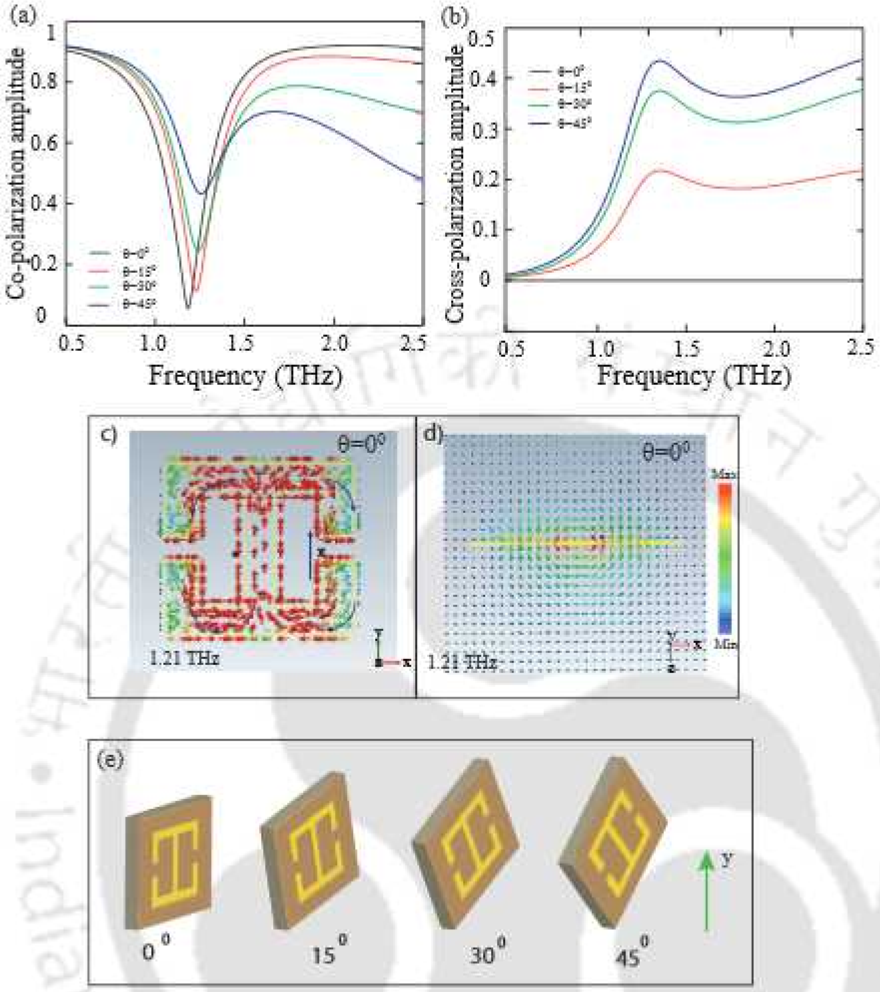

Figure 6.2: Numerically simulated (a) co- polarization spectra for 0° to 45° angles of rotation,(b) Cross-polarization transmission spectra for rotation angles 0° to 45°.(c) surface-current profiles and, (d) magnetic field profiles at the resonace frequency of 1.21 THz for θ=0°. (e) Artistic impression of the rotation of the metasurface by varying degrees.

impression for better understanding of the rotation of the metasurface carried out for a fixed co-polarization direction of the THz radiation along the Y axis. We displayed the magnetic field profile for the toroidal resonance at 1.21 THz, which demonstrated magnetic dipole moments aligned end to end. Further, the transmission spectrum for rotating the MM by θ=15° is shown by the red transmission curve. The green and blue curves depict the transmission spectrum obtained for rotation angle θ=30° and 45°. It has been found that the co-polarized transmission amplitude decreases from 0° to 45° degrees of rotation. For 45° rotation angle, the transmission spectrum shows a reduction in the amplitude by almost 50%. The corresponding transmission amplitude

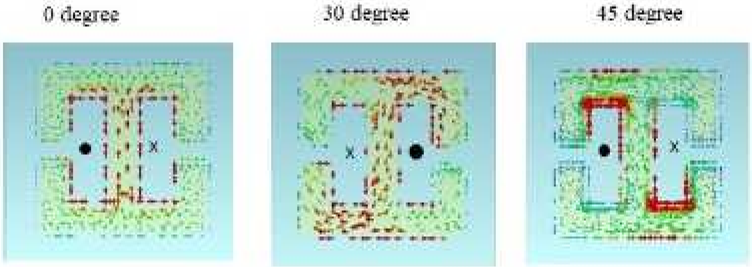

Figure 6.3: The toroidal excitation in the metasurface studied via the surface current profile in the metasurface at the resonant frequency. The surface current profile for (a) $\theta = 0°$ (b) $\theta = 30°$, and(c) $\theta = 45°$ rotation anles of the metasurface.

is also examined for the cross-polarized component of radiation. The cross-polarized transmission amplitude is zero for θ=0° as demonstrated by the black traces in figure 6.2 (d). The transmission amplitude gradually rises along with the rotation angle. 20% cross-polarization amplitude is seen for a wide range of 1.22 THz to 2.5 THz for θ=15°. The green traces show that cross-polarization conversion of 32.5% is seen for a frequency range of 1.19 THz to 2.5 THz for θ=30°. In the frequency range of 1.19 to 2.5 THz, our design exhibits a polarization conversion of 40%, reaching a high of 45% at 2.46 THz for θ=45°. The blue traces demonstrate this.

6.3 Analysis of toroidal behaviour of the metasurface

The toroidal excitation in the metasurface was studied using surface current profile and multipole analysis. Figure 6.3 provides a comparative analysis of the variation of surface current at the resonant frequency of each configuration. We observe that at the resonant frequencies, the surface current demonstrates clockwise flow in one arm and anti-clockwise flow on the other arm of the SRR. This indicates an end to end formation of magnetic moments. Hence, toroidal excitation is present in the different rotated configurations of the metamaterial. However, the variation in toroidal moment along the x and y directions is represented via the multipolar analysis. It may be observed that there is an increase in the x component of toroidal excitation on rotating the MM. Thus, the overall toroidal nature of the resonance persists even on the rotation of the MM by varying degrees as is evident from the surface current plots. To investigate the nature of the electromagnetic moments excited in the MM, we performed a multipolar analysis

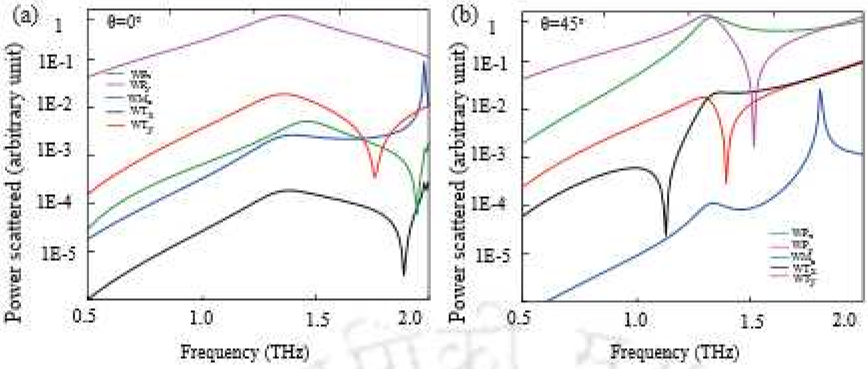

Figure 6.4: (a) Multipolar analysis for the electromagnetic moments when rotation angle is 0°. b) Multipolar analysis for the electromagnetic moments when rotation angle is 45°.

for the proposed geometry. The scattered power by the electric, magnetic, and toroidal dipolar resonance was calculated over the simulated frequency range. The multipole moments were evaluated using the surface current information. It was observed that for θ=0°, there is significant toroidal scattered power WTy, which contributes to the co-polarization transmission. This is shown in figure 6.4(a) by the red traces. In this case, the scattered power WTx shown by the black traces is quite low, which results in zero cross-polarization amplitude. It may be observed that on the rotation of the meta-atom still there is a significant contribution of the toroidal scattered power. Figure 6.4(b) shows the contribution of the scattered power by electromagnetic moments when the meta-atom is rotated by 45°. From the black traces, one can note that the toroidal scattered power WTx increases significantly and becomes almost equal to WTy. Because of the significant enhancement of WTx, our design shows maximum cross-polarization conversion in this case. The blue curve depicts the power scattered by magnetic dipolar contribution (WMz) while the green and magenta traces signifies electric dipolar components WPx and WPy respectively. It may be observed that there is significant toroidal scattered power over the broadband frequency range of 0.5 THz to 2 THz. From figure 6.4, it can be noted that although the power scattered by the toroidal dipole is smaller as compared to the electric dipole still it contributes to the polarization conversion. Further it can be noted that the z-component of magnetic dipole moment reduces due to the change in the excitation strength. The magnetic moment at the θ degree configuration is mostly attributed to the z component of magnetic moment while the x and y component may be ignored. On rotation of the MM, the x and y components of magnetic moments contribute partially to the power scattered, hence leading to a slight reduction in the scattered power of the

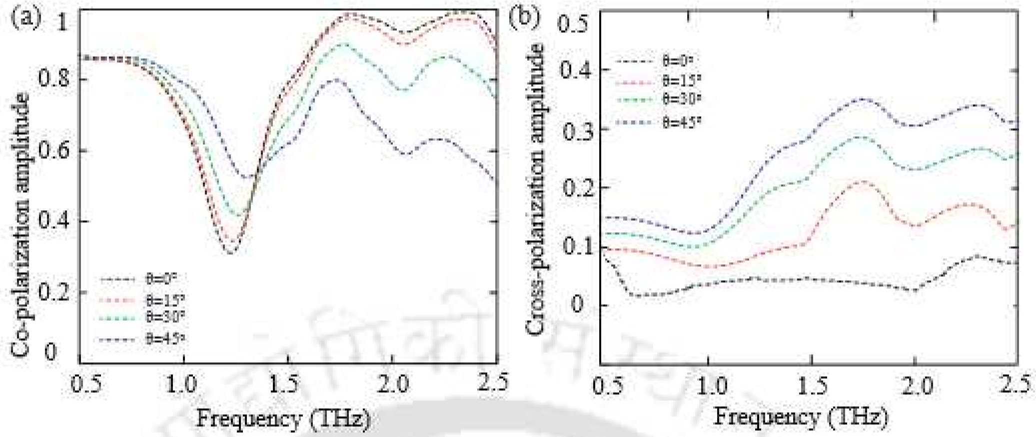

Figure 6.5: Experimentally measured (a) co-and (b) cross-polarization transmission spectra for rotation angles 0° to 45°.

z component of magnetic moment. It may be assumed that the scattered power by the x and y components of magnetic moment is negligible when compared to that of the toroidal and electric dipole moments. Based on this study, polarization conversion can also be achieved to infrared or optical frequencies by changing the length of the resonator. The cross-polarization conversion window can be shifted towards the higher frequency side by reducing the length of the resonator.

6.4 Fabrication of the metasurface and experimental results

We prepared the MM samples in a cleanroom environment using the standard lithography technique discussed in Chapter 2. We have taken a quartz wafer with a thickness of 500 μm and permittivity of $\epsilon_r = 4.42$. To evaluate the transmission spectra of the fabricated samples, we used a THz-TDS system as explained in detail in Chapter 2. We have further used a Polarizer and an analyzer in the path. Figures 6.5(a) and (b) show that the co- and cross-polarization amplitudes are maximum and almost zero for θ=0°, as indicated by the black dashed traces. Red, green, and blue traces represent the appropriate co- and cross-polarization spectra for θ=15°, 30° and 45° respectively. In a broad frequency range of 1.2 to 2.5 THz, we achieved cross-polarization conversions of 15%, 25%, and 35% for θ=15°, 30° and 45°, respectively, which are comparable with the numerical results. As the rotation angle is increased, the toroidal scattered power WTx increases, resulting in a progressive increase in cross-polarization conversion. Similarly, we can deduce that when toroidal dispersed power grows, WTy drops, resulting in a decrease in co-polarization transmission amplitude. Though the numerical and experimental results match consistently, there are mismatches in the results. The difference between the simulated and experimental results can be attributed to fabrication imperfections, resolution limitation of the THz-TDS setup as compared to the simulations, environmental factors etc.

6.5 Discussion

In this chapter the polarization conversion in a planar toroidal metamaterial, comprising a double capacitive gapped split-ring resonator (SRR), has been demonstrated both experimentally and numerically in the terahertz frequency range. The MM geometry's co- and cross-polarization transmission spectra are examined for rotation angles ranging from 0° to 45° in steps of 15° relative to the incident terahertz. The surface current distributions and magnetic field profiles at 1.21 THz confirm the toroidal excitation in our geometry. By rotating the geometry at an angle of 45°, we were able to exhibit cross-polarization conversion of about 40% throughout a wide frequency range of 1.19 to 2.5 THz, peaking at 44% at 2.46 THz. Further, we have performed the multipolar analysis of the scattered powers of electromagnetic radiation to understand the mechanism of cross-polarization conversion in our study. It is observed that the toroidal scattered power in the orthogonal direction increases with the rotation angle, signifying polarization conversion. Experimental results are found to be consistent with the numerical findings. Our findings could aid the development of broadband terahertz photonic devices.

CHAPTER 7

POLARIZATION INDEPEDENT LATTICE COUPLED TOROIDAL EXCITATION IN A TERAHERTZ METASURFACE

The previous chapters discussed the application of the toroidal resonances in polarization conversion and in exciting dual-band EIT in metasurfaces. Scientists have long sought to reduce radiative losses in the terahertz range. Besides the exotic toroidal resonance, another avenue for reduced radiation losses is the lattice mode of metasurfaces which depends on the periodicity of the MM. The lattice mode is a dark mode that arises due to diffraction along the interface of the periodically arranged meta-atoms of a metasurface. The energy transmitted is strongly confined to the surface, acting similar to a trap, hence reducing the far-field radiation [112]. The periodicity of the MM controls the resonant frequency of the lattice mode. Hence, the MM resonance can be easily coupled to the lattice mode by change in the periodicity without significant modification to the MM geometry. Coupling the MM resonance to the lattice mode has led to extremely high narrowing of resonance linewidths leading to very high-quality factor (Q) resonances and lowered radiative losses [113-117]. Though several studies have reported the tuning of electric dipole and Fano resonance via lattice mode coupling, and the excitation of lattice-induced transparency in metasurfaces, there has limited study of the coupling between toroidal resonance to the lattice mode [118]. Further, the polarization dependence of

---

*Part of the results of this chapter has been published in the article, Bhattacharya, Angana, B.C Chouhan, B. Bhowmik. and G. Kumar, "Polarization Independent Lattice-Coupled Toroidal Excitations in a Terahertz Metasurface". Journal of Physics D: Applied Physics, 2023, 56(41), 415101.

the incident radiation to the lattice mode coupling becomes a setback in the device's functionality. The coupling of the unique toroidal resonance to the lattice mode provides an interesting aspect in the dark-dark nature of their interaction.

In this chapter, we discuss numerically and experimentally, the polarization-independent coupling between a toroidal excitation to the first-order lattice mode (FOLM) in a planar terahertz metasurface leading to a sharp, high-quality factor resonance. The unique MM geometry results in the reduction of resonance linewidth, and an increase in the quality factor of the resonance for both the y-polarized and x-polarized modes of the incident terahertz radiation. Such MM-based devices that couple the dark lattice mode to the low-loss toroidal mode, independent of the periodicity, could be significant in the design of terahertz sensors and modulators. The polarization independence provides an extra degree of flexibility in device applications. The first section of the chapter elaborates the MM geometry followed by the numerical simulations and results

7.1 Design of the toroidal metasurface

Figure 7.1(a) shows a schematic of the proposed MM array with y-polarized THz radiation incident normally on the surface of the MM. The proposed MM was designed using CST microwave studio simulation software. Tetrahedral meshing was used and unit cell coundARY conditions were applied on the X and Y directions. The metamolecule has a simple symmetric geometry consisting of four aluminum split-ring resonators (SRR) of width 'w' = 6 μm, length 'l' = 30 μm, capacitive gap 'g'= 6 μm and the distance between adjacent resonators, 'd' = 6 μm as shown by the magnified SEM image in figure 7.1(c). The metamolecules are periodically arranged in a silicon substrate of permittivity $\epsilon = \sqrt{11.9}$ with initial periodicity 'p' = 97 μm.

7.2 Experimental fabrication of the metasurface

The fabrication of the metamaterial samples was done using photolithography. An SEM image of the fabricated MM array corresponding to P = 97 μm is shown in figure 7.1(b). Silicon substrate of 500 μm thickness was initially deposited with an aluminum layer of thickness 200 nm. It was then spin-coated with S1813 positive photoresist followed by UV exposure using a hard mask. After development, it was etched using an aluminium

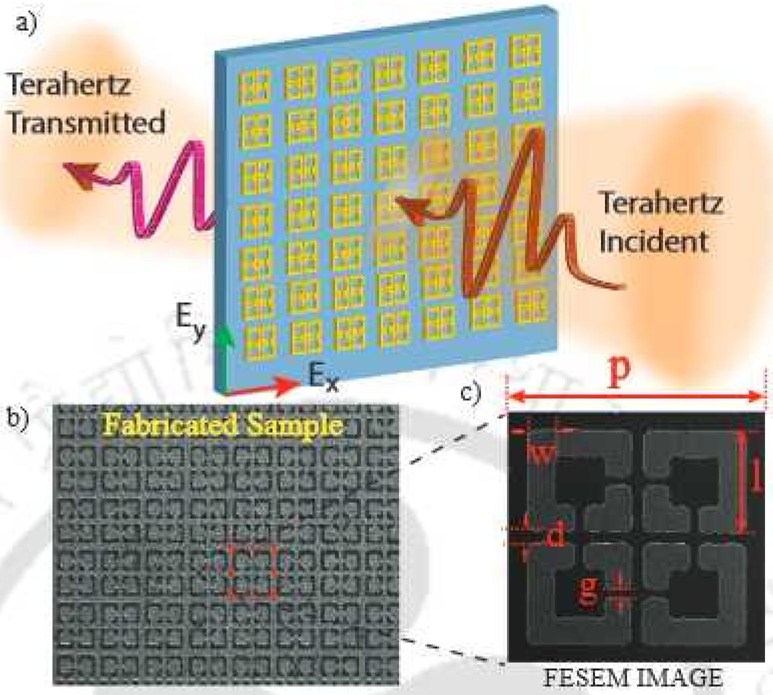

Figure 7.1: (a) Schematic of the proposed metamaterial array having y-polarized terahertz radiation incident normally on the surface. (b) SEM image of the fabricated metasurface array for P = 97 μm. (c) Magnified view of the fabricated meta-molecule with periodicity 'p', length of each split ring resonator 'l', width 'w', capacitive gap 'g', and the distance between adjacent resonators 'd'.

etchant to obtain the desired MM sample. Each MM sample consists of a 1-centimeter by 1-centimeter array of the designed metamolecule arranged periodically for varying 'p'. Samples were fabricated for 'p' = 120 μm, 97 μm, and 75 μm and the THz transmittance through the samples was measured experimentally. The terahertz transmittance measurements were done using a switch-based THz Time-domain spectroscopy setup.

7.3 Numerical analysis and experimental analysis of the metamaterial response

The MM simulations were performed for a wide range of 'p'. The simulations were performed using CST microwave studio simulation software using tetrahedral meshing in the frequency domain. The incident terahertz radiation was simulated such that the electric field was polarized along the y direction initially. The cross-polarized component is the one where the electric field is polarized along the x direction. The red line in figure

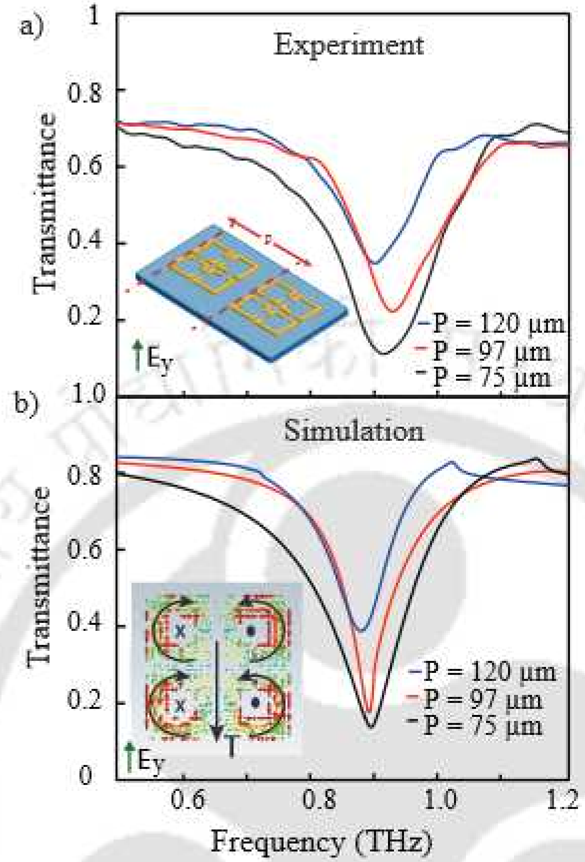

Figure 7.2: (a) Experimentally measured transmittance spectra for changing periodicities 'P' for y-polarized THz light. Inset depicts the periodicity 'P' of the metasurface which is being tuned. (b) Simulated transmittance spectra for varying periodicities of the MM for y-polarized incident light. Inset shows the surface current profile for P = 97 μm in the MM. The arrows indicate the direction of flow of the surface current.

7.2(a) shows the transmittance spectrum for P = 97μm of the MM. A sharp resonance is observed at 0.89 THz. The surface current profile at 0.89 THz for the metasurface with P = 97μm is evaluated as shown in the inset of figure 7.2(b). A clockwise current flow was observed in the left resonators while in contrast, an anti-clockwise current flow was observed in the right-hand resonators of the meta-molecule. This indicates a head-to-tail formation of magnetic moments leading to a toroidal dipole excitation along the negative Y axis.

7.3.1 Examination of lattice-coupled toroidal mode

Further, we study the lattice-coupled behavior of the toroidal excitation at 0.89 THz. The lattice mode F_L, at normal incidence, is given by the formula $F_L = \frac{c\sqrt{i^2+j^2}}{nP}$, where c is the speed of light, n is the refractive index of the substrate or the medium of propagation of the lattice mode, and P is the periodicity of the MM. (i, j) indicate non-negative integers that define the order of the lattice mode [114]. The FOLM has an (i, j) value of (0,1). Hence, the FOLM frequency is given by, $F_L = \frac{c}{nP}$. Thus, the coupling to the FOLM can be achieved by tuning the periodicity of the metasurface. It has been reported that the coupling of a MM resonance to the FOLM leads to sharp resonant features with high-quality factor. To verify this, we matched the f_{FOLM} to the toroidal resonant frequency of the MM, i.e., 0.89 THz, and evaluated the corresponding periodicity, P, which could excite the lattice mode at the selected frequency. Setting the values of f_{FOLM}=0.89 THz, c = $3x10^8$ m/s, and n = $\sqrt{\epsilon}$=$\sqrt{11.9}$, we obtained, P = 97 μm. Thus, the sharp toroidal mode was indeed verified to be the FOLM. To verify that the coupling between the toroidal mode and the FOLM leads to linewidth reduction in the MM, we measured the THz transmittance for varying periodicities P = 120 μm, and P = 75 μm of the metasurface. The results obtained from the experimental measurements are shown in figure 7.2 (a) while the numerically simulated results are shown in figure 7.2 (b). The sharp red curves in figures 2 (a,b) depicts the transmittance for P = 97 μm. The inset in figure 7.2 (a) indicates the periodicity of the MM array which is varied to study the transmittance behavior of the sample. The black lines in figures 2 (a,b) indicates the transmittance for P = 75 μm, and it was observed that the linewidth at 0.89 THz increased and a resonance broader than the one for P = 97 μm was excited. Further, the transmittance for P = 120 μm was evaluated as shown by the blue lines in figures 7.2 (a,b). A broad resonance was observed at 0.89 THz for P = 120 μm with around 50% transmittance amplitude. We observed that the measured transmittance spectrum for P = 120 μm, 97 μm, and 75 μm matched closely with the simulation results. A slight shift in the resonance frequency was observed which may be attributed to human errors in the fabrication process. Further, the measured transmittance spectrum does not reflect the sharpness of the lattice coupled mode at P = 97 μm, which was believed to be a result of the limitations in the resolution of the experimental THZ-TDS setup. From these observations, it was verified that modulation of the transmittance amplitude and resonance sharpness by tuning of periodicity, and the reduced line-width of the resonance at P= 97 μm, was a

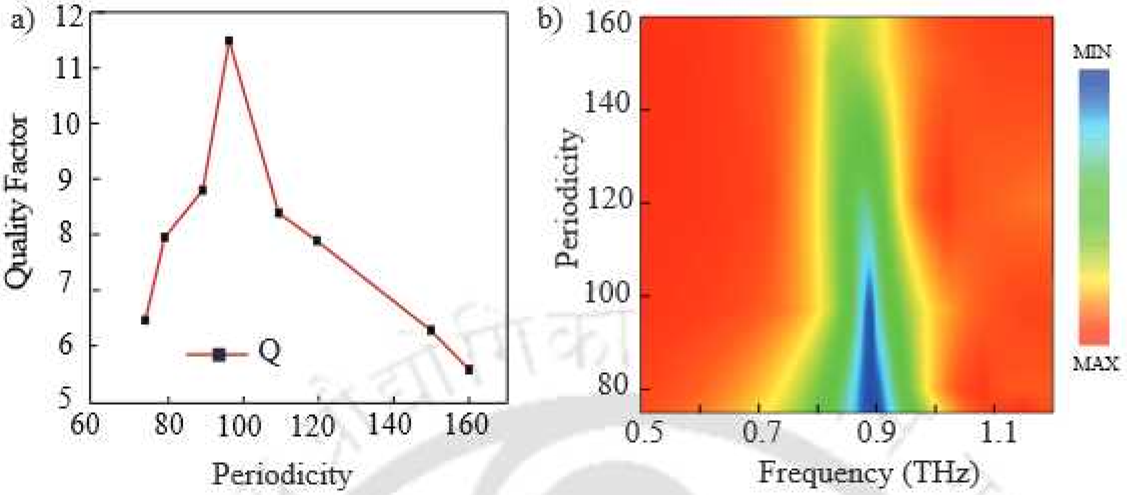

Figure 7.3: (a) Quality factor variation of the toroidal resonance at 0.89 THz for different values of periodicity 'P' of the MM. (b) Modulation of the transmittance line-width for varying P of the MM.

result of the coupling of the toroidal mode with the FOLM. Hence, coupling of the FOLM to the toroidal mode resulted in a sharp "toroidal-coupled lattice mode" with increased transmission depth.

7.3.2 Quality factor analysis of the metasurface

The decrease in linewidth of the toroidal excitation is further quantified by evaluating the quality factor (Q) of the resonance. The quality factor (Q) of a resonant circuit is a dimensionless parameter defined as the ratio of the energy stored in the mode to the energy dissipated per cycle of oscillation. A high Q indicates a low loss. We used the Fano line shape fitting formula to evaluate the Q. The formula is given by, $T = (a + ib + \frac{c}{\omega - \omega_0 + i\gamma})^2$, where T is the transmittance, and a, b, c are constants. 'ω' is the frequency range while ω_0 is the resonance frequency. 'γ' indicates the damping rate in the circuit. The Q value is calculated by, $Q = \frac{\omega_0}{2\gamma}$. In this study, we Fano-fitted the transmittance for different values of periodicity of the metasurface and reported the resultant Q of the toroidal mode. Figure 7.3(a) depicts the variation of Q with changing periodicities. The Q for P = 97 μm, i.e, the lattice-coupled toroidal mode was evaluated to be equal to 11. 47. Further, the Q for P = 75 μm was evaluated to 6.48, while that for P = 120 μm evaluated to 7.9. It may be observed that there is a sharp rise in the Q for the lattice-coupled toroidal mode at P = 97 μm. As the periodicity is increased beyond

120 μm, the Q values fall off and become about 5.8 for P = 160 μm and higher. Hence, as predicted, the coupling of the toroidal mode to the FOLM resulted in a high Q, sharp resonance mode. A 51% increase in Q is observed for the lattice-coupled toroidal mode for P = 97 μm as compared to the Q at higher periodicity of 160 μm. Moreover, a 44% increase in Q is reported as compared to the lower periodicity, P = 75 μm. The contour plot in figure 7.3(b) depicts line-width of the resonance for varying P in the frequency range of 0.5 THz to 1.2 THz.

7.3.3 Polarization independent behaviour of the metasurface

In order to provide an extra degree of freedom in applications of the toroidal-coupled lattice mode for terahertz meta-devices, we explored the polarization-independent characteristics of the proposed MM. Initially, the transmittance was reported for y polarized incident THz radiation falling normally on the MM sample. Next, measurements were performed to study the toroidal mode such that the electric field was polarized along the x direction. Simulations are performed to verify the experimental results. The experimental measurements are shown in figure 7.4(a) while figure 7.4(b) shows the simulated results for transmittance of the MM with the electric field polarized along the x-axis. The blue line in figure 7.4(a) depicts the measured x-polarized transmittance for P = 120 μm, the red line depicts that for P = 75 μm, while the black curve depicts the same for P = 97 μm. The dotted lines indicate the corresponding transmittance for the y-polarized THz radiation that was measured and simulated previously. It may be observed from figure 7.4(a) that the x-polarized transmittance matches exactly with the simulated results for the y-polarized transmittance. The lattice-coupled mode is observed at 0.89 THz for P = 97 μm. It can be observed from figure 7.4(b) that the simulated results closely match the measured results for the x-polarized mode. The blue curve, red curve, and black curve in figure 7.4(b) depict the simulated transmittance for P = 120 μm, P = 97 μm, and P = 75 μm respectively. Thus, it is experimentally and numerically verified that the toroidal-coupled lattice mode is invariant with the polarization of the incident THz radiation. Further, the nature of the resonance at 0.89 THz for the x-polarized incident THz radiation was analyzed by performing a multipole anlaysis of the scattered powers of radiation by the electric, magnetic, and toroidal dipole moment, as described in chapter 1. The multipole analysis is shown in figure 7.5. The black line depicts the power scattered by the toroidal dipole moment (PT), the green line shows the electric

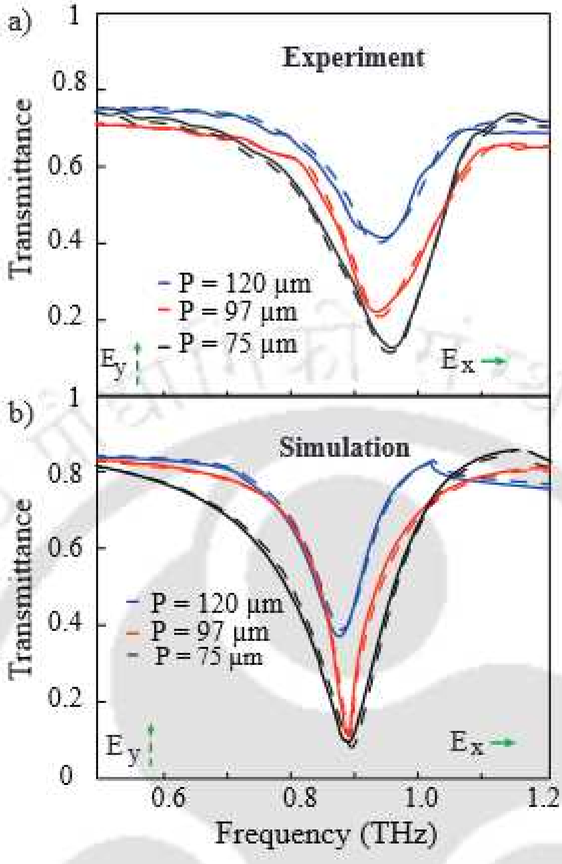

Figure 7.4: (a) Experimentally measured transmittance for varying periodicity when the electric field of incident THz radiation is polarized along the x-axis. The dotted lines indicate the measured transmittance for the y-polarized THz radiation. (b) Simulated transmittance for varying periodicity of MM for x-polarization of incident THz radiation. The dotted lines show simulated transmittance for the y-polarized THz beam.

dipole scattered power (PE), while the red line shows the scattered power by magnetic dipole moment (PM). The analysis is done for the lattice coupled mode at P = 97 μm. It is observed that the toroidal mode has the highest scattered power indicating that the resonance at 0.89 THz for the x-polarized beam is also a lattice-coupled toroidal mode.

7.4 Discussion

Through this chapter, the polarization-independent coupling of the exotic toroidal resonance to a first-order lattice mode was demonstrated. Measurements for varying periodicities, for y-polarized THz radiation, demonstrated that the lattice coupled mode for periodicity P = 97 μm at 0.89 THz shows decreased line-width of the resonance. Surface

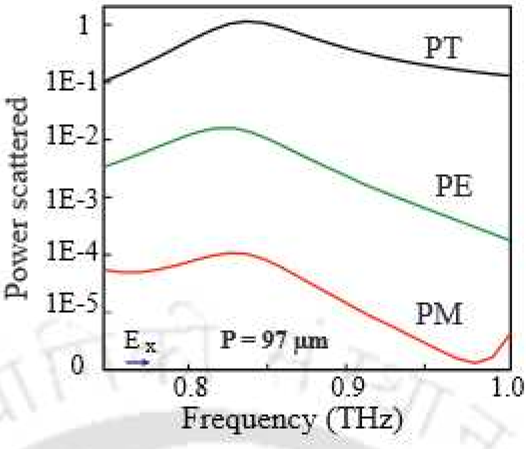

Figure 7.5: Multipole analysis of the power scattered by toroidal, electric, and magnetic dipole moments for x-polarized incident Hz radiation corresponding to P=97 μm of the MM configuration.

current profile indicated that the MM geometry has an inherent toroidal dipole excitation at 0.89 THz. The quality factor (Q) calculation of the lattice-coupled toroidal mode shows a 51% increase in Q for the metasurface configuration corresponding to P = 97 μm as compared to higher periodicities. Further, the transmittance for the x-polarized THz radiation is measured, and it is reported that the metasurface demonstrates polarization independent lattice coupled toroidal mode. Multipole analysis of the scattered power of electromagnetic radiation confirmed toroidal domination for the lattice-coupled mode for x-polarized light. Thus, a terahertz meta-device that excites a polarization independent sharp toroidal-coupled lattice mode was experiemntally realized. Such an increase in Q of a dark toroidal mode via coupling to the lattice mode can find wide applications in polarization independent highly sensitive sensors, modulators, and photonic devices for terahertz applications. .

CHAPTER 8

SUMMARY AND FUTURE SCOPE

In this thesis, we have discussed the toroidal dipole moment and its excitation in terahertz metasurfaces. This includes the near-field coupling between toroidal moments and their interaction in bilayer MMs, the active modulation of toroidal excitations , and the near field coupling in toroidal metasurfaces leading to dual band EIT. The applications of toroidal moments have been explored experimentally in designing a toroidal THz polarization convertor, and a polarization-independent toroidal metadevice that demonstrates enhanced Q factor due to coupling between the lattice-coupled toroidal mode.

In chapter 1, we provided a comprehensive literature review on toroidal excitations in 3D and planar terahertz metasurfaces and their applications.

In chapter 2, we discussed the design, fabrication, and characterization of THz toroidal metasurfaces. The THz-TDS is explained briefly to describe the THz generation and detection process.

In chapter 3, a bilayer MM configuration comprising of two layers of SRRs seperated by a polyimide layer is presented that demonstrates dual toroidal dipolar excitation. The interaction between the two layers of toroidal resonators is examined. A multipolar analysis is performed to study the power scattered by toroidal, electric and magnetic dipole vector over the simulated frequency range. The modulation and switching from dual toroidal resonances to a single toroidal excitation is reported via the rotation of the top resonator. The Q factor of the resonances is evaluated to explore the coupling behaviour. A theoretical model is presented that uses the Lagrangian approach to explain the coupling between the resonators.

In chapter 4, the actively tunable response of toroidal excitation is examined ina graphene based metasurface. By tuning the Fermi energy of the graphene layer, an active modulation of the MM response is observed. It was reported that an increasing Fermi energy from 0.2 eV to 1 eV led to prominent toroidal excitations. The magnetic field and surface current profiles explained the toroidal resonances. Further, a change in relaxation time of graphene layer was used to explore the active amplitude modulation of the toroidal response.

In chapter 5, the single band excitation of EIT was explored by coupling between a toroidal and a C shaped resonator. Further, by adding another LC resonator, dual band EIT was excited in the toroidal metasurface. Multipole analysis demonstrated toroidal domination in the EIT windows. The bright-bright mode coupling lead to the excitation of multiband EIT windows with peaks at 0.907 THz and 1.007 THz. For a thorough analytical understanding, the numerical results were fitted with a theoretical model based on three coupled oscillators.

In chapter 6, a numerical and experimental demonstration of an ultra-broadband polarization conversion in a planar toroidal metamaterial is demonstrated. The co- and cross-polarization transmission spectra for the metasurface is examined for rotation angles ranging from 0° to 45° in steps of 15° relative to the incident terahertz. The rotating of the geometry at an angle of 45° led to cross-polarization conversion of about 40% in a broad frequency range of 1.19 to 2.5 THz, peaking at 44% at 2.46 THz. Mulitpole analysis explains the role of the toroidal components in polarization conversion.

In chapter 7, the polarization-independent coupling of the exotic toroidal resonance to a first-order lattice mode was explored. Measurements for varying periodicities, for y-polarized THz radiation, demonstrated that the lattice coupled mode for periodicity P = 97 μm at 0.89 THz shows decreased line-width of the resonance. Surface current profile and multipole analysis indicated that the MM geometry has an inherent toroidal dipole excitation at 0.89 THz. The quality factor (Q) calculation of the lattice-coupled toroidal mode shows an increase in Q for the metasurface configuration corresponding to P = 97 μm as compared to higher periodicities. Further, the transmittance for the x-polarized THz radiation is measured, and it is reported that the metasurface demonstrates polarization-independent lattice coupled toroidal mode. Thus, a terahertz meta-device that excites a polarization-independent sharp toroidal-coupled lattice mode.

Future Scope of work

The toroidal resonance, in recent times, has emerged as a promising topic of research. The work done in this thesis opens up newer grounds for studies on toroidal THz metasurfaces. In this thesis, the active tuning of toroidal resonance has been studied by simulating MMs made up of graphene. Due to limitations in fabrication facilities, the study could be limited to numerical simulations. The experimental realization of active tuning of toroidal excitation could be carried out in the future.

In this study, the passive switching from dual to single toroidal excitation was reported in a bilayer metasurface. This can be further explored experiemntally to demonstrate multilayer configurations, and toroidal components could be included in integrated photonic circuits.

In this thesis, the excitation of a single band and dual band EIT was explored by the near field coupling between a toroidal resonator and two C type resonators. There is a lot of scope in the experimental realization of such toroidal dual band EIT in THz metasurfaces. MMs could be fabricated using photolithography to experimentally demonstrate dual-band EIT in terahertz metasurfaces. Polarization independent EIT in toroidal metasurfaces also could be explored in the THz regime. Further, the dual-band EIT can be extended to explore triple and multi-band EIT effects in metasurfaces.

To explore the possibility of manipulating the toroidal resonance, the lattice-coupled mode can be widely explored. The polarization independent toroidal-coupled lattice mode, which was indepedent for orthogonal polarizations, can be extended to polarization independence for varying degrees of rotation. Such flexibilites in design of toroidal metasurfaces could be significant in the development of low-loss terahertz photonic devices for applications in next generation communication.

BIBLIOGRAPHY

1 C. Sirtori, "Bridge for the terahertz gap," Nature, vol. 417, no. 6885, pp. 132–133, 2002.

2 X.-C. Zhang and J. Xu, Introduction to THz wave photonics, vol. 29. Springer, 2010.

3 C. Fattinger and D. Grischkowsky, "Terahertz beams," Appl. Phys. Lett., vol. 54, no. 6, pp. 490–492, 1989..

4 N. M. Burford and M. O. El-Shenawee, "Review of terahertz photoconductive antenna technology," Opt. Eng., vol. 56, no. 1, p. 10901, 2017.

5 D. R. Smith, J. B. Pendry, and M. C. K. Wiltshire, "Metamaterials and negative refractive index," Science (80-.)., vol. 305, no. 5685, pp. 788–792, 2004.

6 J. B. Pendry, A. J. Holden, D. J. Robbins, and W. J. Stewart, "Magnetism from conductors and enhanced nonlinear phenomena," IEEE Trans. Microw. Theory Tech., vol. 47, no. 11, pp. 2075–2084, 1999.

7 W. Cai and V. M. Shalaev, Optical metamaterials, vol. 10, no. 6011. Springer, 2010.

8 N. I. Zheludev and Y. S. Kivshar, "From metamaterials to metadevices," Nat. Mater., vol. 11, no. 11, pp. 917–924, 2012.

9 V. M. Shalaev, "Optical negative-index metamaterials," Nat. Photonics, vol. 1, no. 1, pp. 41–48, 2007.

10 H. Chen, C. T. Chan, and P. Sheng, "Transformation optics and metamaterials," Nat. Mater., vol. 9, no. 5, pp. 387–396, 2010.

11 W. J. Padilla and R. D. Averitt, "Imaging with metamaterials," Nat. Rev. Phys., vol. 4, no. 2, pp. 85–100, 2022.

12 M. Y. Azab, M. F. O. Hameed, A. M. Nasr, and S. S. A. Obayya, "Highly sensitive metamaterial biosensor for cancer early detection," IEEE Sens. J., vol. 21, no. 6, pp. 7748–7755, 2021.

13 S. Lin et al., "Using antibody modified terahertz metamaterial biosensor to detect concentration of carcinoembryonic antigen," IEEE J. Sel. Top. Quantum Electron., vol. 27, no. 4, pp. 1–7, 2020.

14 S. Banerjee, B. P. Pal, and D. Roy Chowdhury, "Resonance phenomena in electromagnetic metamaterials for the terahertz domain: a review," J. Electromagn. Waves Appl., vol. 34, no. 10, pp. 1314–1337, 2020.

15 S. Rao, Y. K. Srivastava, G. Kumar, and D. Roy Chowdhury, "Modulating fundamental resonance in capacitive coupled asymmetric terahertz metamaterials," Sci. Rep., vol. 8, no. 1, pp. 1–8, 2018.

16 K. M. Dhriti, M. Islam, A. Bhattacharya, A. Ahmad, and G. Kumar, "Plasmon-induced transparency in an air–dielectric grooved parallel-plate terahertz waveguide," JOSA B, vol. 38, no. 4, pp. 1290–1296, 2021.

17 C. Xu, Z. Ren, J. Wei, and C. Lee, "Reconfigurable terahertz metamaterials: from fundamental principles to advanced 6G applications," Iscience, p. 103799, 2022.

18 A. Kumar, M. Gupta, P. Pitchappa, N. Wang, M. Fujita, and R. Singh, "Terahertz topological photonic integrated circuits for 6G and beyond: A Perspective," J. Appl. Phys., vol. 132, no. 14, p. 140901, 2022.

19 Y. J. Tan, W. Wang, A. Kumar, and R. Singh, "Interfacial topological photonics: broadband silicon waveguides for THz 6G communication and beyond," Opt. Express, vol. 30, no. 18, pp. 33035–33047, 2022.

20 Y. Yang et al., "Terahertz topological photonics for on-chip communication," Nat. Photonics, vol. 14, no. 7, pp. 446–451, 2020.

21 D. Yan et al., "A Review: The Functional Materials-Assisted Terahertz Metamaterial Absorbers and Polarization Converters," in Photonics, 2022, vol. 9, no. 5, p. 335.

22 N. K. Grady et al., “Terahertz metamaterials for linear polarization conversion and anomalous refraction,” Science (80-.)., vol. 340, no. 6138, pp. 1304–1307, 2013.

23 S. Luo, B. Li, A. Yu, J. Gao, X. Wang, and D. Zuo, “Broadband tunable terahertz polarization converter based on graphene metamaterial,” Opt. Commun., vol. 413, pp. 184–189, 2018.

24 T. C. Tan, Y. K. Srivastava, M. Manjappa, E. Plum, and R. Singh, “Lattice induced strong coupling and line narrowing of split resonances in metamaterials,” Appl. Phys. Lett., vol. 112, no. 20, p. 201111, 2018.

25 R. Singh, I. A. I. Al-Naib, M. Koch, and W. Zhang, “Sharp Fano resonances in THz metamaterials,” Opt. Express, vol. 19, no. 7, pp. 6312–6319, 2011.

26 M. Manjappa, Y. K. Srivastava, L. Cong, I. Al-Naib, and R. Singh, “Active photoswitching of sharp Fano resonances in THz metadevices,” Adv. Mater., vol. 29, no. 3, p. 1603355, 2017.

27 S. Han, P. Pitchappa, W. Wang, Y. K. Srivastava, M. V Rybin, and R. Singh, “Extended Bound States in the Continuum with Symmetry-Broken Terahertz Dielectric Metasurfaces,” Adv. Opt. Mater., vol. 9, no. 7, p. 2002001, 2021.

28 S. Han et al., “All-Dielectric Active Terahertz Photonics Driven by Bound States in the Continuum,” Adv. Mater., vol. 31, no. 37, p. 1901921, 2019.

29 X. Zhao et al., “Terahertz investigation of bound states in the continuum of metallic metasurfaces,” Optica, vol. 7, no. 11, pp. 1548–1554, 2020.

30 “Toroidal dipolar response in a metamaterial,” Science (80-.)., vol. 330, no. 6010, pp. 1510–1512, 2010, doi: 10.1126/science.1197172.

31 I. B. Zel’Dovich, “Electromagnetic interaction with parity violation,” Sov. Phys. JETP, vol. 6, no. 6, pp. 1184–1186, 1958.

32 V. M. Dubovik and A. A. Cheshkov, “Multipole distribution in classical and quantum field theory and radiation,” Fiz. Elem. Chastiz i At. Jadra, vol. 5, no. 3, pp. 791–837, 1974.

33 N. Talebi, S. Guo, and P. A. Van Aken, "Theory and applications of toroidal moments in electrodynamics: Their emergence, characteristics, and technological relevance," Nanophotonics, vol. 7, no. 1, pp. 93–110, 2018, doi: 10.1515/nanoph-2017-0017.

34 C. Ederer and N. A. Spaldin, "Towards a microscopic theory of toroidal moments in bulk periodic crystals," Phys. Rev. B, vol. 76, no. 21, p. 214404, 2007.

35 V. Savinov, V. A. Fedotov, and N. I. Zheludev, "Toroidal dipolar excitation and macroscopic electromagnetic properties of metamaterials," Phys. Rev. B, vol. 89, no. 20, p. 205112, 2014.

36 N. Papasimakis, V. A. Fedotov, V. Savinov, T. A. Raybould, and N. I. Zheludev, "Electromagnetic toroidal excitations in matter and free space," Nat. Mater., vol. 15, no. 3, pp. 263–271, 2016.

37 A. Ceulemans, L. F. Chibotaru, and P. W. Fowler, "Molecular anapole moments," Phys. Rev. Lett., vol. 80, no. 9, p. 1861, 1998.

38 L. Joshua-Tor, H. E. Xu, S. A. Johnston, and D. C. Rees, "Crystal structure of a conserved protease that binds DNA: the bleomycin hydrolase, Gal6," Science (80-.)., vol. 269, no. 5226, pp. 945–950, 1995.

39 A. S. Zimmermann, D. Meier, and M. Fiebig, "Ferroic nature of magnetic toroidal order," Nat. Commun., vol. 5, no. 1, pp. 1–6, 2014.

40 A. K. Yadav et al., "Observation of polar vortices in oxide superlattices," Nature, vol. 530, no. 7589, pp. 198–201, 2016.

41 X. Zhao et al., "Terahertz investigation of bound states in the continuum of metallic metasurfaces," Optica, vol. 7, no. 11, pp. 1548–1554, 2020.

42 Z. Liu et al., "High-Quality-Factor Mid-Infrared toroidal excitation in folded 3D metamaterials," Adv. Mater., vol. 29, no. 17, p. 1606298, 2017.

43 J. Li, Z.-G. Dong, M.-J. Zhu, J. Shao, Y.-H. Wang, and J.-Q. Li, "Dual-band toroidal-dipole-induced transparency in optical regime," J. Phys. D. Appl. Phys., vol. 49, no. 34, p. 345104, 2016.

44 Y. Fan et al., "Achieving a high-Q response in metamaterials by manipulating the toroidal excitations," Phys. Rev. A, vol. 97, no. 3, p. 33816, 2018.

45 Z.-G. Dong et al., “Optical toroidal dipolar response by an asymmetric double-bar metamaterial,” Appl. Phys. Lett., vol. 101, no. 14, p. 144105, 2012.

46 A. A. Basharin, V. Chuguevsky, N. Volsky, M. Kafesaki, and E. N. Economou, “Extremely high Q-factor metamaterials due to anapole excitation,” Phys. Rev. B, vol. 95, no. 3, p. 35104, 2017.

46 A. A. Basharin, V. Chuguevsky, N. Volsky, M. Kafesaki, and E. N. Economou, “Extremely high Q-factor metamaterials due to anapole excitation,” Phys. Rev. B, vol. 95, no. 3, p. 35104, 2017.

47 V. R. Tuz, V. V Khardikov, and Y. S. Kivshar, “All-dielectric resonant metasurfaces with a strong toroidal response,” ACS Photonics, vol. 5, no. 5, pp. 1871–1876, 2018.

48 G. Zhang, C. Lan, R. Gao, Y. Wen, and J. Zhou, “Toroidal dipole resonances in all-dielectric oligomer metasurfaces,” Adv. Theory Simulations, vol. 2, no. 10, p. 1900123, 2019.

49 A. Ahmadivand et al., “Rapid detection of infectious envelope proteins by magnetoplasmonic toroidal metasensors,” ACS sensors, vol. 2, no. 9, pp. 1359–1368, 2017.

50 M. Gupta et al., “Sharp toroidal resonances in planar terahertz metasurfaces,” Adv. Mater., vol. 28, no. 37, pp. 8206–8211, 2016.

51 M. Gupta, Y. K. Srivastava, M. Manjappa, and R. Singh, “Sensing with toroidal metamaterial,” Appl. Phys. Lett., vol. 110, no. 12, p. 121108, 2017.

52 M. Gupta, Y. K. Srivastava, and R. Singh, “A toroidal metamaterial switch,” Adv. Mater., vol. 30, no. 4, p. 1704845, 2018.

53 S. Wang, S. Wang, X. Zhao, J. Zhu, Q. Li, and T. Chen, “Excitation of electromagnetically induced transparency effect in asymmetrical planar terahertz toroidal dipole metasurfaces,” J. Infrared, Millimeter, Terahertz Waves, vol. 42, pp. 40–49, 2021.

54 A. Bhattacharya, K. M. Devi, T. Nguyen, and G. Kumar, “Actively tunable toroidal excitations in graphene based terahertz metamaterials,” Opt. Commun., vol. 459, p. 124919, 2020.

55 S. Wang, S. Wang, Q. Li, X. Zhao, and J. Zhu, “Dual toroidal dipole resonance metamaterials under a Terahertz domain,” Materials (Basel)., vol. 11, no. 10, p. 2036, 2018.

56 J. P. Marangos, “Electromagnetically induced transparency,” J. Mod. Opt., vol. 45, no. 3, pp. 471–503, 1998.

57 Fan Y, Wei Z, Hongqiang Li, Chen H and Soukoulis C M 2013, Low-loss and high-q planar metamaterial with toroidal moment Phys. Rev. B 87 115417

58 Fan Y, Zhang F, Shen N-H, Quanhong F, Wei Z, Hongqiang Li and Soukoulis C M 2018, "Achieving a high-q response in metamaterials by manipulating the toroidal excitations", Phys. Rev. A 97 033816

59 Wang S, Zhao X, Wang S, Quan Li, Zhu J and Han L 2020, "The investigation of the electromagnetic coupling effect in terahertz toroidal metasurfaces and metamaterials", J. Mater. Res. Technol. 9 3935–42

60 Tang C, Yan B, Wang Q, Chen J, Yan, Z, Liu F, Chen N and Sui C 2017, "Toroidal dipolar excitation in metamaterials consisting of metal nanodisks and a dielectric spacer on metal substrate", Sci. Rep. 7 1–8

61 Li T, Ye R X, Li C, Liu H, Wang S M, Cao J X, Zhu S N and Zhang X 2009, "Structural-configurated magnetic plasmon bands in connected ring chains", Opt. Express 17 11486–94

62 Sun B and Yingying Y 2019, "Double toroidal spoof localized surface plasmon resonance excited by two types of coupling mechanisms", Opt. Lett. 44 1444–7

63 Gerislioglu, B., A. Ahmadivand, and N. Pala, Tunable plasmonic toroidal terahertz metamodulator. Physical Review B, 2018. 97(16): p. 161405.

64 Ahmadivand, A., et al., Gated Graphene Enabled Tunable Charge–Current Configurations in Hybrid Plasmonic Metamaterials. ACS Applied Electronic Materials, 2019.

65 Gupta, M., Y.K. Srivastava, and R. Singh, A toroidal metamaterial switch. Advanced materials, 2018. 30(4): p. 1704845.

66 Mun, S.E., et al., Enhancement and switching of fano resonance in metamaterial. Advanced Optical Materials, 2018. 6(17): p. 1800545

67 Lee, S.H., et al., Switching terahertz waves with gate-controlled active graphene metamaterials. Nature materials, 2012. 11(11): p. 936

68 Li, Q., et al., Active graphene–silicon hybrid diode for terahertz waves. Nature communications, 2015. 6: p. 7082

69 Mousavi, S.H., et al., Inductive tuning of Fano-resonant metasurfaces using plasmonic response of graphene in the mid-infrared. Nano letters, 2013. 13(3): p. 1111-1117

70 Liu, G.-D., et al., Toroidal resonance based optical modulator employing hybrid graphene-dielectric metasurface. Optics express, 2017. 25(21): p. 26045-26054

71 Devi, K.M., et al., Plasmon induced transparency effect through alternately coupled resonators in terahertz metamaterial. Optics express, 2017. 25(9): p. 10484-10493

72 Huang, Z., et al., Broadband terahertz modulator based on graphene metamaterials. AIP Advances, 2018. 8(3): p. 035304

73 Dong, Z.-G., et al., Optical toroidal dipolar response by an asymmetric double-bar metamaterial. Applied Physics Letters, 2012. 101(14): p. 144105

74 Chen, X. and W. Fan, Study of the interaction between graphene and planar terahertz metamaterial with toroidal dipolar resonance. Optics letters, 2017. 42(10): p. 2034-2037

75 Ju, L., et al., Graphene plasmonics for tunable terahertz metamaterials. Nature nanotechnology, 2011. 6(10): p. 630.

76 Xiao, S., et al., Active modulation of electromagnetically induced transparency analogue in terahertz hybrid metal-graphene metamaterials. Carbon, 2018. 126: p. 271-278.

77 Fang, Z., et al., Active tunable absorption enhancement with graphene nanodisk arrays. Nano letters, 2013. 14(1): p. 299-304.

78 Carrasco, E., M. Tamagnone, and J. Perruisseau-Carrier, Tunable graphene reflective cells for THz reflectarrays and generalized law of reflection. Applied Physics Letters, 2013. 102(10): p. 104103.

79 Griffiths, D.J., Introduction to electrodynamics, 2005, AAPT

80 Wu, C., et al., Spectrally selective chiral silicon metasurfaces based on infrared Fano resonances. Nature communications, 2014. 5: p. 3892

81 Lim, W.X. and R. Singh, Universal behaviour of high-Q Fano resonances in metamaterials: terahertz to near-infrared regime. Nano convergence, 2018. 5(1): p. 5

82 He, X., et al., Graphene patterns supported terahertz tunable plasmon induced transparency. Optics express, 2018. 26(8): p. 9931-9944.

83 Marangos, J. P. Electromagnetically induced transparency. J. Mod. Opt. 45, 471–503 (1998).

84 Safavi-Naeini, A. H. et al. Electromagnetically induced transparency and slow light with optomechanics. Nature 472, 69 (2011).

85 Papasimakis, N. et al. Metamaterial with polarization and direction insensitive resonant transmission response mimicking electromagnetically induced transparency. Appl. Phys. Lett. 94, 211902 (2009).

86 Xu, J. et al. Terahertz microfluidic sensing with dual-torus toroidal metasurfaces. Adv. Opt. Mater. 9, 2100024 (2021).

87 35. Li, H. et al. Low-loss metamaterial electromagnetically induced transparency based on electric toroidal dipolar response. Appl.Phys. Lett. 106, 083511 (2015).

88 Shen, Z.-Y. et al. Electromagnetically induced transparency in novel dual-band metamaterial excited by toroidal dipolar response. Front. Phys. 15, 1–7 (2020).

89 JunáHe, X. et al. A low-loss electromagnetically induced transparency (EIT) metamaterial based on coupling between electric and toroidal dipoles. RSC Adv. 7, 55897–55904 (2017).

90 Shen, Z. et al. Electromagnetically induced transparency metamaterial with strong toroidal dipole response. Mater. Res. Express 7, 035802 (2020).

91 Sun, G., Peng, S., Zhang, X. and Zhu, Y. Switchable electromagnetically induced transparency with toroidal mode in a grapheneloaded all-dielectric metasurface. Nanomaterials 10, 1064 (2020).

92 Wang, S. et al. Excitation of electromagnetically induced transparency effect in asymmetrical planar terahertz toroidal dipole metasurfaces. J. Infrared Millim. Terahertz Waves 42, 40–49 (2021).

93 Yu, W. et al. The bright–bright and bright–dark mode coupling-based planar metamaterial for plasmonic EIT-like effect. Opt. Commun. 414, 29–33 (2018).

94 Zhang, H., Cao, Y., Liu, Y., Li, Y. and Zhang, Y. A novel graphene metamaterial design for tunable terahertz plasmon induced transparency by two bright mode coupling. Opt. Commun. 391, 9–15 (2017).

95 Z. Cheng, W. Withayachumnankul, A. Upadhyay, D. Headland, Y. Nie, R. Z. Gong, M. Bhaskaran, S. Sriram, and D. Abbott, "Ultrabroadband reflective polarization convertor for terahertz waves," Appl. Phys. Lett. 105(18), 181111 (2014).

96 K.-K. Xu, Z.-Y. Xiao, and J.-Y. Tang, "Linearly polarized converters for reflected and transmitted waves based on double-split ring resonator," Plasmonics 12(6), 1869–1874 (2017).

97 R. T. Ako, W. S. L. Lee, S. Atakaramians, M. Bhaskaran, S. Sriram, and W. Withayachumnankul, "Ultra-wideband tri-layer transmissive linear polarization converter for terahertz waves," APL Photonics 5(4), 046101 (2020).

98 W. Pan, X.-Y. Ren, Q. Chen, and X.-Y. Wang, "A broadband terahertz quarter wave plate based on asymmetric cross slots," Optoelectron. Lett. 15(5), 352–355 (2019).

99 Zhang, Y. Feng, T. Jiang, J. Cao, J. Zhao, and B. Zhu, "Tunable broadband polarization rotator in terahertz frequency based on graphene metamaterial," Carbon 133, 170–175 (2018).

100 Yu, X. Gao, W. Qiao, L. Wen, and W. Yang, "Broadband tunable polarization converter realized by graphene-based metamaterial," IEEE Photonics Technol. Lett. 28(21), 2399–2402 (2016).

101 Quader, J. Zhang, M. R. Akram, and W. Zhu, "Graphene-based highefficiency broadband tunable linear-to-circular polarization converter for terahertz waves," IEEE J. Sel. Top. Quantum Electron. 26(5), 1–8 (2020).

102 Li, C.-C. Chang, Q. Zhou, C. Zhang, and H.-T. Chen, "Resonance coupling and polarization conversion in terahertz metasurfaces with twisted split-ring resonator pairs," Opt. Express 25(21), 25842–25852 (2017).

103 J. Mohan Rao, R. Sarkar, G. Kumar, and D. R. Chowdhury, "Gradual cross polarization conversion of transmitted waves in near field coupled planar terahertz metamaterials," OSA Continuum 2(3), 603–614 (2019).

104 Dincer, C. Sabah, M. Karaaslan, E. Unal, M. Bakir, and U. Erdiven, "Asymmetric transmission of linearly polarized waves and dynamically wave rotation using chiral metamaterial," Prog. Electromagn. Res. 140, 227–239 (2013).

105 Cong, N. Xu, W. Zhang, and R. Singh, "Polarization control in terahertz metasurfaces with the lowest order rotational symmetry," Adv. Opt. Mater. 3(9), 1176–1183 (2015).

106 J. Liu, Z.-Y. Xiao, X.-L. Ma, K.-K. Xu, J.-Y. Tang, and Z.-H. Wang, "Broadband asymmetric transmission and polarization conversion of a linearly polarized wave based on chiral metamaterial in terahertz region," Wave Motion 66, 1–9 (2016).

107 Wei, Y. Cao, Y. Fan, X. Yu, and H. Li, "Broadband polarization transformation via enhanced asymmetric transmission through arrays of twisted complementary split-ring resonators," Appl. Phys. Lett. 99(22), 221907 (2011).

108 H. Fan, Y. Zhou, X.-P. Ren, R.-W. Peng, S.-C. Jiang, D.-H. Xu, X. Xiong, X.-R. Huang, and M. Wang, "Freely tunable broadband polarization rotator for terahertz waves," Adv. Mater. 27(7), 1201–1206 (2015).

109 Cong, Y. K. Srivastava, and R. Singh, "Near-field inductive coupling induced polarization control in metasurfaces," Adv. Opt. Mater. 4(6), 848–852 (2016).

110 Cong, Y. K. Srivastava, and R. Singh, "Inter and intra-metamolecular interaction enabled broadband high-efficiency polarization control in metasurfaces," Appl. Phys. Lett. 108(1), 011110 (2016).

111 Singh, E. Plum, W. Zhang, and N. I. Zheludev, "Highly tunable optical activity in planar achiral terahertz metamaterials," Opt. Express 18(13), 13425–13430 (2010).

112 M. Manjappa, Y. K. Srivastava, and R. Singh, "Lattice-induced transparency in planar metamaterials," Physical Review B 94, 161103 (2016).

113 N. Xu, R. Singh, and W. Zhang, "High-q lattice mode matched structural resonances in terahertz metasurfaces," Applied Physics Letters 109, 021108 (2016).

114 T. C. Tan, Y. K. Srivastava, M. Manjappa, E. Plum, and R. Singh, "Lattice induced strong coupling and line narrowing of split resonances in metamaterials," Applied Physics Letters 112, 201111 (2018).

115 A. Bitzer, J. Wallauer, H. Helm, H. Merbold, T. Feurer, and M. Walther, "Lattice modes mediate radiative coupling in metamaterial arrays," Optics express 17, 22108–22113 (2009).

116 S. Karmakar, D. Kumar, R. K. Varshney, and D. R. Chowdhury, "Latticeinduced plasmon hybridization in metamaterials," Optics Letters 45, 3386–3389 (2020).

117 Al-Naib, R. Singh, C. Rockstuhl, F. Lederer, S. Delprat, D. Rocheleau, M. Chaker, T. Ozaki, and R. Morandotti, "Excitation of a high-q subradiant resonance mode in mirrored single-gap asymmetric split ring resonator terahertz metamaterials," Applied Physics Letters 101, 071108 (2012).

118 Lou, R. Yang, J. Liang, Y. Yu, L. Zhang, C. Zhang, T. Li, Y. Fan, F. Zhang, G. Wang, et al., "Dual-sensitivity terahertz metasensor based on lattice–toroidal-coupled resonance," Advanced Photonics Research 2, 2000175 (2021).

119 Dong, J. et al. Terahertz frequency-wavelet domain deconvolution for stratigraphic and subsurface investigation of art painting. Opt. Express 24, 26972–26985 (2016).

117 Bhattacharya, A., Sarkar, R. and Kumar, G. Excitation of near field coupled dual toroidal resonances in a bilayer terahertz metamaterial configuration. J. Phys. D. Appl. Phys. (2021).

118 Bhattacharya, A., Sarkar, R. and Kumar, G. Toroidal electromagnetically induced transparency based meta-surfaces and its applications. iScience 25, (2022).

119 Bhattacharya, A., Sarkar, R., Sharma, N.K. et al. Multiband transparency effect induced by toroidal excitation in a strongly coupled planar terahertz metamaterial. Sci Rep 11, 19186 (2021).

120 Rakesh Sarkar, Angana Bhattacharya, Ajinkya Punjal, Shriganesh S. Prabhu, and Gagan Kumar , "Broadband terahertz polarization conversion using a planar toroidal metamaterial", Journal of Applied Physics 132, 183103 (2022).

122 Gupta, Manoj, and Ranjan Singh. "Toroidal metasurfaces in a 2D flatland." Reviews in Physics 5 (2020): 100040.

123 Ahmadivand, Arash, et al. "Toroidal metaphotonics and metadevices." Laser and Photonics Reviews 14.11 (2020): 1900326.

124 Kupriianov, Anton S., et al. "Metasurface engineering through bound states in the continuum." Physical Review Applied 12.1 (2019): 014024.